# NOVEL COORDINATES FOR NONLINEAR MULTIBODY MOTION WITH APPLICATIONS TO SPACECRAFT DYNAMICS AND CONTROL

A Dissertation

by

HANSPETER SCHAUB

Submitted to the Office of Graduate Studies of
Texas A&M University
in partial fulfillment of the requirements for the degree of

DOCTOR OF PHILOSOPHY

May 1998

Major Subject: Aerospace Engineering

# NOVEL COORDINATES FOR NONLINEAR MULTIBODY MOTION WITH APPLICATIONS TO SPACECRAFT DYNAMICS AND CONTROL

A Dissertation

by

HANSPETER SCHAUB

Submitted to Texas A&M University
in partial fulfillment of the requirements
for the degree of

DOCTOR OF PHILOSOPHY

Approved as to style and content by:

| | |
|---|---|
| J. L. Junkins<br>(Chair of Committee) | |
| S. R. Vadali<br>(Member) | K. T. Alfriend<br>(Member) |
| A. Datta<br>(Member) | K. T. Alfriend<br>(Head of Department) |

May 1998

Major Subject: Aerospace Engineering

## ABSTRACT

Novel Coordinates for Nonlinear Multibody Motion with Applications
to Spacecraft Dynamics and Control. (May 1998)
Hanspeter Schaub, B.S., Texas A&M University;
M.S., Texas A&M University
Chair of Advisory Committee: Dr. John L. Junkins

Novel sets of attitude coordinates called the Stereographic Parameters (SPs) and configuration quasivelocity coordinates called the Eigenfactor Quasivelocities (EQVs) are discussed. The SPs are generated through stereographic projections of the Euler parameter constraint hypersphere onto hyperplanes. SP sets are non-unique and have distinct alternate sets referred to as shadow sets. They abide by the same differential kinematic equation, but generally display a different singular behavior. Explicit expressions are developed that map the original SP set to the shadow set and thus avoid any singularities. Both symmetric SPs such as the classical and Modified Rodrigues Parameters (MRPs), as well as asymmetric SPs are discussed. A globally asymptotically stable MRP feedback law which tracks any reference trajectory is presented. Both unsaturated and saturated control cases are discussed. Further, an MRP costate switching condition is developed that allows both original and shadow MRPs to be used simultaneously in optimal control problems.

The Lagrange equations of motion in terms of the $n$-dimensional EQV vector are developed. The EQV formulation has an identity mass matrix which results in no matrix inverse being taken in numerical simulations. An explicit expression is presented that incorporates Pfaffian non-holonomic constraints into the EQV formulation without increasing the system order. Unfortunately, the use of EQV in

numerical simulations only proved beneficial in selected cases. Generally the computational burden proved too high. However, the EQVs are found to be valuable when used as velocity feedback coordinates. EQV feedback laws have an exponentially decaying kinetic energy, superior performance to traditional state velocity feedback laws and are found to decouple the motion of multi-link robotic systems.

The equations of motion and steering laws of spacecraft containing Variable Speed Control Moment Gyroscopes (VSCMGs) are developed. Contrary to classical CMG steering laws, the VSCMG steering laws derived herein are do not encounter singularities. Both gimbal angle velocity and acceleration based steering laws are presented. Since gimbaling is more efficient energy consumption wise, the steering law presented only utilizes reaction wheel modes close to classical CMG singularities. The reaction wheel mode also assists in driving the gimbals to preferred angles using null motion.

To my parents, Sis and Hanspeter,

for their love and support

and to Steve and Caesar

for always being there

## ACKNOWLEDGMENTS

Special thanks to Dr. John L. Junkins, whose guidance and support during my graduate studies has been beyond exceptional. I would also like to thank my other advisors Dr. S. R. Vadali, Dr. K. T. Alfriend and Dr. A. Datta for their guidance. Further, I must thank Dr. Rush Robinett of Sandia National Labs for supporting me and allowing me to work on so many interesting projects.

Last, but not least, I would like to thank Andrea Loggins and Lisa Willingham for all their help in getting the paper work done to attend the many conferences, publish the various journal papers and complete my degrees.

# TABLE OF CONTENTS

CHAPTER Page

# LIST OF FIGURES

FIGURE Page

# LIST OF TABLES

# CHAPTER I

# INTRODUCTION

This dissertation explores the role of coordinate selection in analytical dynamics in a broad sense and in multibody spacecraft dynamics and controls in particular. The early portion of the dissertation deals with the classical case of a single rigid body. Subsequent developments are introduced that apply to a large family of multibody dynamics problems. Finally, a detailed study is addressed to systems of variable speed control moment gyroscopes. In these developments, novel coordinate choices, together with Lyapunov stability theory, are utilized to establish new insights into dynamics, stability, and control of nonlinear multibody systems.

The choice of configuration coordinates used to describe nonlinear dynamical systems is a very fundamental and important issue. Unfortunately, it is also very often an overlooked one.[1] Choosing an inappropriate set of configuration coordinates can unduly complicate the resulting dynamical expressions and the time evolution of the motion as seen in the chosen coordinates. Further, singularities can be introduced that are solely due to the choice of coordinates and *not* inherent in the actual dynamical system. For example, the standard aircraft orientation angles, the 3-2-1 Euler angles yaw, pitch and roll, are singular when the aircraft pitches up or down 90 degrees.[2] This is a geometric singularity and has nothing to do with the actual aircraft motion. Therefore, choosing these Euler angles as the orientation parameters artificially limits the type of maneuvers that can thus be performed or controlled. Similar examples can be found for spacecraft dynamics and robotics. Tsiotras and Longuski introduce a new set of rigid body attitude coordinates called the $(w, z)$ coordinates in Ref. 3. The

---

The journal model is *AIAA Journal of Guidance, Control and Dynamics.*

parameter $w$ is a complex parameter and $z$ is a real scalar quantity. These attitude coordinates lend themselves perfectly to describe the orientation of a spinning rigid body since $w$ describes the spin axis orientation and $z$ essentially defines the current rotation angle about the spin axis. Therefore these attitude coordinates provide excellent feedback parameters to stabilize a spinning symmetric spacecraft about its spin axis as shown in Ref. 4.

Several new coordinate choices are discussed in this dissertation that have useful properties for describing dynamical systems and/or have benefits when used as feedback variables in a control law. Chapter II introduces a family of attitude coordinates called the Stereographic Parameters (SPs). They are a minimal set of attitude coordinates which are closely related to the Euler parameters (quaternions). The Euler parameters are a well-known set of four attitude coordinates which have been extensively used both in academia and industry. They have several elegant properties, but their popularity arises from the fact that they do not contain any singular orientations and have a linear kinematic differential equation. They achieve these remarkable properties by increasing the number of coordinates from three to four. This redundancy can cause some numerical difficulties at times.[5]

This dissertation will focus on sets of minimal attitude coordinates that are functionally equivalent to the Euler parameters. Sets of minimal attitude coordinates all have one thing in common, they go singular at particular orientation. Different sets differ by the location of their singular orientation and the nonlinearity of their differential kinematic equations. The family of stereographic parameters are attractive since they allow custom sets of attitude parameters to be created whose singularities are set at specific orientations. Two general classes of SPs are introduced. The symmetric SPs are singular at specific principal rotation angles regardless about which axis the rigid body is rotated. The asymmetric SPs only become singular at specific

principal rotations angles about certain axes. The most elegant set of SP attitude coordinates are called the Modified Rodrigues Parameters (MRPs). Their basic formulation was first introduced as a modification to the classical Rodrigues parameters[6] by Wiener in Ref. 7(1962). Thereafter they did not appear in the literature for over two decades and remained largely undeveloped. The MRPs were essentially "rediscovered" by Marandi and Modi in Ref. 8 and studied further by Tsiotras in Refs. 9 and 10. They have many attractive properties such as being able to describe *any arbitrary* orientation, having kinematic differential equations with only second order polynomial nonlinearities and being able to scale to higher dimensions.

While chapter II deals with sets of configuration variables, chapter III studies novel velocity coordinates called the Eigenfactor Quasivelocity coordinates (EQVs). Complex dynamical systems, such as found in multi-body dynamics, typically have large, configuration variable dependent system matrices. Numerically simulating these systems often involves inverting a configuration-variable dependent mass matrix to find the corresponding instantaneous state acceleration vectors. Jain and Rodriguez discuss a method called the diagonalized Lagrangian robot dynamics in Ref. 11. Their formulation introduces a new set of quasivelocity coordinates which render the system mass matrix equal to the identity matrix. This dissertation presents another set of quasivelocities which diagonalize the Lagrangian dynamics. Whereas Jain and Rodriguez use the innovations factorization to parameterize the mass matrix, an instantaneous spectral decomposition will be used in this dissertation. This method replaces the task of inverting the configuration dependent mass matrix with the one of solving the corresponding eigenfactor differential equations. The literature usually deals with the case where the mass matrix $M$ and and its derivative $\dot{M}$ are given and one needs to solve for the eigenfactor derivatives.[12–15] A simple method is presented that establishes kinematic-like differential equations for the eigenfactors

which can be integrated. The method includes provisions for the case of crossing eigenvalues. The resulting Lagrangian dynamics in terms of these quasivelocities provide for a natural splitting of the *dynamics* and *kinematics* of the equations of motion. The development is analogous to the introduction of the orthogonal components of the body angular velocity vector as the quasivelocity vector for a rigid body. Euler's equations of motion of a rigid body are typically not written in terms of the second derivative of the attitude vector, but in terms of the derivative of the orthogonal components of the body angular velocity vector.

The EQV formulation also allows for Pfaffian constraints to be directly incorporated into the equations of motion without increasing the overall dimension of the system. Numerical studies are performed to examine any benefits and drawbacks of this formulation when used to solve numerical simulations. Further, just as the body angular velocity vector plays an important role in rigid body velocity feedback laws, the use of the EQV as feedback coordinates is examined. Simple globally asymptotically stable EQV feedback laws are developed and compared to classical velocity feedback laws.

In chapter IV the marriage between two popular spacecraft attitude control actuator systems is proposed, namely between the single-gimbal Control Moment Gyroscopes (CMGs) and the Reaction Wheels (RWs). The CMGs are usually more efficient energy wise in controlling large space structures. However, they contain singular gimbal orientations which can cause the feasible torque set produced by the CMG cluster to not include the required torque demanded by the control law.[16–18] Any discrepancy between commanded and realized torque causes the spacecraft to deviate from the desired trajectory, which is unacceptable in some applications. In such cases it has been proposed to augment the CMG control system with thrusters to provide the necessary torque when the spacecraft is operating close to a CMG

singularity. However, thrusters have several drawbacks. They expel propellant which cannot be easily renewed, and are difficult to use when a precision maneuver is being performed. Ford and Hall present in Ref. 19 the dynamical equations of motion of a spacecraft with several Variable Speed Control Moment Gyroscopes (VSCMGs) attached. These devices are essentially single-gimbal CMGs with a variable speed RWs. Their formulation was convenient since it allowed them to quickly develop control laws for *either* CMG or RW case. However, they did not consider the *simultaneous* use of both modes together.

The dynamics of a spacecraft with several VSCMG is presented in this dissertation in a manner that makes it trivial to either switch to either classical case of using *only* RWs or CMGs or retain and use the two modes together. Ideally the VSCMGs should perform like classical CMGs when not in the proximity of CMG singularities since they are more efficient energy wise than the RWs. Whenever a singularity is approached, then the RW mode should be used along with the CMG mode to ensure that the actual torque produced by the VSCMG cluster is equal to the torque demanded by the control law. Two types of steering laws which perform in such a manner will be discussed, a velocity- and an acceleration based control law. The CMGs are typically controlled at the gimbal velocity level to take advantage of the torque amplification effect. However, the dynamical system which leads to the velocity-based steering law ignores the transverse and gimbal VSCMG inertia terms. To provide a more accurate simulation and perform energy consumption studies, the gimbal acceleration based steering law is developed. Further, the use of the VSCMG *null motion* to reorient the gimbal angles away from the proximity of a singularity is discussed. Vadali et. al. discuss in Ref. 20 the existence of preferred gimbal angle sets for which the resulting maneuver will be singularity free. However, the classical CMG null motion of four CMGs in a pyramid configuration is very limited in its ability to

rearrange the gimbal angles without producing an effective torque on the spacecraft, because only one degree of freedom exists. The use of the RW mode allows for far more general reorientations since this approach has five redundant degrees of freedom. While the RW mode of the velocity or acceleration based steering laws might require relatively large torques to pass by CMG singularities, it will be of interest whether or not the VSCMG null motion could be performed with existing CMG hardware (which already include a small RW torque motor and feedback controller to keep the disk spinning at a constant rate). The main question will be: What are the consequences of surrendering the constant speed constraint in favor of variable wheel speeds, with no other design changes? This question can be readily answered using the results of this dissertation.

# CHAPTER II

# STEREOGRAPHIC ORIENTATION PARAMETERS*

A novel family of rigid body attitude parameters called the *Stereographic Parameters* (SPs) were recently developed.[21] It is well known that the Modified Rodrigues Parameters (MRPs) can be found through a stereographic projection of the Euler parameters unit constraint sphere onto an appropriate three-dimensional hyperplane.[8,9] This projection will be discussed in detail in the first section of this chapter. This elegant geometric interpretation of the MRPs can be expanded to generate a whole family of rigid body attitude parameters. As an example, it turns out the classical Rodrigues parameters[6] can also be described through a stereographic projection of the Euler parameter constraint sphere. The second section will briefly discuss these Rodrigues parameters and develop them from the general stereographic parameters. As will be evident in this discussion, the bright shining star of the SPs are the MRPs. The bulk of this chapter will deal with their development and the discussion of their many unique properties, including their use in feedback control laws and optimal control problems. Both the classical and the modified Rodrigues parameters are members of a subset of the SPs called the symmetric SPs. The last section will discuss the properties of the second subset called the asymmetric SPs.

## 2.1 General Stereographic Projection

### *2.1.1 The Euler Parameter Unit Constraint Sphere*

The four Euler parameters (quaternions) are well known in the field of rigid body kinematics, and are thoroughly studied in the literature. It is possible to describe

*Portions of this chapter were published in References 21–26. Authors retained the copyright.

them directly from Euler's principal rotation theorem.[5,27] Let the angle $\Phi$ be the principal rotation angle and the unit vector $\hat{\boldsymbol{e}}$ be the principal rotation axis.

**Theorem 2.1 (Euler's Principal Rotation)** *A rigid body or coordinate reference frame can be brought from an arbitrary initial orientation to an arbitrary final orientation by a single rigid rotation through a principal angle $\Phi$ about the principal axis $\hat{\boldsymbol{e}}$; the principal axis being a judicious axis fixed in both the body and reference frame defined by the initial body position.*

The principal rotation angle $\Phi$ is not unique. There always exists a second principal rotation angle $\Phi'$ defined as the complement of $\Phi$

$$\Phi' = \Phi - 2\pi \tag{2.1}$$

The angles $\Phi$ and $\Phi'$ always differ by 360 degrees. In most cases the magnitude of $\Phi$ is simply chosen to be less than or equal to 180 degrees. In this case $\Phi$ represents the "shorter" principal rotation and $\Phi'$ represents the "longer" rotation. This reflects the fundamental truth that there are always two ways to rotate an object to a specific attitude. The shorter rotation $\Phi$ will have a principal rotation less than 180 degree, while the longer rotation angle $\Phi'$ is the complement of $\Phi$ (more than 180 degrees) in the opposite direction. However, note that both $\Phi$ and $\Phi'$ locate the same unique physical orientation.

The Euler parameters $\beta_i$ are defined in terms of the principal rotation elements as

$$\beta_0 = \cos\frac{\Phi}{2} \qquad \beta_i = e_i \sin\frac{\Phi}{2} \quad i = 1, 2, 3 \tag{2.2}$$

and form a once redundant set of rigid body attitude parameters. The four Euler parameters $\beta_i$ must abide by the holonomic constraint

$$\boldsymbol{\beta}^T\boldsymbol{\beta} = \beta_0^2 + \beta_1^2 + \beta_2^2 + \beta_3^2 = 1 \tag{2.3}$$

This constraint geometrically represents the surface of a four-dimensional unit hypersphere. All Euler parameters therefore lie on the surface of this sphere and some geodesic arc on the sphere surface completely describes any possible rotational motion without any singularities or discontinuities. However, note that the Euler parameter vector $\boldsymbol{\beta}$ is not unique. The mirror image trajectory $-\boldsymbol{\beta}(t)$ describes the identical rotational motion as $\boldsymbol{\beta}(t)$.[5] The negative sign means the corresponding principal rotation is accomplished using $\Phi'$ instead of $\Phi$. Usually this non-uniqueness does not pose any difficulties since both sets have identical properties, correspond to the same physical orientation, and can be solved uniquely once initial conditions are prescribed. However, this non-uniqueness will lead to some very interesting and useful SP properties, when $\boldsymbol{\beta}(t)$ and $-\boldsymbol{\beta}(t)$ are mapped through coordinate transformations.

Because the four Euler parameters satisfy one holonomic constraint, they form a once redundant set of equations. Three parameters are sufficient to describe a general rotation. However, the problem with any set of three parameters is that, as is well known, singularities will occur at certain orientations. Different three-parameter sets distinguish themselves by having different geometric interpretations and, especially, having their singular behavior at different orientations. Also of significance, most three-parameter sets introduce transcendental nonlinearities into the parameterization of the direction cosine matrix and related kinematical relationships. However, the classical Rodrigues parameters and other sets discussed herein involve low degree polynomial nonlinearities in both the direction cosine matrix and associated kinematical differential equation, without approximation. The Euler parameter description

represents an attractive regularization which has no singularity, at the cost of having one extra variable.

### *2.1.2 Stereographic Projection of the 4D Unit Sphere*

If a minimum parameter representation is desired, the four Euler parameters can be reduced to any three parameter set by an appropriate transformation. For example, the 3-1-3 Euler angles or the Rodrigues parameters are very commonly used sets that are easily transformed from the Euler parameters.[5,27] Marandi, Modi and Tsiotras found that the modified Rodrigues parameters are obtained by means of a stereographic projection of the four-dimensional unit constraint sphere onto a three-dimensional hyperplane. To visualize the stereographic projection, imagine a three-dimensional sphere being projected onto a two-dimensional plane (analogous to the Earth map projection problem). A certain point is chosen in the 3-D space called a projection point. Next a 2-D mapping plane is chosen. Every point on the unit sphere is then projected onto the mapping plane by extending a line from the projection point through the point on the unit sphere and intersecting it with the mapping plane.

Figure 2.1 shows only a 2-D to 1-D stereographic projection to keep the illustration simple. The results though can easily be expanded to a four-dimensional sphere since the axes are mutually orthogonal. With all these projections shown in Figure 2.1, the Euler parameter $\beta_0$ is eliminated since the mapping hyperplane normal is chosen to be the $\beta_0$ axis. The resulting projections are labelled *symmetric* projections since the non-singular principal rotation angle range is symmetric about the zero rotation orientation. *Asymmetric* stereographic projections are projections onto a hyperplane with a normal other than the $\beta_0$ axis, and result in a non-symmetric principal rotation angle range. The case where the Euler parameter $\beta_1$, $\beta_2$ or $\beta_3$ is eliminated is discussed in the last section in this chapter.

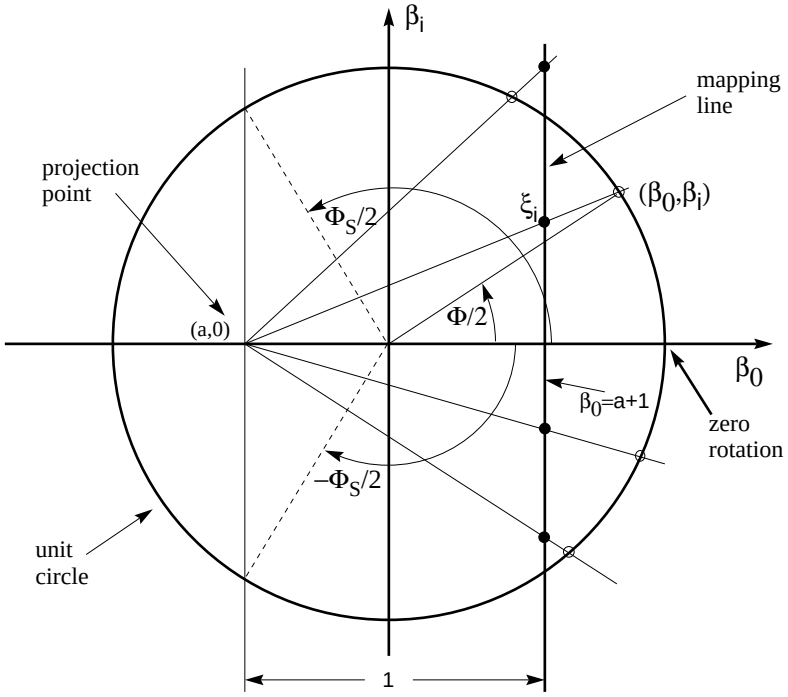


**Fig. 2.1:** Illustration of a Symmetric Stereographic Projection onto Hyperplane Orthogonal to $\beta_0$ axis

Placing the projection point on the $\beta_0$ axis yields a symmetric situation wherein the zero rotation is in the center of the nonsingular principal angle range. The mapping line is placed a distance of +1 from the projection point. The parameters are scaled by this arbitrary distance, so having a distance of 2 between the projection point and the mapping plane would simply scale all the parameters by a factor of 2.

Keep in mind that the Euler parameters are defined in terms of *half* of the principal rotation angle $\Phi$. The point (1,0) on the circle corresponds to a zero rotation. The point (0,1) corresponds to a +180 degree rotation. Studying Figure 2.1 it becomes evident that the reduced parameters go off to infinity when a point on the circle is projected which lies directly in the plane perpendicular to the $\beta_0$ axis through the projection point. The two lines that need to be intersected are parallel to each other causing the intersection point to move to infinity. The corresponding principal

rotation obviously yields the angle at which the reduced set of parameters will go singular! By placing the projection point at different locations on the $\beta_0$ axis, the maximum range of principal rotation angles is varied. If the projection point is outside the unit circle no singularity will occur; however, the resulting projection will no longer be one-to-one. Clearly this is not a desirable feature because of the ambiguity this lack of uniqueness would introduce (given the projected coordinates, we cannot uniquely orient the reference frame).

Let $\boldsymbol{\xi}$ be a stereographic parameter vector and let the angle $\Phi_s$ be the corresponding principal rotation angle where $\boldsymbol{\xi}$ encounters a singularity. This angle $\Phi_s$ is determined by the placement of the projection point $a$.

$$a = \cos\frac{\Phi_s}{2} \tag{2.4}$$

The transformation from the Euler parameters to a general set of three symmetric stereographic parameters $\xi_i$ is defined as

$$\xi_i = \frac{\beta_i}{\beta_0 - a} \qquad i = 1, 2, 3 \tag{2.5}$$

The condition for a singularity to occur with symmetric stereographic parameters is evident in the denominator of Eq. (2.5) and is given by

$$a = \beta_0 = \cos\frac{\Phi}{2} \tag{2.6}$$

If $a < 1$ this condition is satisfied at an infinite set of orientations with the same principal orientation angle $\Phi_s$. If the projection point is on the unit sphere surface, then $a = -1$ and a singularity is only encountered at $\Phi = \pm 360$ degrees. The inverse

transformations from the general SP to the Euler parameters are

$$\begin{aligned}\beta_0 &= \frac{a\boldsymbol{\xi}^T\boldsymbol{\xi} + \sqrt{1+\boldsymbol{\xi}^T\boldsymbol{\xi}\,(1-a^2)}}{1+\boldsymbol{\xi}^T\boldsymbol{\xi}} \\ \beta_i &= \xi_i\left[\frac{-a+\sqrt{1+\boldsymbol{\xi}^T\boldsymbol{\xi}\,(1-a^2)}}{1+\boldsymbol{\xi}^t\boldsymbol{\xi}}\right] \qquad i=1,2,3\end{aligned} \tag{2.7}$$

This equation holds for both the symmetric and asymmetric stereographic projections. Since the Euler parameters are unique only to within a $\pm$ sign, it is equally valid to rewrite Eq. (2.5) in terms of $-\beta_i$. For the general case the resulting stereographic parameters $\boldsymbol{\xi}^S$ correspond to the mirror image of the Euler parameters and are generally numerically distinct of $\boldsymbol{\xi}$ given in Eq. (2.5). However, the resulting vector $\boldsymbol{\xi}^S$ describes the same orientation as the original parameters and are herein referred to as the shadow sets of $\boldsymbol{\xi}$ and are denoted with a superscript $S$.

$$\xi_i^S = \frac{-\beta_i}{-\beta_0 - a} = \frac{\beta_i}{\beta_0 + a} \qquad i=1,2,3 \tag{2.8}$$

This non-uniqueness of the SPs turns out to be very beneficial and allows one to switch between the two possible sets to avoid any singularities. Using Eq. (2.7) the shadow parameter vector $\boldsymbol{\xi}^s$ can be expressed directly as a transformation of the original parameter vector $\boldsymbol{\xi}$ and the projection point $a$ as

$$\xi_i^S = \xi_i\left[\frac{-a+\sqrt{1+\boldsymbol{\xi}^T\boldsymbol{\xi}\,(1-a^2)}}{a+2a\boldsymbol{\xi}^T\boldsymbol{\xi}+\sqrt{1+\boldsymbol{\xi}^T\boldsymbol{\xi}\,(1-a^2)}}\right] \qquad i=1,2,3 \tag{2.9}$$

Note that the distinction between which parameter vector is the original and which is the shadow set is purely arbitrary. Once a particular set is found, the alternate shadow set is found using Eq. (2.9). The fact that the shadow parameter vector $\boldsymbol{\xi}^S$ generally has a different behavior than the original $\boldsymbol{\xi}$ will be useful when describing a rotation. By differentiating Eq. (2.5) the differential kinematic equations of $\boldsymbol{\xi}$ are

found to be

$$\dot{\xi}_i = \frac{\dot{\beta}_i}{\beta_0 - a} - \frac{\beta_i \dot{\beta}_0}{(\beta_0 - a)^2} \qquad i = 1, 2, 3 \tag{2.10}$$

By making use of the differential kinematic equations of the Euler parameters[28]

$$\begin{pmatrix} \dot{\beta}_0 \\ \dot{\beta}_1 \\ \dot{\beta}_2 \\ \dot{\beta}_3 \end{pmatrix} = \frac{1}{2} \begin{bmatrix} \beta_0 & -\beta_1 & -\beta_2 & -\beta_3 \\ \beta_1 & \beta_0 & -\beta_3 & \beta_2 \\ \beta_2 & \beta_3 & \beta_0 & -\beta_1 \\ \beta_3 & -\beta_2 & \beta_1 & \beta_0 \end{bmatrix} \begin{pmatrix} 0 \\ \omega_1 \\ \omega_2 \\ \omega_3 \end{pmatrix} \tag{2.11}$$

and the definition of the stereographic parameters given in Eq. (2.5), the differential kinematic equations for the stereographic parameters are found. Their general form is very lengthy and not shown here. The most important special cases are discussed in the following sections. Viewing Figure 2.1, it becomes evident that a set of three symmetric stereographic parameters cannot have the singularity point moved beyond a principal rotation of $\pm 360$ degrees. Moving the projection point further to the left than $a = -1$ would not result in a one-to-one map onto the projection plane. Therefore the symmetric parameters are better suited for regulator or moderately large departure motion problems, than for spinning body cases. However, this picture corresponds to a rotational scaling of $\Phi/2$. Recent developments in Ref. 24 show that corresponding developments can be carried out for $\Phi/n$ scaling with $n = 2, 3, 4, \ldots$, and thereby the nonsingular range be be moved beyond $\pm 360$ degrees. However, these higher order Rodrigues parameters are no longer the result of a stereographic projection of the Euler parameter unit constraint sphere.

Asymmetric stereographic parameters have a qualitatively different singular behavior from the symmetric stereographic parameters. The Euler parameter $\beta_0$ contains information about the principal rotation angle only (i.e., the direction of $\hat{\boldsymbol{e}}$ does

not affect $\beta_0$). Eliminating $\beta_0$ during a symmetric projection causes the singularity to appear at a certain principal rotation angle only, independent from the principal rotation axis $\hat{\boldsymbol{e}}$. Consequently, symmetric projections have a symmetric range of non-singular principal rotations ($-\Phi_s < \Phi < +\Phi_s$) about the zero rotation, regardless of the direction of $\hat{\boldsymbol{e}}$.

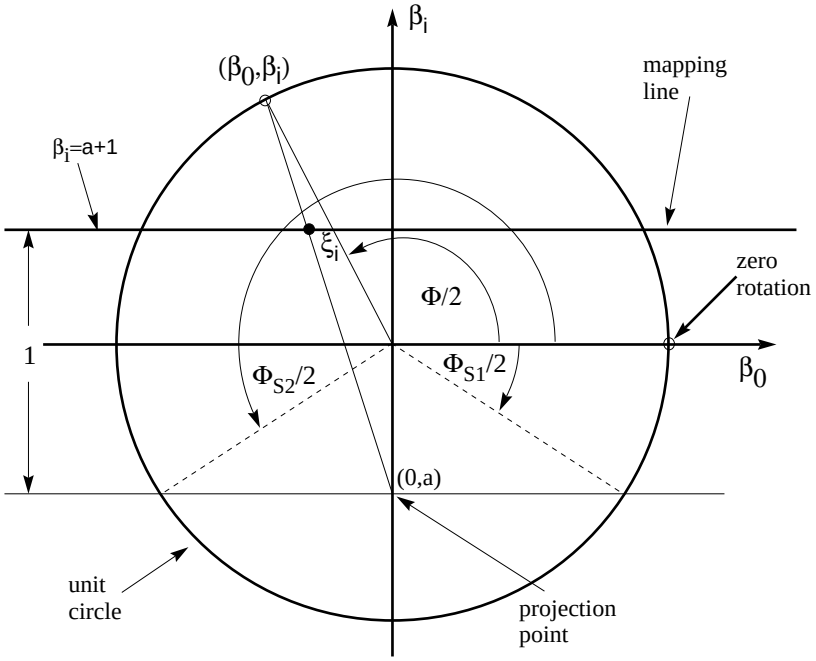


**Fig. 2.2:** Illustration of a Asymmetric Stereographic Projection onto Hyperplane Orthogonal to $\beta_i$ axis

For an asymmetric projection one of the $\beta_1$, $\beta_2$, or $\beta_3$ Euler parameters is eliminated. Each one of these parameters contains information about both the principal rotation angle $\Phi$ and axis $\hat{\boldsymbol{e}}$. Therefore singularities will only occur at certain angles about the $i$-th axis (corresponding to the eliminated $\beta_i$). Figure 2.2 illustrates an asymmetric stereographic projection where $\beta_i$ is eliminated. All possible projections points $a$ now lie on the $\beta_i$ axis, while the mapping hyperplane perpendicular to the $\beta_i$ axis is defined as $\beta_i = a + 1$. Since the zero rotation is no longer in the center of the nonsingular principal angle range, the valid range of principal angles is now

non-symmetric. A singularity will occur at $\Phi_{s_1}$ or $\Phi_{s_2}$, where these two principal angles are unequal in magnitude. Given a singular principal rotation angle $\Phi_{s_1}$ which lies between $\pm 180$ degrees, the corresponding projection point $a$ is defined as

$$a = \cos\frac{\Phi_{s_1}}{2} \tag{2.12}$$

The second singular principal rotation angle $\Phi_{s_2}$ is then found as

$$\Phi_{s_2} = 2\pi - \Phi_{s_1} \tag{2.13}$$

The transformation from Euler parameters to the corresponding asymmetric stereographic parameters is the same as given in Eq. (2.5) with $\beta_0$ and $\beta_i$ switched. A singularity now occurs when $\beta_i$ equals $a$. If the projection point $a$ lies inside the four-dimensional unit sphere, this may occur at several orientations. Using Eq. (2.2), the condition for a singularity becomes

$$e_i \sin\frac{\Phi}{2} = a \tag{2.14}$$

where the index $i$ stands for the $\beta_i$ parameter which was eliminated. Since the sine function is bounded between $\pm 1$, a singularity will never occur if $|e_i| < a$. If the projection point $a$ is moved to the sphere surface, namely to $\pm 1$, then a singularity may occur with a rotation about the $i$-th body axis only! The reason for this is evident in Eq. (2.14). Since a is $\pm 1$ and the sin function is bounded within $\pm 1$, the only way Eq.(2.14) is satisfied is if $|e_i| = 1$. Because $\hat{\boldsymbol{e}}$ is a unit vector, the other two direction components must be zero if $|e_i| = 1$. Thus, if the body is spinning about an axis other than the $i$-th body axis, a singularity will never occur. Therefore these asymmetric stereographic parameters are attractive for spinning body problems where an object is rotating mainly about a certain axis. The principal rotation angle is now not bounded within a closed angle range as with the symmetric stereographic parameters, but can

grow beyond $\pm 360$ degrees. Simply choose the normal of the projection hyperplane to be far removed from the rotation axis and place the projection point a on the four-dimensional unit sphere surface and the probability of encountering a singularity is virtually nil.

For both the symmetric and asymmetric stereographic parameters, having the projection point on the sphere surface means the singularity can only occur at two distinct orientations. If the projection point lies inside the sphere, there generally exists an infinite set of possible singular orientations.

The inverse transformation from asymmetric stereographic parameters to Euler parameters is the same as given in Eq. (2.7). These asymmetric parameters also exhibit the same shadow point behavior as the symmetric parameters do with the same transformations given in Eqs. (2.8) and (2.9). Therefore, if a singular orientation is approached with the asymmetric stereographic parameters, one can again switch to the shadow set to avoid the approaching singularity.

## 2.2 Classical Rodrigues Parameters

The origin of the classical Rodrigues parameter vector $\boldsymbol{q}$ (also known as Gibbs vector) dates back over a hundred years to the French mathematician O. M. Rodrigues.[6] They are well suited to describe most large rotations since their only singularity is for principal rotations of $\Phi = \pm 180$ degrees. It is well know that the modified Rodrigues parameters can be described geometrically through a stereographic projection. What is less widely known is that the classical Rodrigues parameters are also a particular set of SP, and can thus be described through a corresponding stereographic projection as outlined in the previous section. The singularity at $\Phi = \pm 180$ degrees corresponds to a point on the two-dimensional unit circle in Figure 2.1 of $(0,\pm 1)$. Since the singular points are always within a hyperplane which is perpendicular to the $\beta_0$ axis and

contains the projection point $a$, then this projection point $a$ must lie on the origin for $\boldsymbol{\xi}$ to become the classical Rodrigues vector $\boldsymbol{q}$. The corresponding mapping hyperplane is at $\beta_0 = 1$. With this geometrical interpretation it becomes evident why the classical Rodrigues parameters go singular at $\Phi = \pm 180$ degrees when describing them as a special case of the symmetric stereographic parameters. The transformation from the Euler parameters to the Rodrigues parameters is found by setting $\Phi_s = \pm 180$ degrees in Eqs. (2.4) and (2.5). The well known result is given by

$$q_i = \frac{\beta_i}{\beta_0} \qquad i = 1, 2, 3 \tag{2.15}$$

The inverse transformation from the Rodrigues to the Euler parameters is found by using the same $\Phi_s$ in Eq. (2.7).

$$\beta_0 = \frac{1}{\sqrt{1 + \boldsymbol{q}^T \boldsymbol{q}}} \quad \beta_i = \frac{q_i}{\sqrt{1 + \boldsymbol{q}^T \boldsymbol{q}}} \qquad i = 1, 2, 3 \tag{2.16}$$

The differential kinematic equation in terms of the classical Rodrigues parameters is given in vector form as

$$\dot{\boldsymbol{q}} = \frac{1}{2} \left[ I + [\tilde{\boldsymbol{q}}] + \boldsymbol{q}\boldsymbol{q}^T \right] \boldsymbol{\omega} \tag{2.17}$$

where $\boldsymbol{\omega}$ is the body angular velocity vector and $I$ is the $3 \times 3$ identity matrix. The tilde matrix operator $[\tilde{\boldsymbol{q}}]$ is defined by $\boldsymbol{q} \times \ldots$ and is expressed as

$$[\tilde{\boldsymbol{q}}] = \begin{bmatrix} 0 & -q_3 & q_2 \\ q_3 & 0 & -q_1 \\ -q_2 & q_1 & 0 \end{bmatrix} \tag{2.18}$$

Note that only second order polynomial nonlinearities appear in these differential

kinematic equations. An explicit matrix form of Eq. (2.17) is given below.[5]

$$\dot{\boldsymbol{q}} = \frac{1}{2}\begin{bmatrix} 1+q_1^2 & q_1q_2-q_3 & q_1q_3+q_2 \\ q_2q_1+q_3 & 1+q_2^2 & q_2q_3-q_1 \\ q_3q_1-q_2 & q_3q_2+q_1 & 1+q_3^2 \end{bmatrix}\begin{pmatrix} \omega_1 \\ \omega_2 \\ \omega_3 \end{pmatrix} \tag{2.19}$$

Using the definitions of the Euler parameters in Eq. (2.2), the Rodrigues parameters can also be expressed directly in terms of the principal rotation angle $\Phi$ and the principal rotation axis $\hat{\boldsymbol{e}}$.

$$\boldsymbol{q} = \tan\frac{\Phi}{2}\hat{\boldsymbol{e}} \tag{2.20}$$

Studying Eq. (2.20) it is mathematically apparent why the classical Rodrigues parameters go singular at $\Phi = \pm 180$ degrees. For completeness the direction cosine matrix $[C]$ is given in explicit matrix form as[5]

$$[C] = \frac{1}{1+\boldsymbol{q}^T\boldsymbol{q}}\begin{bmatrix} 1+q_1^2-q_2^2-q_3^2 & 2\left(q_1q_2+q_3\right) & 2\left(q_1q_3-q_2\right) \\ 2\left(q_2q_1-q_3\right) & 1-q_1^2+q_2^2-q_3^2 & 2\left(q_2q_3+q_1\right) \\ 2\left(q_3q_1+q_2\right) & 2\left(q_3q_2-q_1\right) & 1-q_1^2-q_2^2+q_3^2 \end{bmatrix} \tag{2.21}$$

and in vector form as[27]

$$[C] = \frac{1}{1+\boldsymbol{q}^T\boldsymbol{q}}\left(\left(1-\boldsymbol{q}^T\boldsymbol{q}\right)I + 2\boldsymbol{q}\boldsymbol{q}^T - 2[\tilde{\boldsymbol{q}}]\right) \tag{2.22}$$

Eq. (2.22) and its inverse can also be written as the very elegant and beautiful Cayley Transform.[5,22,27,29]

$$[C(\boldsymbol{q})] = \left(I-[\tilde{\boldsymbol{q}}]\right)\left(I+[\tilde{\boldsymbol{q}}]\right)^{-1} \tag{2.23}$$

$$[\tilde{\boldsymbol{q}}] = \left(I-[C(\boldsymbol{q})]\right)\left(I+[C(\boldsymbol{q})]\right)^{-1} \tag{2.24}$$

The kinematic differential equation shown in Eqs. (2.17) and (2.19) has the "Cayley"

form[5]

$$\frac{d}{dt}[\tilde{\boldsymbol{q}}] = \frac{1}{2}\left(I - [\tilde{\boldsymbol{q}}]\right)[\tilde{\boldsymbol{\omega}}]\left(I - [\tilde{\boldsymbol{q}}]\right) \tag{2.25}$$

Let the vector $\boldsymbol{q}^S$ (defined with $-\boldsymbol{\beta}$) denote the shadow set of the classical Rodrigues parameters. Using Eq. (2.15), the following definition for the $\boldsymbol{q}^S$ vector is found.

$$q_i^S = \frac{-\beta_i}{-\beta_0} = \frac{\beta_i}{\beta_0} = q_i \qquad i = 1, 2, 3 \tag{2.26}$$

Eq. (2.26) shows that for the classical Rodrigues parameters, the shadow set components are identical to the original Rodrigues parameters, with identical values and properties. Therefore the shadow set concept is of no practical consequence in this particular SP set; however, the classical Rodrigues parameters are unique and their singularity cannot be avoided.

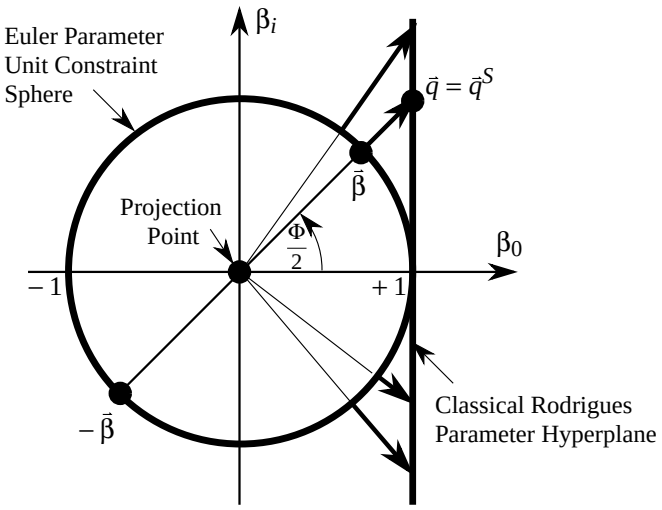


**Fig. 2.3:** Original and Shadow Point Projection of the Classical Rodrigues Parameters

Having the projection point $a$ at the origin causes this elegant, degenerate projection. Figure 2.3 illustrates why both sets of classical Rodrigues parameters are

identical. These Rodrigues parameters are the only symmetric SPs which exhibit this lack of distinction between the original parameters and their image (shadow) point counterparts. This proves simultaneously to be an advantage and a disadvantage.

## 2.3 Modified Rodrigues Parameters

### *2.3.1 Rigid Body Attitude Vector*

The modified Rodrigues parameters discussed by Marandi and Modi in Ref. 8 and Tsiotras in Ref. 9 move the projection point to the negative extreme end of the $\beta_0$ axis at (-1,0,0,0) and project the Euler parameters on the sphere surface onto the hyperplane defined through $\beta_0 = 0$. This results in the MRP singularity being as far away from the zero-rotation as possible. The parameters will now go singular at $\Phi = \pm 360$ degrees. This means that the MRP are able to describe any type of rotation except a complete revolution back to the original orientation. Compare this non-singular range with that of Euler angles where one is never more than a 90 degree rotation away from a singular orientation. The classical Rodrigues parameters go singular when $\Phi = \pm 180$ degrees. On the constraint hypersphere this corresponds to a great circle (hyperline) around the 4-D sphere equator. The attitude description is singular for any 180 degree principal rotation about any principal rotation axis. Contrary to this, the singular MRP condition is not a *hyperline*, but a *point* on the constraint hypersphere. *Only* a complete 360 degree tumbling maneuver back exactly to its original or reference orientation will cause the MRP description to go singular.

Setting $a = -1$ in Eq. (2.5), the transformation from Euler parameters to the modified Rodrigues parameter vector $\boldsymbol{\sigma}$ is given by[9]

$$\sigma_i = \frac{\beta_i}{\beta_0 + 1} \qquad i = 1, 2, 3 \tag{2.27}$$

Using Eq. (2.7), the inverse transformation is found to be

$$\beta_0 = \frac{1-\sigma^2}{1+\sigma^2} \quad \beta_i = \frac{2\sigma_i}{1+\sigma^2} \qquad i = 1,2,3 \tag{2.28}$$

where the notation $\sigma^{2n} = \left(\boldsymbol{\sigma}^T\boldsymbol{\sigma}\right)^n$ is used. Using Eq. (2.2) again, the modified Rodrigues parameters are written as[9]

$$\boldsymbol{\sigma} = \tan\frac{\Phi}{4}\hat{\boldsymbol{e}} \tag{2.29}$$

Studying Eq. (2.29) it is evident that the MRP have a geometric singularity at $\Phi = \pm 360$ degrees. Also note that for small rotations the MRPs linearize as quarter angles[21]

$$\boldsymbol{\sigma} \approx \frac{\Phi}{4}\hat{\boldsymbol{e}} \tag{2.30}$$

It is interesting that $\Phi = 0$ and $\Phi = \pm 360$ degrees correspond physically to the same body orientation. This fact has both theoretical and practical consequences in avoiding the singularity.

The MRP vector $\boldsymbol{\sigma}$ can be transformed directly into the classical Rodrigues parameter vector $\boldsymbol{q}$ through[21]

$$\boldsymbol{q} = \frac{2}{1-\sigma^2}\boldsymbol{\sigma} \tag{2.31}$$

The inverse transformation is given by

$$\boldsymbol{\sigma} = \frac{1}{1+\sqrt{1+\boldsymbol{q}^T\boldsymbol{q}}}\boldsymbol{q} \tag{2.32}$$

Naturally, these forward and inverse transformations go singular at $\Phi = \pm 180$ degrees since the classical Rodrigues parameters description is singular at this orientation. Comparing Eqs. (2.20) and (2.29) it is immediately evident that both the classical and the modified Rodrigues parameter vectors have the same direction $\hat{\boldsymbol{e}}$, but differ in

their magnitude. The transformation shown in Eq. (2.31) can be rewritten in terms of the principal rotation angle $\Phi$ as

$$\boldsymbol{q} = \frac{\tan\frac{\Phi}{2}}{\tan\frac{\Phi}{4}}\boldsymbol{\sigma} \tag{2.33}$$

The direction cosine matrix $[C]$ in terms of the MRPs is given by[9,21,27]

$$[C] = \frac{1}{(1+\sigma^2)^2}\begin{bmatrix} 4\left(\sigma_1^2-\sigma_2^2-\sigma_3^2\right)+\Sigma^2 & 8\sigma_1\sigma_2+4\sigma_3\Sigma & \cdots \\ 8\sigma_2\sigma_1-4\sigma_3\Sigma & 4\left(-\sigma_1^2+\sigma_2^2-\sigma_3^2\right)+\Sigma^2 & \cdots \\ 8\sigma_3\sigma_1+4\sigma_2\Sigma & 8\sigma_3\sigma_2-4\sigma_1\Sigma & \\ & 8\sigma_1\sigma_3-4\sigma_2\Sigma & \\ \cdots & 8\sigma_2\sigma_3+4\sigma_1\Sigma & \\ & 4\left(-\sigma_1^2-\sigma_2^2+\sigma_3^2\right)+\Sigma^2 & \end{bmatrix} \tag{2.34}$$

where $\Sigma = 1-\sigma^2$. In compact vector form $[C]$ is parameterized in terms of the MRP vector $\boldsymbol{\sigma}$ as[21,27]

$$[C] = I + \frac{8[\tilde{\boldsymbol{\sigma}}]^2 - 4\left(1-\sigma^2\right)[\tilde{\boldsymbol{\sigma}}]}{\left(1+\sigma^2\right)^2} \tag{2.35}$$

However, contrary to the classical Rodrigues parameters, the projection of the alternate Euler parameter vector $-\boldsymbol{\beta}$ results in a mathematically and numerically distinct set of shadow MRPs as can be seen in Figure 2.4. Each MRP vector is an equally valid attitude description satisfying the same kinematic differential equation. Therefore one can arbitrarily switch between the two vectors through the mapping[8,21,27]

$$\sigma_i^S = \frac{-\beta_i}{1-\beta_0} = \frac{-\sigma_i}{\sigma^2} \qquad i = 1,2,3 \tag{2.36}$$

where the choice as to which vector is the original and which is the shadow vector is arbitrary. Studying Figure 2.4 it is clear that while one set of MRPs will have a magnitude of 1 or less, their corresponding shadow set will have a magnitude of 1 or

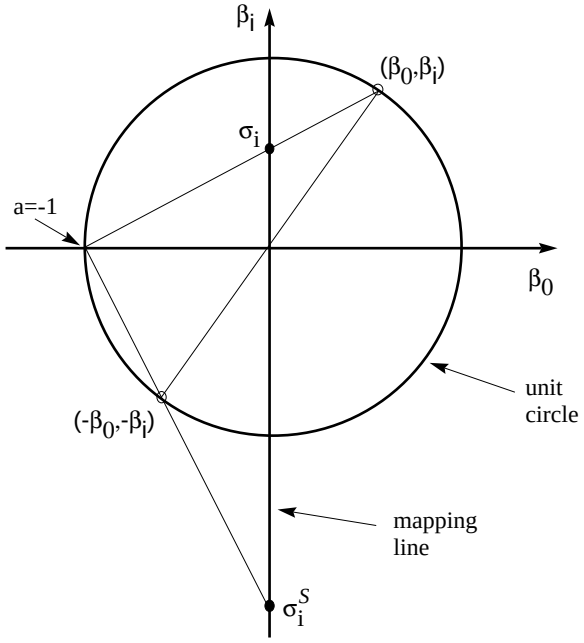


**Fig. 2.4:** Stereographic Projection of Euler Parameters to Modified Rodrigues Parameters

greater. From Eq. (2.29) it evident that

$$\begin{aligned} |\boldsymbol{\sigma}| &\leq 1 \quad if \quad \Phi \leq 180^\circ \\ |\boldsymbol{\sigma}| &\geq 1 \quad if \quad \Phi \geq 180^\circ \\ |\boldsymbol{\sigma}| &= 1 \quad if \quad \Phi = 180^\circ \end{aligned} \tag{2.37}$$

This behavior can also be observed in Figure 2.4. The mapping in Eq. (2.36) can be written in terms of the principal rotation elements using the definitions of $\beta_i$ in Eq. (2.2) as

$$\boldsymbol{\sigma}^S = \tan\left(\frac{\Phi - 2\pi}{4}\right)\hat{\boldsymbol{e}} \tag{2.38}$$

Using Eq. (2.1) this can be written directly in terms of the alternate principal rotation angle $\Phi'$ as

$$\boldsymbol{\sigma}^S = \tan\left(\frac{\Phi'}{4}\right)\hat{\boldsymbol{e}} \tag{2.39}$$

Thus, while one MRP set describes the "shorter" principal rotation, the corresponding shadow MRP set describes the "longer" principal rotation.

Note that the singular behavior of the shadow set is the opposite of that of the original set. As is seen in Figure 2.4, the shadow point of the zero rotation is a singular description while the shadow point of the $\pm 360$ degree principal rotation is non-singular! Therefore the non-uniqueness of the MRPs allows one to avoid their singularities altogether. As one MRP set approaches a singularity, this set can be mapped to the corresponding shadow set through Eq. (2.36). On which surface $\sigma^2 = c$ one switches is arbitrary. However, switching between the two MRP sets whenever the vector $\boldsymbol{\sigma}$ penetrates the surface $\sigma^2 = 1$ has many positive aspects. For one, the mapping between the two MRP vectors simplifies on this surface to the simplest form $\boldsymbol{\sigma}^S = -\boldsymbol{\sigma}$. Further, the magnitude of $\boldsymbol{\sigma}$ will remain bounded above by 1 and the corresponding principal rotation angle $\Phi$ will remain less than or equal to 180 degrees through the condition in Eq. (2.37). Having a bounded norm of an attitude description is useful since it reflects the fundamental fact that two orientations can only differ by a finite rotation. Referring to the MRPs from here on, it will be understood that the combined set of original and shadow MRPs is meant. This combined set forms a non-singular, bounded, minimal attitude description.

### *2.3.2 Differential Kinematic Equations*

The differential kinematic equation of the MRPs is found by substituting Eq. (2.28) into Eq. (2.10). The resulting matrix formulation is[9, 21]

$$\dot{\boldsymbol{\sigma}} = \frac{1}{4}\begin{bmatrix} 1-\sigma^2+2\sigma_1^2 & 2\left(\sigma_1\sigma_2-\sigma_3\right) & 2\left(\sigma_1\sigma_3+\sigma_2\right) \\ 2\left(\sigma_2\sigma_1+\sigma_3\right) & 1-\sigma^2+2\sigma_2^2 & 2\left(\sigma_2\sigma_3-\sigma_1\right) \\ 2\left(\sigma_3\sigma_1-\sigma_2\right) & 2\left(\sigma_3\sigma_2+\sigma_1\right) & 1-\sigma^2+2\sigma_3^2 \end{bmatrix}\begin{pmatrix}\omega_1\\ \omega_2\\ \omega_3\end{pmatrix} \tag{2.40}$$

The MRP kinematic differential equation in vector form is[21,27]

$$\dot{\boldsymbol{\sigma}} = \frac{1}{4}\left[(1-\sigma^2)I + 2[\tilde{\boldsymbol{\sigma}}] + 2\boldsymbol{\sigma}\boldsymbol{\sigma}^T\right]\boldsymbol{\omega} = [B(\boldsymbol{\sigma})]\boldsymbol{\omega} \tag{2.41}$$

Note that the MRPs satisfy a kinematic differential equation very similar to the classical Rodrigues parameters in Eqs. (2.17) and (2.19) with only quadratic nonlinearities present. Further, this same and identical differential equation holds for *both* sets of MRPs, i.e., after switching between original and shadow MRPs, the same differential equation is satisfied. However, the resulting vector $\dot{\boldsymbol{\sigma}}$ will obviously depend on which set of MRPs is being used in Eq. 2.41. Just as a direct mapping exists between $\boldsymbol{\sigma}$ and $\boldsymbol{\sigma}^S$, a direct mapping between $\dot{\boldsymbol{\sigma}}$ and $\dot{\boldsymbol{\sigma}}^S$ is given by[23]

$$\dot{\boldsymbol{\sigma}}^S = -\frac{\dot{\boldsymbol{\sigma}}}{\sigma^2} + \frac{1}{2}\left(\frac{1+\sigma^2}{\sigma^4}\right)\boldsymbol{\sigma}\boldsymbol{\sigma}^T\boldsymbol{\omega} \tag{2.42}$$

Let the matrix $[B]$ map the $\boldsymbol{\omega}$ vector into $\dot{\boldsymbol{\sigma}}$ in Eqs. (2.40) and (2.41). This $[B]$ matrix is near orthogonal for the MRPs, since the inverse of $[B]$ can be written as a scalar times its transpose.

$$[B]^{-1} = \frac{16}{\left(1+\sigma^2\right)^2}[B]^T \tag{2.43}$$

To prove Eq. (2.43), let's study the orthogonality condition $[B][B]^T$. Using Eq. (2.41) this is written as

$$[B][B]^T = \frac{1}{16}\left((1-\sigma^2)I - 2[\tilde{\boldsymbol{\sigma}}] + 2\boldsymbol{\sigma}\boldsymbol{\sigma}^T\right)\left((1-\sigma^2)I + 2[\tilde{\boldsymbol{\sigma}}] + 2\boldsymbol{\sigma}\boldsymbol{\sigma}^T\right) \tag{2.44}$$

where the skew-symmetric matrix property $[\tilde{\boldsymbol{\sigma}}]^T = -[\tilde{\boldsymbol{\sigma}}]$ was used. After carrying out all the matrix multiplications the $[B][B]^T$ expression is reduced to

$$[B][B]^T = \frac{1}{16}\left((1-\sigma^2)^2 I - 4[\tilde{\boldsymbol{\sigma}}]^2 + 4\boldsymbol{\sigma}\boldsymbol{\sigma}^T\right) \tag{2.45}$$

which can be further simplified using the identity $[\tilde{\boldsymbol{\sigma}}]^2 = \boldsymbol{\sigma}\boldsymbol{\sigma}^T - \sigma^2 I$ to

$$[B][B]^T = \frac{(1+\sigma^2)^2}{16} I \tag{2.46}$$

At this point, it is trivial to verify that Eq. (2.43) must hold. The inverse transformation of Eqs. (2.40) and (2.41) then is in matrix notation

$$\boldsymbol{\omega} = \frac{16}{(1+\sigma^2)^2} [B]^T \dot{\boldsymbol{\sigma}} \tag{2.47}$$

and in the more explicit vector form is[27]

$$\boldsymbol{\omega} = \frac{4}{(1+\sigma^2)^2} \left[ (1-\sigma^2) I - 2[\tilde{\boldsymbol{\sigma}}] + 2\boldsymbol{\sigma}\boldsymbol{\sigma}^T \right] \dot{\boldsymbol{\sigma}} \tag{2.48}$$

### *2.3.3 MRP in a Higher Dimensional Setting*

Like the classical Rodrigues parameters, the MRPs can also be used to minimally parameterize a higher-dimensional proper orthogonal matrix $[C]$. Let the $[S]$ be a skew-symmetric matrix. The extended Cayley transform of $[C]$ in terms of $[S]$ is[22,24]

$$[C] = (I - [S])^2 (1 + [S])^{-2} = (I + [S])^{-2} (I - [S])^2 \tag{2.49}$$

where the order of the matrix products is again irrelevant. For the case where $[C]$ is a 3x3 matrix, then $[S]$ is the same as $[\tilde{\boldsymbol{\sigma}}]$, as was shown in Ref. 22. Therefore Eq. (2.49) transforms a higher dimensional proper orthogonal $[C]$ into higher dimensional MRPs.

Unfortunately no direct inverse transformation exists, analogous to Eq. (2.24), for the higher order Cayley transforms.[22] The transformation is achieved indirectly through the matrix $[W]$ which is defined as the proper matrix square root of $[C]$.

$$[C] = [W][W] \tag{2.50}$$

Since $[C]$ is orthogonal, it can be spectrally decomposed as

$$[C] = [V][D][V]^* \tag{2.51}$$

where $[V]$ is the orthogonal eigenvector matrix and $[D]$ is the diagonal eigenvalue matrix with entries of unit magnitude. The "$*$" operator stands for the adjoint operator which performs the complex conjugate transpose of a matrix. The matrix $[W]$ can be computed as

$$[W] = [V] \begin{bmatrix} \ddots & & 0 \\ & \sqrt{[D]_{ii}} & \\ 0 & & \ddots \end{bmatrix} [V]^* \tag{2.52}$$

The eigenvalues of $[C]$ are typically complex conjugate pairs. If the dimension of $[C]$ is odd, then the extra eigenvalue is real. For proper orthogonal matrices it is $+1$ and it's square root is also chosen to be $+1$. The resulting $[W]$ matrix will then itself also be an proper orthogonal matrix. As Ref. 22 shows, the geometric interpretation of $[W]$ is that it represents the same "higher-dimensional" orientation as $[C]$ except that the corresponding principal rotation angles are halved.

The standard Cayley transforms in Eqs. (2.23) and (2.24) can be applied to map $[W]$ into $[S]$ and back.

$$[W] = (I - [S])(I + [S])^{-1} = (I + [S])^{-1}(I - [S]) \tag{2.53}$$

$$[S] = (I - [W])(I + [W])^{-1} = (I + [W])^{-1}(I - [W]) \tag{2.54}$$

Therefore, to obtain a higher-dimensional MRP representation of $[C]$, the matrix $[W]$ must be found first and then substituted into Eq. (2.54). Note that substituting

Eq. (2.53) into Eq. (2.50) a direct forward transformation from $[S]$ to $[C]$ is found.

$$[C] = (I - [S])^2(I + [S])^{-2} = (I + [S])^{-2}(I - [S])^2 \tag{2.55}$$

The kinematic differential equations for $[S]$ are not written directly in terms of $[C]$ as they were for the classical Cayley transform. Instead the $[W]$ matrix is used. Being an orthogonal matrix, it's kinematic differential equation is of the form

$$[\dot{W}] = -[\tilde{\boldsymbol{\Omega}}][W] \tag{2.56}$$

where $[\tilde{\boldsymbol{\Omega}}]$ is the corresponding angular velocity matrix. It is related to the $[\tilde{\boldsymbol{\omega}}]$ matrix in $[\dot{C}] = -[\tilde{\boldsymbol{\omega}}][C]$ through

$$[\tilde{\boldsymbol{\omega}}] = [\tilde{\boldsymbol{\Omega}}] + [W][\tilde{\boldsymbol{\Omega}}][W]^T \tag{2.57}$$

Analogously to Eq. (2.25), the kinematic differential equation of the $[S]$ matrix is given by

$$[\dot{S}] = \frac{1}{2}\left(I + [S]\right)[\tilde{\boldsymbol{\Omega}}]\left(I - [S]\right) \tag{2.58}$$

### *2.3.4 MRP Feedback Control Law*

The modified Rodrigues parameter vector $\boldsymbol{\sigma}$ is very well suited for describing attitude errors in a feedback control law setting. Particularly when very large attitude errors are present, the MRPs are extremely attractive. By switching between the original and shadow MRP set they are able to describe any arbitrary orientation without encountering singularities by only using three parameters instead of four as do the Euler parameters. Adopting the switching surface $\sigma^2 = 1$ bounds the attitude error vector norm within $|\boldsymbol{\sigma}| \leq 1$. This bounded attitude error property is very useful since it makes designing the attitude feedback gain much easier. Choosing the $\sigma^2 = 1$

switching surface also has a big benefit when trying to bring a tumbling rigid body to rest. Conventional attitude parameters such as the Euler angles have no explicit means of determining the shortest rotational distance back to the reference attitude. Consider this one dimensional example. If a rigid body has tumbled past 180 degrees from the reference attitude, it would be much simpler for the control law to just let the body complete the tumble and then bring it to rest as it approaches the reference attitude from the opposite direction. Using MRPs with the $\sigma^2 = 1$ switching surface (in a feedback control law setting) provides a set of attitude coordinates that will naturally do just that. As is shown in the cases in Eq. (2.37), bounding the MRP vector to unit magnitude or less limits corresponding principal rotation angle $\Phi$ to be 180 degrees or less. In other words, these MRPs will always measure the shortest rotational error to the reference attitude, and implicitly seek the shortest angular path to the target state.

#### 2.3.4.1 Unconstrained MRP Feedback Control Law

Let $[I]$ be the rigid body inertia matrix, $\boldsymbol{\omega}(t)$ be the body angular velocity vector and $\boldsymbol{u}(t)$ be some *unconstrained* external torque vector. Euler's rotational equations of motion for a rigid body are given by[5]

$$[I]\dot{\boldsymbol{\omega}} = -[\tilde{\boldsymbol{\omega}}][I]\boldsymbol{\omega} + \boldsymbol{u} \tag{2.59}$$

The vector $\boldsymbol{\sigma}(t)$ measures the attitude error of this rigid body to some reference trajectory which itself is defined through the reference angular velocity vector $\boldsymbol{\omega}_r(t)$. The error $\delta\boldsymbol{\omega}(t)$ in angular velocities is defined as

$$\delta\boldsymbol{\omega} = \boldsymbol{\omega} - \boldsymbol{\omega}_r \tag{2.60}$$

The MRP rate vector $\dot{\boldsymbol{\sigma}}$ and the body angular velocity error vector $\delta\boldsymbol{\omega}$ are then related through

$$\dot{\boldsymbol{\sigma}} = \frac{1}{4}\left[(1-\sigma^2)I + 2[\tilde{\boldsymbol{\sigma}}] + 2\boldsymbol{\sigma}\boldsymbol{\sigma}^T\right]\delta\boldsymbol{\omega} \tag{2.61}$$

The Lyapunov function[9,21,25]

$$V(\boldsymbol{\omega},\boldsymbol{\sigma}) = \frac{1}{2}\delta\boldsymbol{\omega}^T[I]\delta\boldsymbol{\omega} + 2K\log\left(1+\boldsymbol{\sigma}^T\boldsymbol{\sigma}\right) \tag{2.62}$$

provides a positive definite, radially unbounded measure of the rigid body state error relative to the reference trajectory. The use of the logarithm function was introduced by P. Tsiotras in Ref. 9 and results in a feedback control law which is *linear* in the attitude error vector $\boldsymbol{\sigma}$. The parameter $K$ is a positive *scalar* attitude feedback gain. The derivative of $2K\log\left(1+\boldsymbol{\sigma}^T\boldsymbol{\sigma}\right)$ is

$$\frac{d}{dt}\left(2K\log\left(1+\boldsymbol{\sigma}^T\boldsymbol{\sigma}\right)\right) = 2K\frac{1}{1+\boldsymbol{\sigma}^T\boldsymbol{\sigma}}2\boldsymbol{\sigma}^T\dot{\boldsymbol{\sigma}} \tag{2.63}$$

After using differential kinematic equations for the MRPs in Eq. (2.41) this is simplified to

$$\begin{aligned}\frac{d}{dt}\left(2K\log\left(1+\boldsymbol{\sigma}^T\boldsymbol{\sigma}\right)\right) &= \frac{4K}{1+\boldsymbol{\sigma}^T\boldsymbol{\sigma}}\boldsymbol{\sigma}^T\frac{1}{4}\left[(1-\sigma^2)I + 2[\tilde{\boldsymbol{\sigma}}] + 2\boldsymbol{\sigma}\boldsymbol{\sigma}^T\right]\delta\boldsymbol{\omega} &(2.64)\\ &= \frac{K}{1+\boldsymbol{\sigma}^T\boldsymbol{\sigma}}\left((1-\boldsymbol{\sigma}^T\boldsymbol{\sigma}) + 2\boldsymbol{\sigma}^T\boldsymbol{\sigma}\right)\boldsymbol{\sigma}^T\delta\boldsymbol{\omega} &(2.65)\\ &= K\boldsymbol{\sigma}^T\delta\boldsymbol{\omega} &(2.66)\end{aligned}$$

After differentiating $V$ and using Eqs. (2.61) and (2.66), $\dot{V}$ is expressed as

$$\dot{V} = \delta\boldsymbol{\omega}^T\left([I]\delta\dot{\boldsymbol{\omega}} + K\boldsymbol{\sigma}\right) \tag{2.67}$$

Upon forcing $\dot{V}$ to be negative semi-definite through the use of the positive definite angular velocity feedback gain matrix $[P]$

$$\dot{V} = -\delta\boldsymbol{\omega}^T[P]\delta\boldsymbol{\omega} \tag{2.68}$$

the following stability constraint is found.

$$[I]\delta\dot{\boldsymbol{\omega}} + [P]\delta\boldsymbol{\omega} + K\boldsymbol{\sigma} = 0 \tag{2.69}$$

After substituting the rigid body dynamics in Eq. (2.59) into Eq. (2.69), the feedback control $\boldsymbol{u}$ is given by

$$\boldsymbol{u} = -K\boldsymbol{\sigma} - [P]\delta\boldsymbol{\omega} + [I]\dot{\boldsymbol{\omega}}_r + [\tilde{\boldsymbol{\omega}}][I]\boldsymbol{\omega} \tag{2.70}$$

Note that if the reference trajectory is a stationary attitude then the feedback control law is simplified to[9,21]

$$\boldsymbol{u} = -K\boldsymbol{\sigma} - [P]\delta\boldsymbol{\omega} \tag{2.71}$$

The last term in Eq. (2.70) is not needed here since for this case this gyroscopic term is non working ($\boldsymbol{\omega}^T[\tilde{\boldsymbol{\omega}}][I]\boldsymbol{\omega}$ is zero).

Since $\dot{V}$ in Eq. (2.68) is only negative semi-definite, it can only be concluded at this point that the control law $\boldsymbol{u}$ in Eq. (2.70) is globally stabilizing. To prove that it is indeed globally asymptotically stabilizing, the higher time derivatives of the Lyapunov function $V$ must be investigated. A sufficient condition to guarantee asymptotic stability is that the first nonzero higher-order derivative of $V$, evaluated on the set of states such that $\dot{V}$ is zero, must be of odd order and be negative definite.[28,30,31] For this dynamical system $\dot{V}$ is zero if $\delta\dot{\boldsymbol{\omega}}$ is zero. Differentiating

Eq. (2.68) yields

$$\frac{d^2}{dt^2}V = -2\delta\boldsymbol{\omega}^T[P]\delta\dot{\boldsymbol{\omega}} \tag{2.72}$$

which is zero for the set where $\delta\boldsymbol{\omega}$ is zero. Differentiating again the third derivative of the Lyapunov function $V$ is

$$\frac{d^3}{dt^3}V = -2\delta\boldsymbol{\omega}^T[P]\delta\ddot{\boldsymbol{\omega}} - 2\delta\dot{\boldsymbol{\omega}}^T[P]\delta\dot{\boldsymbol{\omega}} \tag{2.73}$$

Substituting Eq. (2.69) into Eq. (2.73) and setting $\delta\boldsymbol{\omega} = 0$, the third derivative of the Lyapunov function is expressed as

$$\frac{d^3}{dt^3}V = -K^2\boldsymbol{\sigma}^T\left([I]^{-1}\right)[P][I]\boldsymbol{\sigma} \tag{2.74}$$

which is a negative definite quantity (on the $\delta\boldsymbol{\omega} = 0$ set) since both $[I]$ and $[P]$ are positive definite matrices. Therefore the control law $\boldsymbol{u}$ in Eq. (2.70) is globally asymptotically stabilizing.

To determine appropriate feedback gains, the closed loop dynamics are studied. Substituting the feedback control law $\boldsymbol{u}$ given in Eq. (2.70) into Eq. (2.59) the closed loop dynamics for the controlled rigid body are[25]

$$[I]\delta\dot{\boldsymbol{\omega}} = -[P]\delta\boldsymbol{\omega} - K\boldsymbol{\sigma} \tag{2.75}$$

Note that thanks to the use of the MRPs and the logarithm function in Eq. (2.62), the closed loop dynamics are *rigorously linear* in both the body angular velocity and attitude error vectors. Eq. (2.75) is solved along with Eq. (2.41) to determine the exact closed-loop performance. The only nonlinearities that appear in these two differential equations are the quadratic nonlinearities present in the MRP kinematic

differential equation. Linearizing Eq. (2.41) about $\boldsymbol{\sigma}= 0$ yields

$$\dot{\boldsymbol{\sigma}} \simeq \frac{1}{4}\boldsymbol{\omega} \tag{2.76}$$

Since the MRPs "behave like angles over four" for small angles, this linearization will be applicable for a relatively large range of rotations. As a comparison, the classical Rodrigues parameters only linearize as angles over two, whereas the standard Euler angles simply linearize as angle type quantities.

The linearized set of closed loop equations is

$$\begin{pmatrix} \dot{\boldsymbol{\sigma}} \\ \delta\dot{\boldsymbol{\omega}} \end{pmatrix} = \begin{bmatrix} 0 & \frac{1}{4}I \\ -K[I]^{-1} & -[I]^{-1}[P] \end{bmatrix} \begin{pmatrix} \boldsymbol{\sigma} \\ \delta\boldsymbol{\omega} \end{pmatrix} \tag{2.77}$$

Given the rigid body inertia matrix $[I]$, any standard linear control design method such as a pole placement method can be used to determine the desired response of the linearized closed loop dynamics. If both the inertia matrix $[I]$ and the angular velocity feedback gain matrix $[P]$ are diagonal matrices with entries $I_i$ and $P_i$ respectively, then Eq. (2.77) can be conveniently decoupled into three sets of two differential equations[25]

$$\begin{pmatrix} \dot{\boldsymbol{\sigma}}_i \\ \delta\dot{\boldsymbol{\omega}}_i \end{pmatrix} = \begin{bmatrix} 0 & \frac{1}{4} \\ -\frac{K}{I_i} & -\frac{P_i}{I_i} \end{bmatrix} \begin{pmatrix} \boldsymbol{\sigma}_i \\ \delta\boldsymbol{\omega}_i \end{pmatrix} \qquad i = 1,2,3 \tag{2.78}$$

whose roots are explicitly given by

$$\lambda_i^{1/2} = -\frac{1}{2I_i}\left(P_i \pm \sqrt{-KI_i + {P_i}^2}\right) \qquad i = 1,2,3 \tag{2.79}$$

For an underdamped system, the corresponding natural frequencies $\omega_{n_i}$ and damping ratios $\xi_i$ are

$$\omega_{n_i} = \frac{1}{2I_i}\sqrt{KI_i - 2P_i^2} \tag{2.80}$$

$$\xi_i = \frac{P_i}{\sqrt{KI_i - 2P_i^2}} \tag{2.81}$$

The decay time constants $T_i$ which indicates how long it would take for the state error to decay to $\frac{1}{e}$ of its initial value is given by

$$T_i = \frac{2I_i}{P_i} \tag{2.82}$$

It is interesting to note that only the angular velocity feedback gain constants $P_i$ dictate how fast the state errors will decay. The attitude feedback gain constant $K$ contributes to the natural frequency and damping ratios of the closed loop response. The damped natural frequency $\omega_{d_i}$ is given by

$$\omega_{d_i} = \frac{1}{2I_i}\sqrt{KI_i - P_i^2} \tag{2.83}$$

Other methods exist to achieve linear closed loop equations. In Ref. 32 Paielli and Bach first start out with linear, stable, second order differential equation in terms of the attitude error vector and then extract the rigid body dynamics. However, their corresponding nonlinear control input contains higher order polynomial nonlinearities, and is not of the simple form as the control presented in Eq. (2.71). Further, since they are essentially feeding back the Gibbs vector as a attitude error measure, their control law has numerical difficulties for $\Phi = \pm 180$ degrees. While the closed loop dynamics presented here are not perfectly linear, they linearize very well for a large range of rotations while retaining a rather simple control formulation.

The use of the feedback control law in Eq. (2.70), along with the design of the feedback gains, is illustrated in the following numerical simulation. Assume a rigid body with body axes aligned along the principal axes is initially in a tumbling situation. The reference trajectory is set to be the zero attitude at rest. The parameter values for the numerical simulation are shown in Table 2.1. The relative orientation

of the rigid body to the zero attitude is expressed through the MRP vector $\boldsymbol{\sigma}$. Note that the rigid body has a large initial angular velocity about the first body axis which will cause the body to tumble through the $\Phi = 180$ degree orientation. Other three-parameter sets of attitude coordinates cannot describe arbitrary rotations without encountering singularities. For example, had the classical Rodrigues parameters been used in the simulation they would early on encounter a singularity at $\Phi = 180$ degrees.

**Table 2.1:** Parameter of MRP Control Law Numerical Simulation

| Parameter | Value | Units |
|---|---|---|
| $I_1$ | 140.0 | kg-m$^2$ |
| $I_2$ | 100.0 | kg-m$^2$ |
| $I_3$ | 80.0 | kg-m$^2$ |
| $\boldsymbol{\sigma}(t_0)$ | [0.60 $-$0.40 0.20] | |
| $\boldsymbol{\omega}(t_0)$ | [0.70 0.20 $-$0.15] | rad/sec |
| $[P]$ | [18.67 2.67 10.67] | kg-m$^2$/sec |
| $K$ | 7.11 | kg-m$^2$/sec$^2$ |

The feedback gains for this simulation were chosen such that the closed loop dynamics will be very underdamped. Clearly the resulting performance would not be what is needed to control a real system. However, having clearly visible state oscillations present will allow for the predicted damped natural frequency in Eq. (2.83) and decay time constants in Eq. (2.82) to be verified.

The results of the numerical simulation are shown in Figure 2.5. The control vector $\boldsymbol{u}$ stabilizes the tumbling rigid body and brings it to rest at the zero attitude. The decay time constant $T_2$, which controls how fast the states $\sigma_s$ and $\omega_s$ are reduced, was chosen purposely to be much larger than the other two time constants. This results in the second body axis state errors being reduced much slower than the other two, simulating a situation where less control authority is present about this axis. As is seen in Figures 2.5(i) and 2.5(ii) the nonlinear response corresponds very well with the linearized prediction. As the body tumbles through the "upside down" orientation

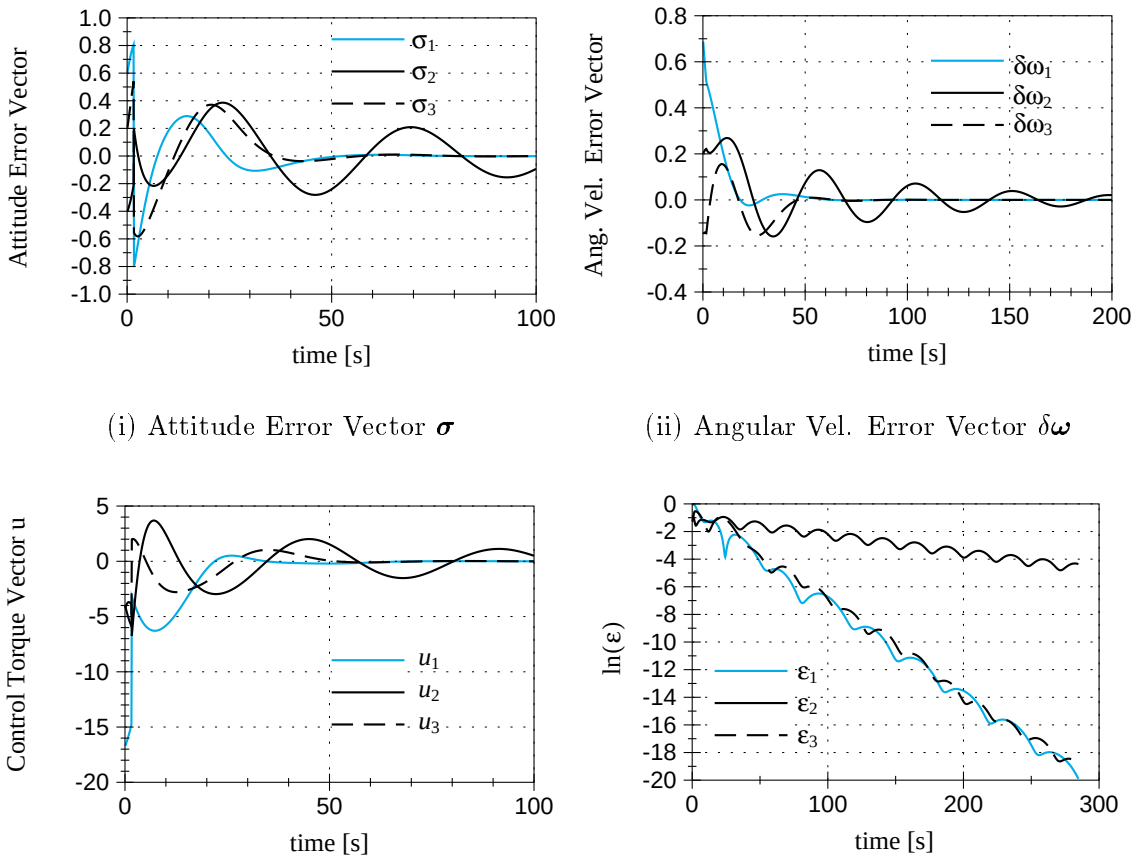


(i) Attitude Error Vector $\boldsymbol{\sigma}$

(ii) Angular Vel. Error Vector $\delta\boldsymbol{\omega}$

(iii) Feedback Control Vector $\boldsymbol{u}$

(iv) State Error Vector $\boldsymbol{\epsilon}$

**Fig. 2.5:** MRP Feedback Control Law Simulation Without Control Constraints

at $\Phi$= 180 degrees, the MRP vector switches to the alternate set. At this point the corresponding control law ceases to fight the tumble and lets the body complete the revolution before bringing it to rest at the origin as seen in Figure 2.5(iii).

Let vector $\boldsymbol{\epsilon}$ be the state error vector whose components are given by

$$\epsilon_i = \sqrt{\sigma_i^2 + \omega_i^2} \qquad i = 1, 2, 3 \tag{2.84}$$

To study the damped natural frequencies $\omega_{d_i}$ and the decay times $T_i$ the natural logarithm of $\epsilon_i$ is plotted in Figure 2.5(iv). This Figure clearly shows the decay rate

**Table 2.2:** Comparison of True vs. Linearized Decay Times and Damped Natural Frequencies

| Parameter | Actual Averaged Value | Linearized Prediction | Percent Difference |
|---|---|---|---|
| $T_1$ | 14.71 s | 15.00 s | 1.97% |
| $T_2$ | 76.92 s | 75.00 s | -2.50% |
| $T_3$ | 14.71 s | 15.00 s | 1.97% |
| $\omega_{d_1}$ | 0.0938 rad/s | 0.0909 rad/s | -3.12% |
| $\omega_{d_2}$ | 0.1326 rad/s | 0.1326 rad/s | 0.08% |
| $\omega_{d_3}$ | 0.1343 rad/s | 0.1333 rad/s | -0.74% |

and the natural oscillations of the underdamped response.

Note that the simulated maneuver performs a very large rotation which includes a complete tumble. Typically, when studying the closed loop response of a control law, only small attitude errors in the order of 10s of degrees are used. Table 2.2 compares the actual averaged decay rates and damped natural frequencies of the nonlinear system to the ones predicted by the linearized feedback gain design. As expected, the linearization used in Eq. (2.76) yields accurate closed loop performance predictions. The percent differences between the actual nonlinear $T_i$ and $\omega_{d_i}$ and the ones obtained from the linearized model are only in the 1 to 2 percent range. Thus the MRP feedback law in Eq. (2.70) achieves global, asymptotic stability by only using three attitude coordinates as compared to four coordinates required by Euler parameter feedback laws. Some control laws using other three parameter sets of attitude coordinates such as the standard yaw, pitch and roll angles also claim to have global stability. However, they all come with a disclaimer warning against rotating the rigid body to certain attitudes because of the inherent singularities of the chosen attitude coordinates. Such control laws can therefore hardly be considered globally stabilizing. The MRP attitude description allows for arbitrary rotations and has the added benefit of always indicating the shortest rotational distance back to the origin when the switching surface $\sigma^2 = 1$ is chosen.

#### 2.3.4.2 MRP Feedback Control Law with Control Constraints

As expected, the control effort required to stabilize a tumbling rigid body can be quite large as is seen in Figure 2.5(iii). Most control devices typically have an upper bound on how much control authority they can exert onto the rigid body. As discussed in Ref. 26, there are essentially two possibilities in dealing with saturated control torques. One solution is to reduce the angular velocity and attitude feedback gains such that the required torque about each axis never exceeds the maximum allowable torque. However, this method has the drawback that the overall performance of the feedback law is greatly reduced.

A more efficient method of dealing with saturated controls is to allow the control about each individual axis to become saturated. This leads to a saturated control law which is Lyapunov optimal. Being Lyapunov optimal means that the time derivative of the given Lyapunov function $V$ is made as negative as possible during intervals where one or more of the control devices are saturated.[26,33–35] Substituting the rigid body equations of motion into Eq. (2.67), $\dot{V}$ is expressed as

$$\dot{V} = \delta\boldsymbol{\omega}^T \left(-[\tilde{\omega}][I]\boldsymbol{\omega} + \boldsymbol{u} - [I]\boldsymbol{\omega}_r + K\boldsymbol{\sigma}\right) \tag{2.85}$$

Since we are now dealing with a tumbling rigid body where the control will be at times saturated, during these intervals we do not attempt to track some reference trajectory, but simply set $\boldsymbol{\omega}_r(t)$ equal to zero. This allows $\dot{V}$ to be simplified along these saturation to

$$\dot{V} = \boldsymbol{\omega}^T \left(\boldsymbol{u} + K\boldsymbol{\sigma}\right) \tag{2.86}$$

The control torque $\boldsymbol{u}_{us}$ for unsaturated conditions is set equal to Eq. (2.71)

$$\boldsymbol{u}_{us} = -K\boldsymbol{\sigma} - [P]\boldsymbol{\omega} \tag{2.87}$$

Recall that $u_{us}$ for unsaturated conditions was shown to be globally, asymptotically stabilizing. Assume that the available control torque about the $i$-th body axis is now limited by $u_{max_i}$. A saturated control law is augmented with the unsaturated control law $u_{us_i}$ to form[26]

$$u_i = \begin{cases} u_{us_i} & \text{if} \quad |u_{us_i}| \leq u_{max_i} \\ u_{max_i} \cdot sign\left(u_{us_i}\right) & \text{if} \quad |u_{us_i}| > u_{max_i} \end{cases} \tag{2.88}$$

Without the unsaturated control term chattering about the reference state would be an issue. Note that it is possible for the control law to be saturated about one body axis, but not about the other two. Stability of this saturated control law is guaranteed if $\dot{V}$ in Eq. (2.86) can be kept negative. The control law in Eq. (2.88) will render $\dot{V}$ as negative as possible during saturation and is therefore *Lyapunov optimal* during these sub intervals for fixed $K$ and $[P]$. A conservative stability condition is found by studying $\dot{V}$ in Eq. (2.86):

$$K|\sigma_i| \leq u_{max_i} \tag{2.89}$$

Since the magnitude of the MRP attitude error vector $\boldsymbol{\sigma}$ is bounded by 1, this stability condition can also be written as

$$K \leq u_{max_i} \tag{2.90}$$

As shown in Ref. 26, while this condition in Eq. (2.89) guarantees stability, it it not a necessary condition for stability. If one simply wanted to stop the tumbling motion without regard to the final attitude, then one could set $K = 0$ and be guaranteed global asymptotic stability with the saturated control law in Eq. (2.88).

However, limiting $K$ through the stability condition in Eq. (2.90) is usually overly conservative. As the following numerical simulation will illustrate, having a

$K > u_{max_i}$ still typically leads to an asymptotically stable closed-loop dynamics. The reason for this is the bounded nature of the attitude error vector. The stability condition in Eq. (2.89), and therefore the requirement of $\dot{V}$ being negative, may indeed be locally violated for finite periods of time. These violations are likely to occur whenever the rigid body tumbles towards the $\Phi = \pm 180$ degrees condition. After the body tumbles past $\Phi = \pm 180$ degrees, the sign of attitude vector components are switched through $\sigma^S = -\sigma$. As is seen in Figure 2.5(iii), the required unsaturated control torque drops drastically in magnitude during this switching. Before the switching, where the body is still rotating away from the origin, both the angular velocity and the attitude feedback are demanding a control torque in the same direction and their effects are added up to produce the large control torque before the switching. After the switching at the $\sigma^2 = 1$ surface, the body now starts to rotate back towards the origin and the sign of the attitude feedback control is switched. This results in the angular velocity and attitude feedback control partially cancelling each other and therefore producing a much smaller control torque. Therefore the required control torques are larger and more likely to be saturated approaching $\Phi = \pm 180$ degrees then they are leaving the "upside-down orientation." Since the body is tumbling, the $\boldsymbol{\sigma}$ vector magnitude will always periodically come close to zero where the stability condition in Eq. (2.89) is satisfied and kinetic energy is guaranteed to be pumped out of the system. Eventually, after *several* revolutions or tumbles, the body will come to rest.

To illustrate this behavior, the following numerical simulation uses the same parameters in Table 2.1 as the previous unsaturated simulation used. The only difference is that now the saturated control law given in Eq. (2.88) will be used. The maximum allowable torque about all three body axes is set to $u_{max_i} = 1$. The numerical simulation results are shown in Figure 2.6.

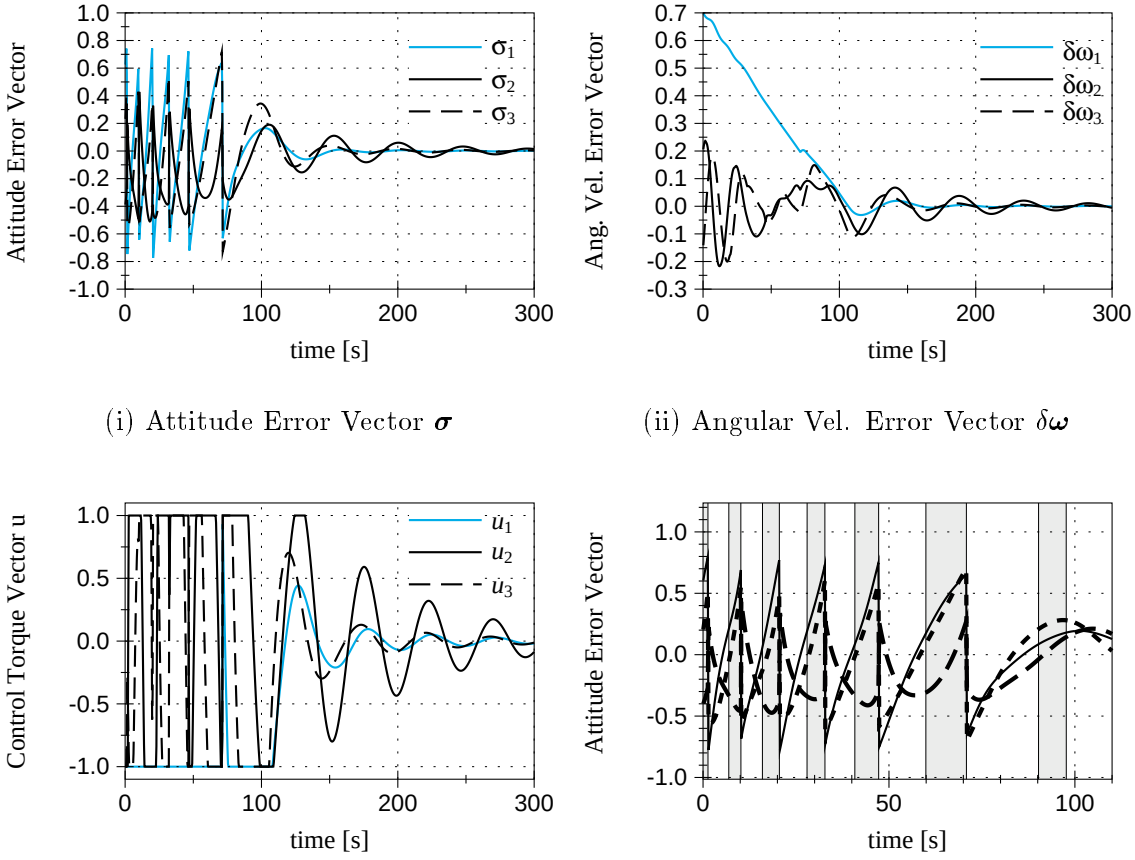


(i) Attitude Error Vector $\boldsymbol{\sigma}$

(ii) Angular Vel. Error Vector $\delta\boldsymbol{\omega}$

(iii) Feedback Control Vector $\boldsymbol{u}$

(iv) Illustration of Regions where $\dot{V} > 0$

**Fig. 2.6:** Saturated MRP Feedback Control Law Simulation

As Figure 2.6(i) shows, with the limited control effort present the rigid body now performs about five tumbles before coming to rest at the origin. The large initial body angular velocity about the first body axis is gradually reduced until the control torque $\boldsymbol{u}$ remains in the unsaturated regime. As shown in Figure 2.6(ii), from there on $\omega_1$ starts to exhibit the anticipated underdamped oscillations as were present with the unsaturated control law. For the first 100 seconds into the simulation the control torque components $u_i$ remain mostly saturated as shown in Figure 2.6(iii). Once the angular velocity errors are sufficiently reduced, the required control effort remains in

the unsaturated regime. Figure 2.6(iv) shows the MRP attitude vector components for up to 120 seconds into the simulation. In the background the time regions are grayed out where the Lyapunov function time derivative $\dot{V}$ is actually positive for this dynamical system. As predicted, $\dot{V}$ becomes temporarily positive when the rigid body is rotating towards the "upside-down" orientation. As soon as the body rotates past this orientation $\dot{V}$ becomes negative again. This happens even though the control torque vector components $u_i$ are mostly still saturated.

Therefore, even though $K$ was chosen to be much larger than $u_{max_i} = 1$ for this simulation, the saturated control law in Eq. (2.88) still asymptotically stabilized the rigid body. One beautiful property of this MRP feedback control law is that not only does it perform well for small orientation errors, it also scales well to handle the much tougher problem of *arbitrary* orientation in the presence of control saturation.

### *2.3.5 MRPs in Optimal Control Problems*

Solutions of spacecraft optimal control problems, whose cost functions rely on an attitude description, usually depend on the choice of attitude coordinates used. Coordinate choices are often considered a matter of taste, but the question of coordinate "optimality" arises. For example, a problem could be solved using 3-2-1 Euler angles or using classical Rodrigues parameters and yield two different "optimal" solutions unless care is taken to ensure that the performance index is invariant with respect to the attitude coordinate choice. Another problem arising with many attitude coordinates is that the resulting control formulation has no intrinsic sense of when a body has tumbled beyond $\pm 180$ degrees from the reference attitude. In many such cases it would be simpler and cheaper to let the body complete the revolution rather than force it to reverse the rotation and return to the desired attitude; it is desirable that attitude error be measured in a fashion consistent with this truth.

Schaub et. al. in Ref. 23 develop a universal attitude penalty function $g()$ which renders the resulting optimal rigid body attitude maneuver independent of the choice of attitude coordinates. This penalty function is defined at the most basic level in terms of the direction cosine matrix $[C]$ as

$$g([C]) = \frac{1}{4}(3 - trace([C])) \quad \in \Re^+ \tag{2.91}$$

By expressing the $[C]$ matrix in terms of other attitude coordinates, the attitude penalty function $g()$ is written in terms of these coordinates. No matter what attitude coordinates are used, for a given attitude error the $g()$ function will return the same scalar attitude penalty. Using Eq. (2.34), the function $g(\boldsymbol{\sigma})$ is written as[23]

$$g([C(\boldsymbol{\sigma})]) = 4\frac{\boldsymbol{\sigma}^T\boldsymbol{\sigma}}{(1+\boldsymbol{\sigma}^T\boldsymbol{\sigma})^2} \tag{2.92}$$

Ref. 23 provides several other parameterizations of the universal $g()$ function. Written in terms of the principal rotation elements, it is written as

$$g([C(\hat{e},\phi)]) = \sin^2(\frac{\phi}{2}) \tag{2.93}$$

As Eq. (2.93) shows, the penalty function $g()$ depends only on the corresponding principal rotation angle $\Phi$ and *not* the principal rotation axis $\hat{\boldsymbol{e}}$. Besides returning the same penalty for a given physical attitude regardless of the choice of attitude coordinates, this attitude penalty function has several other benefits. It provides a bounded scalar measure of the attitude which ranges from 0 for a zero rotation to 1 for a $\pm 180$ degree rotation as is shown in Figure 2.7(i). This boundedness is attractive since it mirrors the fundamental truth that two orientations can only differ by a finite amount. This attitude error measure handles the case of a generally tumbling body well since the attitude penalty is reduced automatically once the body rotates through $\Phi = 180$ degrees.

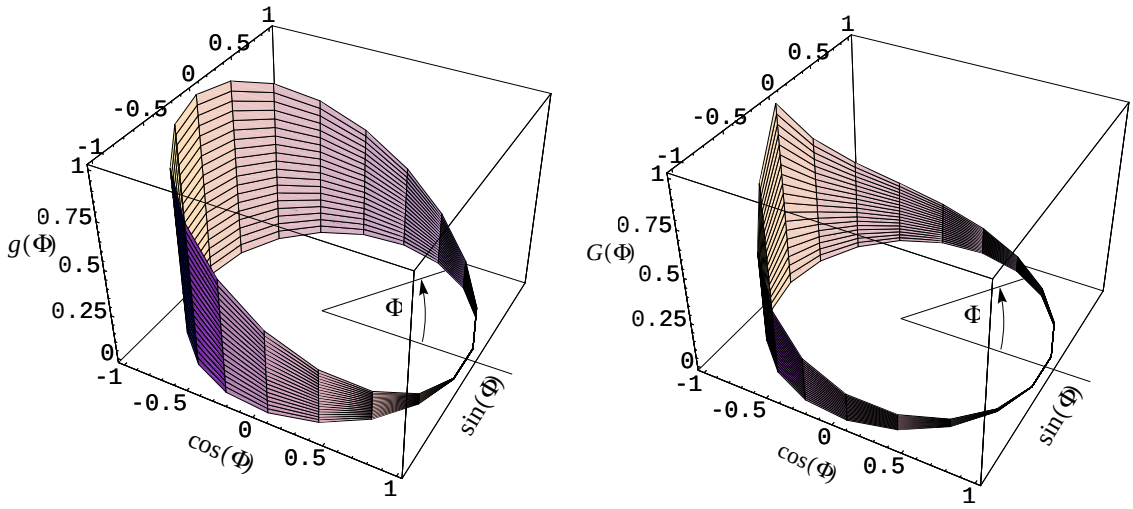


(i) Attitude Penalty Function $g()$ (ii) MRP Attitude Penalty Function $G()$

**Fig. 2.7:** Illustration of Attitude Penalty Function vs. the Principal Rotation Angle $\Phi$

One drawback of $g()$ is that, depending on the choice of attitude coordinates, the resulting expression is generally more complicated than the standard use of the sum squared of all the attitude coordinates. The simpler attitude penalty function[23]

$$G(\boldsymbol{\sigma}) = \boldsymbol{\sigma}^T \boldsymbol{\sigma} \tag{2.94}$$

provides the same benefits as does the more complex $g()$, such as being bounded between 0 and 1 and handling the case of a tumbling rigid body well. The exception of course is that the optimal trajectory, obtained with $G()$ in the optimal control formulation, will no longer be independent of the attitude coordinate choice. Using Eq. (2.29) the function $G()$ is written in terms of $\Phi$ as

$$G(\Phi) = \tan^2 \frac{\Phi}{4} \tag{2.95}$$

which is illustrated in Figure 2.7(ii).

With either attitude penalty function the MRP vector $\boldsymbol{\sigma}$ provides for a convenient way to express any arbitrary orientation with a minimal set of three parameters. Euler parameters can also naturally express any orientation without encountering singularities. However, their being once redundant can cause some analytical and numerical problems when solving optimal control problems.[5] While these issues have been addressed, it would be attractive to be able to use a non-redundant three-parameter set to describe rigid body attitudes singularity free in optimal control problems. On the other hand, the use of MRPs in optimal control problems brings up a new difficulty. Since the MRPs are rendered nonsingular and bounded by introducing the notion of switching to the shadow set, the $\boldsymbol{\sigma}$ vector will be discontinuous during this switching. Of particular importance to solving optimal control problems is that the MRP switch will result in discontinuous partial derivatives of the accelerations with respect to these attitude coordinates. Such discontinuous behavior can in principle be accommodated rigorously in optimal control theory. This section will develop the necessary MRP costate switching condition that will allow MRPs along with their shadow counterparts to be used in optimal control problems.

#### 2.3.5.1 Optimal Control Problem Statement

Most spacecraft optimal control problems have a cost function $J$ which depends on the control effort, the body angular velocity, and the attitude coordinates. Let $\boldsymbol{u}$ be the control torque vector, $\boldsymbol{\omega}$ be the body angular velocity vector and $\boldsymbol{\sigma}$ be a MRP attitude coordinate vector in the following general optimal control formulation. For these developments, we consider the fixed final time problem. Adding a free final time would not change the resulting costate switching theorem and would unduly

complicate the formulation.

$$\begin{aligned} J &= h\left(t_f\right) + \int_0^{t_f} p(\boldsymbol{\sigma}, \boldsymbol{\omega}, \boldsymbol{u}, t) dt \\ s.\ t. \qquad & (\dot{\boldsymbol{\sigma}}, \dot{\boldsymbol{\omega}})^T = F(\boldsymbol{\sigma}, \boldsymbol{\omega}, \boldsymbol{u}) \end{aligned} \tag{2.96}$$

where typical scalar penalty functions are

$$h\left(t_f\right) = \frac{1}{2} K_1 g\left(\boldsymbol{\sigma}_{t_f}\right) + \frac{1}{2} \boldsymbol{\omega}_{t_f}^T [K_2] \boldsymbol{\omega}_{t_f} \tag{2.97}$$

and

$$p(\boldsymbol{\sigma},\boldsymbol{\omega},\boldsymbol{u},t) = \frac{1}{2}\left(K_3 g(\boldsymbol{\sigma}) + \boldsymbol{\omega}^T [K_4] \boldsymbol{\omega} + \boldsymbol{u}^T [R] \boldsymbol{u}\right) \tag{2.98}$$

The weights $K_1$ and $K_3$ are positive scalars and the weights $[K_2]$, $[K_4]$ and $[R]$ are positive definite 3x3 matrices. The function $g(\boldsymbol{\sigma})$ is a general, non-negative attitude penalty function. For spacecraft optimal control problems, the equations of motion can be imposed as an equality constraint. The complete equations of motion for a rigid body are rewritten below in Eqs. (2.99) and (2.100), where the function $f(\boldsymbol{\sigma})$ is defined in Eq. (2.41).

$$\dot{\boldsymbol{\sigma}} = f(\boldsymbol{\sigma}) \boldsymbol{\omega} \tag{2.99}$$

$$[I] \dot{\boldsymbol{\omega}} = -[\tilde{\omega}][I] \boldsymbol{\omega} + \boldsymbol{u} \tag{2.100}$$

The matrix $[I]$ is the spacecraft inertia matrix. The Hamiltonian $H$ for this system is

$$\begin{aligned} H = \frac{1}{2} K_3 g(\boldsymbol{\sigma}) + \frac{1}{2} \boldsymbol{\omega}^T [K_4] \boldsymbol{\omega} + \frac{1}{2} \boldsymbol{u}^T [R] \boldsymbol{u} + \boldsymbol{\Lambda}_\sigma^T f(\boldsymbol{\sigma}) \boldsymbol{\omega} \\ + \boldsymbol{\Lambda}_\omega^T [I]^{-1} (-[\tilde{\omega}][I] \boldsymbol{\omega} + \boldsymbol{u}) \end{aligned} \tag{2.101}$$

where $\boldsymbol{\Lambda}_\sigma$ is the $\boldsymbol{\sigma}$ costate vector and $\boldsymbol{\Lambda}_\omega$ is the $\boldsymbol{\omega}$ costate vector. The costate (adjoint)

differential equations are given by[36–38]

$$\dot{\mathbf{\Lambda}}_\sigma = -\frac{\partial H}{\partial \boldsymbol{\sigma}} = -\frac{1}{2}K_3\frac{\partial g}{\partial \boldsymbol{\sigma}} - \frac{\partial}{\partial \boldsymbol{\sigma}}(f(\boldsymbol{\sigma})\boldsymbol{\omega})^T\mathbf{\Lambda}_\sigma \tag{2.102}$$

$$\dot{\mathbf{\Lambda}}_\omega = -\frac{\partial H}{\partial \boldsymbol{\omega}} = -[K_4]\boldsymbol{\omega} - f(\boldsymbol{\sigma})^T\mathbf{\Lambda}_\sigma - \left([I][\tilde{\omega}] - \left[\widetilde{[I]\boldsymbol{\omega}}\right]\right)[I]^{-1}\mathbf{\Lambda}_\omega \tag{2.103}$$

For unbounded control torque $\boldsymbol{u}$, the optimality condition $\partial H/\partial \boldsymbol{u} = 0$ leads to the following optimal control torque[36–38]

$$\boldsymbol{u} = -[R]^{-1}[I]^{-1}\mathbf{\Lambda}_\omega \tag{2.104}$$

The transversality conditions for a free final state are[36,37]

$$\mathbf{\Lambda}_\sigma(t_f) = \frac{\partial h}{\partial \boldsymbol{\sigma}}(t_f) = \frac{1}{2}K_1\frac{\partial g}{\partial \boldsymbol{\sigma}}(t_f) \tag{2.105}$$

$$\mathbf{\Lambda}_\omega(t_f) = \frac{\partial h}{\partial \boldsymbol{\omega}}(t_f) = K_2\boldsymbol{\omega}(t_f) \tag{2.106}$$

The partial derivative of Eq. (2.41) with respect to $\boldsymbol{\sigma}$ is

$$\frac{\partial}{\partial \boldsymbol{\sigma}}(f(\boldsymbol{\sigma})\boldsymbol{\omega}) = \frac{1}{2}\left(\boldsymbol{\sigma}\boldsymbol{\omega}^T - [\tilde{\omega}] - \boldsymbol{\omega}\boldsymbol{\sigma}^T + \boldsymbol{\sigma}^T\boldsymbol{\omega}I\right) \tag{2.107}$$

Given good estimates of initial conditions, this nonlinear optimal control problem can be solved using various standard techniques.[38]

#### 2.3.5.2 MRP Costate Switching Condition

The optimality conditions for optimal control problem are derived assuming that all states are piece-wise smooth and continuous. Continuity is not guaranteed when switching between the two sets of MRPs. Since the "original" and "shadow" MRP satisfy exactly the same differential equation, however, the MRP costate differential equation in Eq. (2.102) is the same for either set of MRPs. To be able to switch the MRPs along the optimal trajectory, an analogous mapping of the MRP costates at

the time of the switch is required. Since the attitude penalty function *g()* renders the optimal trajectory independent of attitude coordinate choice, the MRP switching could be triggered at any time. If the *G()* function is used, then one must switch the MRPs on the $\boldsymbol{\sigma}^T\boldsymbol{\sigma} = 1$ surface, otherwise the cost function $J$ will be discontinuous.

Deriving the necessary corner conditions for discontinuous states has been covered in the literature, such as in Ref. 38. However, the state discontinuities, and therefore the variations of the state before and after a jump, are assumed to be arbitrary in this reference. With the MRPs we are in the unique situation where the discontinuity is well defined through Eq. (2.36). This results in the state variations before and after a jump being related, and leads to a different costate switching condition than what is found in the literature.

The Weierstrass-Erdmann corner conditions were developed for the case where the state derivative is discontinuous.[36,39] The same initial assumptions used in deriving the Weierstrass-Erdmann corner conditions also hold if the state, not the derivative of the state, is discontinuous. Without loss of generality, let us assume that $\boldsymbol{\sigma}$ is only discontinuous at $t_1$, where $0 < t_1 < t_f$. The time $t_1$ is chosen or specified apriori and is not part of the optimization process. Since the attitude penalty function used in this development is the universal $g()$ function which renders the optimal solution independent on the choice of attitude coordinates. Therefore we can switch arbitrarily between the original and shadow MRP attitude coordinates without affecting the final optimal trajectory. In essence, we are describing the identical optimal attitude trajectory in two different ways by using the MRPs along their shadow counterparts. This concept is illustrated in Figure 2.8. At a time $t_1$, where both the original MRP vector $\boldsymbol{\sigma}$ and the corresponding shadow set $\boldsymbol{\sigma}^S$ are defined, we chose to switch from one description to another. Since $\boldsymbol{\sigma}$ and $\boldsymbol{\sigma}^S$ are related through Eq. (2.36), any variations in $\boldsymbol{\sigma}$ at time $t_1^-$ will be therefore related to variations at time $t_1^+$.

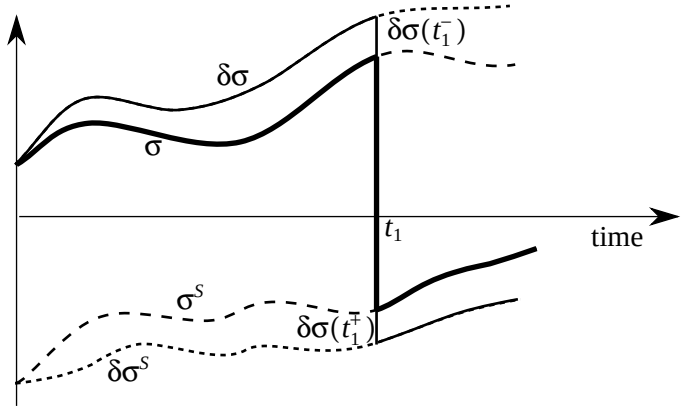


**Fig. 2.8:** Switching between MRP Descriptions While Taking Variations

The cost function $J$, in terms of the system Hamiltonian $H$ and the costates $\mathbf{\Lambda}$, can now be written as

$$J = h\left(t_f\right) + \int_0^{t_1^-} \left(H - \mathbf{\Lambda}^T \dot{\boldsymbol{x}}\right) dt + \int_{t_1^+}^{t_f} \left(H - \mathbf{\Lambda}^T \dot{\boldsymbol{x}}\right) dt = J_1 + J_2 + J_3 \tag{2.108}$$

where $\boldsymbol{x} = col(\boldsymbol{\sigma}, \boldsymbol{\omega})$ and $\mathbf{\Lambda} = col(\mathbf{\Lambda}_\sigma, \mathbf{\Lambda}_\omega)$. For notational compactness, lets define $\boldsymbol{\sigma}_- = \boldsymbol{\sigma}(t_1^-)$, $\boldsymbol{\sigma}_+ = \boldsymbol{\sigma}(t_1^+)$, $\mathbf{\Lambda}_{i^-} = \mathbf{\Lambda}_i(t_1^-)$ and $\mathbf{\Lambda}_{i^+} = \mathbf{\Lambda}_i(t_1^+)$. Each integral can now be evaluated without state discontinuity problems. The first variation of $J$ must satisfy[36]

$$\delta J = 0 = \delta J_1 + \delta J_2 + \delta J_3 \tag{2.109}$$

The first variation of $J_1$ is

$$\delta J_1 = \frac{\partial h}{\partial \boldsymbol{x}}(\boldsymbol{x}\left(t_f\right))^T \delta \boldsymbol{x}(t_f) \tag{2.110}$$

Taking the first variation of $J_2$, we treat $t_1$ as a fixed time.

$$\delta J_2 = \int_0^{t_1^-} \left(\frac{\partial H}{\partial \boldsymbol{x}}^T \delta \boldsymbol{x} - \mathbf{\Lambda}^T \delta \dot{\boldsymbol{x}} + \frac{\partial H}{\partial \boldsymbol{u}}^T \delta \boldsymbol{u}\right) dt \tag{2.111}$$

Since the states are smooth and continuous within the integral, $\delta \dot{\boldsymbol{x}}$ can be written as

$\frac{d}{dt}(\delta \boldsymbol{x})$. This permits $\delta J_2$ to be integrated by parts.

$$\delta J_2 = -\boldsymbol{\Lambda}(t_1^-)^T \delta \boldsymbol{x}(t_1^-) + \int_0^{t_1^-} \left( \left( \frac{\partial H}{\partial \boldsymbol{x}} + \dot{\boldsymbol{\Lambda}} \right)^T \delta \boldsymbol{x} + \frac{\partial H}{\partial \boldsymbol{u}}^T \delta \boldsymbol{u} \right) dt \tag{2.112}$$

Let $\delta \boldsymbol{x}(t_1^-) = (\delta \boldsymbol{\sigma}_-, \delta \boldsymbol{\omega}_-)^T$, then $\delta J_2$ is written as

$$\delta J_2 = -\boldsymbol{\Lambda}_{\sigma^-}^T \delta \boldsymbol{\sigma}_- - \boldsymbol{\Lambda}_{\omega^-}^T \delta \boldsymbol{\omega}_- + \int_0^{t_1^-} \left( \left( \frac{\partial H}{\partial \boldsymbol{x}} + \dot{\boldsymbol{\Lambda}} \right)^T \delta \boldsymbol{x} + \frac{\partial H}{\partial \boldsymbol{u}}^T \delta \boldsymbol{u} \right) dt \tag{2.113}$$

Similarly $\delta J_3$ can be found assuming that the initial and final states on the interval $(t_1^+, t_f)$ are free and the time $t_1$ is fixed.

$$\begin{aligned} \delta J_3 = \boldsymbol{\Lambda}_{\sigma^+}^T \delta \boldsymbol{\sigma}_+ + \boldsymbol{\Lambda}_{\omega^+}^T \delta \boldsymbol{\omega}_+ - \boldsymbol{\Lambda}(t_f)^T \delta \boldsymbol{x}_f \\ + \int_{t_1^+}^{t_f} \left( \left( \frac{\partial H}{\partial \boldsymbol{x}} + \dot{\boldsymbol{\Lambda}} \right)^T \delta \boldsymbol{x} + \frac{\partial H}{\partial \boldsymbol{u}}^T \delta \boldsymbol{u} \right) dt \end{aligned} \tag{2.114}$$

Since the body angular velocity is continuous $\delta \boldsymbol{\omega}_- = \delta \boldsymbol{\omega}_+ = \delta \boldsymbol{\omega}$. After enforcing the optimality and transversality conditions, the total variation $\delta J$ becomes[38]

$$\delta J = \boldsymbol{\Lambda}_{\sigma^+}^T \delta \boldsymbol{\sigma}_+ - \boldsymbol{\Lambda}_{\sigma^-}^T \delta \boldsymbol{\sigma}_- + (\boldsymbol{\Lambda}_{\omega^+} - \boldsymbol{\Lambda}_{\omega^-})^T \delta \boldsymbol{\omega} = 0 \tag{2.115}$$

Since the variation $\delta \boldsymbol{\omega}_1$ in Eq. (2.115) is independent from other variations, the following conclusion can be made.

$$\boldsymbol{\Lambda}_{\omega^+} = \boldsymbol{\Lambda}_{\omega^-} \tag{2.116}$$

Since a switch occurs at $t_1$, $\boldsymbol{\sigma}_+$ would be the "shadow" set of $\boldsymbol{\sigma}_-$. Recall that which set is referred to as the "original" or as the "shadow" set is arbitrary. This mapping from $\boldsymbol{\sigma}_-$ to $\boldsymbol{\sigma}_+$ is well defined in Eq. (2.36), therefore the variations $\delta \boldsymbol{\sigma}_-$ and $\delta \boldsymbol{\sigma}_+$ are also related. Their relative mapping is found by taking the first variation of Eq. (2.36).

$$\delta \boldsymbol{\sigma}_- = {\boldsymbol{\sigma}_+}^{-4} \left[ 2\boldsymbol{\sigma}_+ \boldsymbol{\sigma}_+^T - \boldsymbol{\sigma}_+^T \boldsymbol{\sigma}_+ I \right] \delta \boldsymbol{\sigma}_+ \tag{2.117}$$

which can be further reduced to the following useful form using Eq. (2.36).

$$\delta\boldsymbol{\sigma}_- = \left[2\boldsymbol{\sigma}_-\boldsymbol{\sigma}_-^T - \boldsymbol{\sigma}_-^T\boldsymbol{\sigma}_- I\right]\delta\boldsymbol{\sigma}_+ \tag{2.118}$$

Since the total variation $\delta J$ given in Eq. (2.115) must be zero, then

$$\boldsymbol{\Lambda}_{\sigma^+}^T\delta\boldsymbol{\sigma}_+ = \boldsymbol{\Lambda}_{\sigma^-}^T\delta\boldsymbol{\sigma}_- \tag{2.119}$$

must be true. After expanding this condition using Eq. (2.118) we obtain

$$\left(\boldsymbol{\Lambda}_{\sigma^+} - \left[2\boldsymbol{\sigma}_-\boldsymbol{\sigma}_-{}^T - \boldsymbol{\sigma}_-{}^T\boldsymbol{\sigma}_- I\right]\boldsymbol{\Lambda}_{\sigma^-}\right)^T\delta\boldsymbol{\sigma}_+ = 0 \tag{2.120}$$

Since Eq. (2.120) must hold for any admissible variations $\delta\boldsymbol{\sigma}_+$ the following costate switching condition is found:

$$\boldsymbol{\Lambda}_{\sigma^+} = \left[2\boldsymbol{\sigma}_-\boldsymbol{\sigma}_-^T - \left(\boldsymbol{\sigma}_-^T\boldsymbol{\sigma}_-\right) I\right]\boldsymbol{\Lambda}_{\sigma^-} \tag{2.121}$$

Note that Eq. (2.121) yields a general mapping for the switching of a costate $\boldsymbol{\Lambda}_{\sigma^-}$ to its "shadow" costate $\boldsymbol{\Lambda}_{\sigma^+}$. This mapping is valid at any instance of the maneuver.

Let us examine the special case of performing pure single-axis rotations. Using Eq. (2.36) the attitude vector can be written as $\boldsymbol{\sigma} = \hat{\boldsymbol{e}}|\boldsymbol{\sigma}| = \hat{\boldsymbol{e}}\sigma$. The body angular velocity vector is given by $\boldsymbol{\omega} = \hat{\boldsymbol{e}}|\boldsymbol{\omega}| = \hat{\boldsymbol{e}}\omega$. From Eqs. (2.102), (2.105) and (2.107) it is clear that for a single axis rotation the attitude costate $\boldsymbol{\Lambda}_\sigma$ can be written as $\boldsymbol{\Lambda}_\sigma = \hat{\boldsymbol{e}}|\boldsymbol{\Lambda}_\sigma| = \hat{\boldsymbol{e}}\Lambda_\sigma$. Using these definitions, the following costate switching condition can be found for the single-axis rotation case.

$$\Lambda_{\sigma^+} = \left(\boldsymbol{\sigma}_-^T\boldsymbol{\sigma}_-\right)\Lambda_{\sigma^-} \tag{2.122}$$

The above condition shows that the only instance for which $\boldsymbol{\Lambda}_\sigma$ does not have a discontinuity during the switching is the case of a single-axis rotation with the switching surface $\boldsymbol{\sigma}^T\boldsymbol{\sigma} = 1$. The developments above lead to the following theorem:

**Theorem 2.2 (MRP Costate Switching Condition)** *Assume that the scalar attitude penalty function be given by Eq.* (2.92)*, then the costate* $\mathbf{\Lambda}_\omega$ *and the Hamiltonian* $H$ *will remain continuous during the switching of the MRPs to their "shadow" set. The costate* $\mathbf{\Lambda}_\sigma$*,however, will have a discontinuity defined by Eq. (2.121).*

To verify that the Hamiltonian $H$ remains continuous during the switching of the MRPs, Eq. (2.101) is studied. The attitude penalty function $g()$ is continuous during the switching, as are the control vector $\boldsymbol{u}$ and the angular velocity vector $\boldsymbol{\omega}$. The only term that needs to be shown to remain continuous during the MRP switching is $\mathbf{\Lambda}_\sigma^T f(\boldsymbol{\sigma})\boldsymbol{\omega}$. Using Eq. (2.121) we get

$$\mathbf{\Lambda}_{\sigma^-}^T f(\boldsymbol{\sigma}_-)\boldsymbol{\omega} - \mathbf{\Lambda}_{\sigma^+}^T f(\boldsymbol{\sigma}_+)\boldsymbol{\omega} = \mathbf{\Lambda}_{\sigma^-}^T \left(f(\boldsymbol{\sigma}_-) - (2\boldsymbol{\sigma}_-\boldsymbol{\sigma}_-^T - \boldsymbol{\sigma}_-^T\boldsymbol{\sigma}_- I) f(\boldsymbol{\sigma}_+)\right)\boldsymbol{\omega} \quad (2.123)$$

After using Eq. (2.42) this expression is rewritten as

$$\mathbf{\Lambda}_{\sigma^-}^T \left(\dot{\boldsymbol{\sigma}}_- - (2\boldsymbol{\sigma}_-\boldsymbol{\sigma}_-^T - \boldsymbol{\sigma}_-^T\boldsymbol{\sigma}_- I)\left(-\frac{\dot{\boldsymbol{\sigma}}_-}{\sigma_-^2} + \frac{1}{2}\left(\frac{1+\sigma_-^2}{\sigma_-^4}\right)\boldsymbol{\sigma}_-\boldsymbol{\sigma}_-^T\right)\right)\boldsymbol{\omega} \quad (2.124)$$

After substituting the differential kinematic equation for the MRPs given in Eq. (2.41) it can be verified that

$$\mathbf{\Lambda}_{\sigma^-}^T f(\boldsymbol{\sigma}_-)\boldsymbol{\omega} - \mathbf{\Lambda}_{\sigma^+}^T f(\boldsymbol{\sigma}_+)\boldsymbol{\omega} = 0 \quad (2.125)$$

and that the Hamiltonian $H$ will remain continuous during the MRP switching. Note that Theorem 2.2 allows for the MRPs to switch on *any* time where $\boldsymbol{\sigma}^T\boldsymbol{\sigma} > c^2$. A numerical method would not have to pin point the time where this surface is penetrated. It is sufficient to monitor at each time step if a surface penetration has occurred, meaning that $\boldsymbol{\sigma}^T\boldsymbol{\sigma} > c^2$. If yes, then the attitude state and costate would be switched as shown. This theorem leads directly to the following corollary regarding the costate magnitude $|\mathbf{\Lambda}_\sigma|$ during the MRP switching.

**Corollary 2.1** *The costate magnitude* $|\mathbf{\Lambda}_\sigma|$ *will remain continuous during the MRP switching if the* $\boldsymbol{\sigma}^T\boldsymbol{\sigma} = 1$ *switching surface is used.*

**Proof:** Corollary 2.1 is verified by using Theorem 2.2 to find the expression $\mathbf{\Lambda}_\sigma^T\mathbf{\Lambda}_\sigma$ before and after the MRP switching, and using the fact that during the switching $\boldsymbol{\sigma}^T\boldsymbol{\sigma}$ is equal to 1. ■

This corollary shows that the MRP costate vector $\mathbf{\Lambda}_\sigma$ behaves very similar to the MRP vector $\boldsymbol{\sigma}$ during the switching. Both switch on the surface of a sphere. The difference is that $\boldsymbol{\sigma}$ switches on a unit sphere, where $\mathbf{\Lambda}_\sigma$ switches on a sphere of arbitrary radius.

Instead of using the calculus of variations development, the MRP costate switching conditions can also be derived by transforming the given optimal control problem with internal discontinuous states into a standard optimal control problem with a terminal constraint surface. This is accomplished by doubling the number of system states by assigning the states before and after the switch at $t_1$ to be separate, independent states. The states before the switch are integrated forward in time on the interval $[0, t_1]$, where the states after the switch are integrated backward in time on $[t_f, t_1]$. By folding the time around the state discontinuity, the previously internal MRP switching at $t_1$ now effectively becomes a terminal state constraint.[40] The MRP costate switching conditions are then found by using the standard necessary conditions for a continuous optimal control problem with the terminal state constraint surfaces[38] $\boldsymbol{\sigma}^S(t_1^+) + \boldsymbol{\sigma}(t_1^-)/\sigma^2(t_1^-) = 0$ and $\boldsymbol{\omega}(t_1^+) - \boldsymbol{\omega}(t_1^-) = 0$.

#### 2.3.5.3 Analytical Result of a Single-Axis Rotation

To verify the MRP costate switching conditions, a simple single-axis optimal control problem is solved analytically using the MRPs as attitude parameters. For generality,

the switching surface is set to $\sigma^2 = c^2$. Let us minimize the cost function $J$ which depends solely on the control $u$

$$J = \frac{1}{2}\int_0^1 u^2 dt \tag{2.126}$$

subject to the simple one-dimensional equations of motion for a body with unit inertia

$$\dot{\sigma} = \frac{1}{4}\left(1+\sigma^2\right)\omega \tag{2.127}$$

$$\dot{\omega} = u \tag{2.128}$$

and subject to the state constraints

$$\sigma(t_0 = 0) = \sigma_0 \qquad \sigma(t_f = 1) = \sigma_f \qquad \omega(t_0) = \omega(t_f) = 0 \tag{2.129}$$

The optimal control torque $u^*$ for this cost function $J$ is known to be of the form[5]

$$u^*(t) = k(1-2t) \tag{2.130}$$

where $k$ is simply a scaling factor that guarantees that the body is at $\sigma_f$ at $t_f$. Note that the optimal trajectory is independent of the choice of attitude coordinates. This allows the optimal control problem to be solved using either the "original" MRP set or their "shadow" set. By comparing the resulting costate $\Lambda_\sigma$ history for the "original" and "shadow" costates, we verify below the costate switching condition for single-axis rotations in Eq. (2.122). The optimality condition in Eq. (2.104) states that

$$u^*(t) = -\Lambda_\omega(t) \tag{2.131}$$

Since $u^*$ is continuous, so is $\Lambda_\omega$ as predicted in Eq. (2.116). If at some point in time the MRP are switched to their "shadow" set it obviously has no effect on the continuity of $\Lambda_\omega$.

To find a time history of the costate $\Lambda_\sigma$, Eq. (2.103) is used.

$$\dot{\Lambda}_\omega = -\frac{1}{4}\left(1+\sigma^2\right)\Lambda_\sigma \tag{2.132}$$

Since $\dot{\Lambda}_\omega = 2k$ this can be solved for $\Lambda_\sigma$.

$$\Lambda_\sigma = -\frac{8k}{1+\sigma^2} \tag{2.133}$$

Let $\sigma^S$ and $\Lambda_\sigma^S$ be the "shadow" attitude and costate vector. Analogous to above, the solution for $\Lambda_\sigma^S$ is

$$\Lambda_\sigma^S = -\frac{8k}{1+\left(\sigma^S\right)^2} \tag{2.134}$$

Eq. (2.134) can be written in terms of $\sigma$ by using Eq. (2.36).

$$\Lambda_\sigma^S = -\frac{8k}{1+\frac{1}{\sigma^2}} = -\frac{8k}{1+\sigma^2}\sigma^2 \tag{2.135}$$

Substituting Eq. (2.133) into Eq. (2.135) a direct relationship between $\Lambda_\sigma^S$ and $\Lambda_\sigma$ is obtained.

$$\Lambda_\sigma^S = \sigma^2\Lambda_\sigma \tag{2.136}$$

By switching between the two possible MRP attitude descriptions the costate $\Lambda_\sigma$ must be switched as well according to Eq. (2.136). This result verifies the single-axis rotation MRP costate switching condition found in Eq. (2.122).

#### 2.3.5.4 Three-Dimensional Numerical Result

To verify the general transformation given in the MRP costate switching condition theorem, a three-dimensional optimal control problem was solved as outlined in the problem statement. The attitude penalty function was chosen to be the *g()* given in Eq. (2.91). With this penalty function the answer did not depend on the attitude

coordinate choice. Therefore the optimal solution using the combined set of $\boldsymbol{\sigma}$ and $\boldsymbol{\sigma}^S$ should be the same as the optimal solution obtained by using only $\boldsymbol{\sigma}$ or $\boldsymbol{\sigma}^S$.

The optimization problem was solved numerically by a steepest descent method.[38] The only modification needed to use the combined set of original and shadow MRP vectors was to check whether $\boldsymbol{\sigma}^T\boldsymbol{\sigma}$ had grown larger than one. If yes, then the attitude vector was switched to its shadow counter part. At the same time the corresponding attitude costate vector was also switched to its shadow counter part using the MRP costate switching condition.

**Table 2.3:** Parameters of 3D Optimal Control Problem

| Parameter | Value | Units |
|---|---|---|
| $I_1$ | 0.5 | kg-m$^2$/sec |
| $I_2$ | 1.0 | kg-m$^2$/sec |
| $I_3$ | 0.7 | kg-m$^2$/sec |
| $K_1$ | 2 | |
| $K_2$ | 10 | |
| $K_3$ | 1 | |
| $K_4$ | 5 | |
| $R$ | 20 | |
| $\boldsymbol{\sigma}(t_0)$ | [0.87 0.00 0.00] | |
| $\boldsymbol{\omega}(t_0)$ | [80.21 51.57 45.84] | deg/sec |

The three-dimensional optimal control problem had a fixed maneuver time $t_f$ of 10 seconds. The body axis are assumed to be aligned with the principal axis. The values of the simulation parameters are shown in Table 2.3. Note that the initial orientation has the body almost turned up-side-down with a large initial angular velocity driving it to the up-side-down orientation. This optimal control problem penalizes any non-zero state and torque during the maneuver and any non-zero final state. Note that the final state is left free. Trying to minimize torque for this maneuver, it is intuitively reasonable to let the body rotate through the up-side-down orientation and then reduce the states instead of forcefully reversing the existing motion.

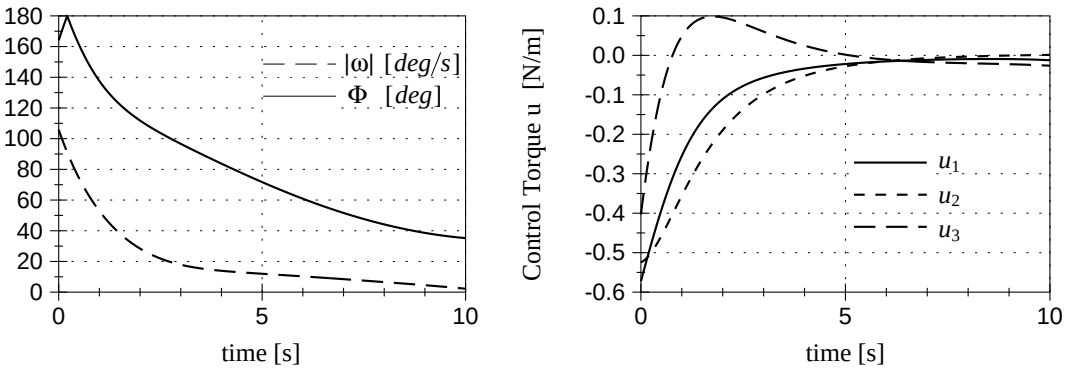


(i) Optimal $\boldsymbol{\omega}$ and $\Phi$ (ii) Optimal Control Torque $\boldsymbol{u}$

**Fig. 2.9:** Optimal Results for All Three Cases

Three separate optimal control problems were solved using either $\boldsymbol{\sigma}/\boldsymbol{\sigma}^S$, $\boldsymbol{\sigma}$ or $\boldsymbol{\sigma}^S$ as the attitude coordinates. As expected, all three optimizations converged to the same solution. The principal rotation angle $\phi$ and the magnitude of the angular velocity are shown in Figure 2.9(i). The optimal solution indeed lets the body rotate through the $\Phi = 180$ degree point and diminishes simultaneously the angular velocity and attitude errors as the final maneuver time is approached. The optimal control torque for the maneuver is shown in Figure 2.9(ii). The attitude coordinate vector time histories are shown in Figure 2.10(i). The respective MRP trajectories were different for each case since different attitude coordinates were used. The combined set $\boldsymbol{\sigma}/\boldsymbol{\sigma}^S$ started out identical to $\boldsymbol{\sigma}$, since the initial attitude vector had less than unit magnitude. As $|\boldsymbol{\sigma}|$ grew larger than one, the combined set $\boldsymbol{\sigma}/\boldsymbol{\sigma}^S$ trajectory is switched to the shadow set $\boldsymbol{\sigma}^S$ trajectory. This is illustrated in Figure 2.10(i). The black line denotes the trajectory of the combined $\boldsymbol{\sigma}$ and $\boldsymbol{\sigma}^S$ set which remains within the unit sphere. Note that this trajectory converged exactly with the $\boldsymbol{\sigma}$ and $\boldsymbol{\sigma}^S$ trajectories whenever they too were within the unit sphere.

The ultimate test of the MRP costate switching condition theorem is to see

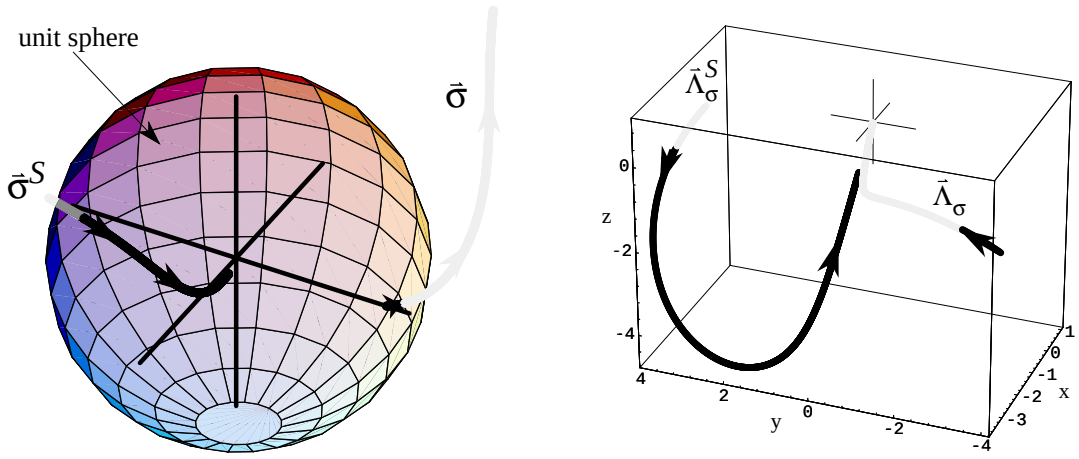


(i) MRP Attitude Coordinates (ii) MRP Costate Coordinates

**Fig. 2.10:** Three-Dimensional Illustration of $\boldsymbol{\sigma}$ and $\boldsymbol{\Lambda}_\sigma$ for All Three Cases

if the costate $\boldsymbol{\Lambda}_\sigma$ exhibits the same behavior. The costate trajectories are shown in Figure 2.10(ii). Again the black line is the solution obtained using the combined $\boldsymbol{\sigma}/\boldsymbol{\sigma}^S$ set and using the MRP costate switching condition. Indeed the costate $\boldsymbol{\Lambda}_\sigma$ switches exactly from the costate trajectory of the pure $\boldsymbol{\sigma}$ solution to the costate trajectory of the pure $\boldsymbol{\sigma}^S$ solution, thus verifying the MRP Costate Switching theorem presented in this section.

## 2.4 Asymmetric Stereographic Orientation Parameters

Both the classical and the modified Rodrigues parameters are examples of symmetric stereographic parameters. Their singular orientation depends solely on the corresponding principal rotation angle $\Phi$ and the range of allowable orientations up to the singularity is symmetric about the zero rotation. In this section, an example asymmetric stereographic parameter vector $\boldsymbol{\eta}$ is constructed. The Euler parameter $\beta_1$ is eliminated and setting the projection point $a = -1$ on the $\beta_1$ axis as shown

in Figure 2.2. The corresponding projection hyperplane is defined through $\beta_1 = 0$. Adjusting Eq. (2.5), the vector $\boldsymbol{\eta}$ is defined as

$$\boldsymbol{\eta} = \frac{1}{\beta_1 + 1} \begin{pmatrix} \beta_0 \\ \beta_2 \\ \beta_3 \end{pmatrix} \tag{2.137}$$

The singularity condition in Eq. (2.14) is for this set of parameters

$$e_1 \sin \frac{\Phi}{2} = -1 \tag{2.138}$$

Since the sine function is bounded by $\pm 1$, a singular orientation is *only possible* if the corresponding principal rotation axis $\hat{\boldsymbol{e}}$ is along the first body axis. If $\hat{\boldsymbol{e}}$ is *never* along $\hat{\boldsymbol{b}}_1$, then the $\boldsymbol{\eta}$ parameters will *never* encounter any singular orientations. Therefore, contrary to the symmetric SP such as the classical and modified Rodrigues parameters, the asymmetric SP vector $\boldsymbol{\eta}$ is able to describe the orientation of a rotating body without having to resort to switching the attitude parameters to alternate shadow sets.

Using Eqs. (2.12) and (2.13) the singular principal rotation angles for the $\boldsymbol{\eta}$ attitude vector becomes $\Phi_{s_1}$ = -180 degrees and $\Phi_{s_2}$ =+540 degrees about the first body axis. As mentioned earlier, the direction at which a singular orientation is approached is important with asymmetric stereographic parameters. Here a negative principal rotation of 180 degrees about the first body axis causes a singularity. A positive principal rotation of 180 degrees would yield an identical physical orientation, yet no singularity is encountered! Only after a +540 rotation about $\hat{\boldsymbol{b}}_1$ does this representation go singular, even though this position is the same as +180 degrees. This strange non-symmetric principal angle range is due to the fact that the zero rotation point (1,0,0,0) does not lie on the $\beta_1$ axis. Naturally, as with the symmetric SPs, any

singularities could always be avoided by switching the $\boldsymbol{\eta}$ vector to its corresponding shadow set through

$$\boldsymbol{\eta}^S = -\frac{1}{\boldsymbol{\eta}^T\boldsymbol{\eta}}\boldsymbol{\eta} \tag{2.139}$$

Differentiating Eq. (2.137) and using Eq. (2.11), the differential kinematic equation for the $\boldsymbol{\eta}$ vector is found to be

$$\dot{\boldsymbol{\eta}} = \tfrac{1}{4}\begin{bmatrix} (-1-\eta_1^2+\eta_2^2+\eta_3^2) & 2(\eta_1\eta_3-\eta_2) & \\ 2(\eta_3-\eta_1\eta_2) & 2(\eta_2\eta_3+\eta-1) & \cdots \\ -2(\eta_1\eta_3+\eta_2) & (1-\eta_1^2-\eta_2^2+\eta_3^2) & \\ & -2(\eta_1\eta_2+\eta_3) & \\ \cdots & (-1+\eta_1^2-\eta_2^2+\eta_3^2) & \\ & 2(\eta_1-\eta_2\eta_3) & \end{bmatrix}\begin{bmatrix}\omega_1\\ \omega_2\\ \omega_3\end{bmatrix} \tag{2.140}$$

Note that Eq. (2.140) contains no transcendental functions and is similar qualitatively to Eq. (2.40). Because $\boldsymbol{\eta}$ is an asymmetric stereographic parameter vector, there is less evident symmetry in the matrix. As a result, Eq. (2.140) cannot be written in a more compact vector form as was the case with the symmetric stereographic parameters. The direction cosine matrix in terms of the $\boldsymbol{\eta}$ components is given by

$$[C] = \tfrac{1}{(1+\eta^2)^2}\begin{bmatrix} 4(\eta_1^2-\eta_2^2-\eta_3^2)+\Sigma^2 & 8\eta_1\eta_3+4\eta_1\Sigma & \\ -8\eta_1\eta_3+4\eta_2\Sigma & 4(\eta_1^2+\eta_2^2-\eta_3^2)+\Sigma^2 & \cdots \\ 8\eta_1\eta_2+4\eta_3\Sigma & 8\eta_2\eta_3-4\eta_1\Sigma & \\ & -8\eta_1\eta_2+4\eta_3\Sigma & \\ \cdots & 8\eta_2\eta_3+4\eta_1\Sigma & \\ & 4(\eta_1^2-\eta_2^2+\eta_3^2)+\Sigma^2 & \end{bmatrix} \tag{2.141}$$

Analogously, asymmetric stereographic parameters could be derived by projecting onto a hyperplane orthogonal to the $\beta_2$ or $\beta_3$ axis, or actually any non-$\beta_0$ axis.

All these parameters would have a similar singular behavior as the $\boldsymbol{\eta}$ parameters presented in the section. In practice the body axis is chosen about which the rigid body is least likely to rotate. Then the corresponding $\beta_i$ parameter is eliminated through the appropriate stereographic projection. The resulting three parameter set will then only encounter a singularity when the rigid body is at the two specific orientations discussed earlier.

# CHAPTER III

## EIGENFACTOR QUASI-VELOCITY COORDINATES *

While the previous chapter dealt with studying novel sets of attitude coordinates, this chapter studies a new set of quasivelocity coordinates called the Eigenfactor Quasivelocities (EQVs). Also, while the earlier discussion pertained to a single rigid body, a system of bodies is considered in this chapter. Large nonlinear motions are admitted. The equations of motion of complex dynamical systems are usually second order nonlinear differential equations which, in the most general case, require taking the inverse of a time-varying, configuration variable dependent mass matrix in some manner. Such dynamical systems could be a large nonlinear deformation model for an arbitrary body, a multi-body system, or a multi-link robot arm. One reason why the resulting dynamics are complicated is that they are usually written in a way that combines coordinates natural to the momentum or energy description with configuration coordinates natural to the displacement description. The result is a split between momentum differential equations and kinematic differential equations. This natural splitting is typically destroyed when the generalized methods of mechanics are employed and result in a more complicated mass matrix. This occurs when the classical Lagrange equations of motion are written in terms of a generalized coordinate and their time derivatives. By using Newton-Eulerian mechanics or modified Lagrange's equations of motion, it is possible to introduce quasivelocities which separate the decision of choosing displacement coordinates and velocity (momentum) coordinates. As is well-known, (e.g. Eulerian rigid body dynamics), this process often leads to more attractive sets of equations than those that result from "brute force" application of

*Portions of this chapter were published in References 41–43. Authors retained the copyright.

Lagrange's equations. It is possible to bring the equations of motion to their most convenient form with a constant mass matrix.[11,44] For general configuration-variable mass matrices there has not been a generally applicable method to accomplish an analogous transformation.

Several methods have been proposed to carry out the mass matrix inverse[11,45] ranging from taking an algebraic inverse, to using traditional numerical inverse methods (such as a Cholesky decomposition), to an elegant recursive method of using the innovations factorization.[11] Naturally each method has its advantages and disadvantages. The algebraic inverse is only feasible for relatively small systems; even when making use of symbol manipulation programs such as Mathematica and Maple. Taking a numerical inverse at each integration step is computationally costly and difficult, but is also the most generally applicable method. The method proposed by Ref. 11 uses the innovations factorizations technique to parameterize the mass matrix and recursively approximate its inverse. The mass matrix factors involved are obtained from a recursive filter. However, this recursive filter is conveniently applicable only to a linked body chain and other kinematically recursive topologies.

This chapter presents a method to solve a very general class of constrained and unconstrained dynamical systems and avoids the necessity of inverting a configuration variable mass matrix to obtain instantaneous accelerations. The equations of motion will be separated into dynamical and kinematic differential equations somewhat analogous to classical developments in rigid body dynamics. A method outlined in Ref. 41 will be used to replace the mass matrix inverse problem with one of solving the corresponding eigenfactor differential equations. The new formulation will also allow any Pfaffian constraints to be easily incorporated into the equations of motion, thus avoiding having coupled algebraic constraint equations to be solved simultaneously with the original equations of motion and reducing the overall order of the system.

### 3.1 Classical Lagrange Equations of Motion

The equations of motion for a dynamical system can be derived by first formulating expressions for the kinetic energy $T$ and the potential energy $V$. Let the system Lagrangian $\mathcal{L}$ be defined as

$$\mathcal{L} = T - V \tag{3.1}$$

Let $\boldsymbol{x}$ be the generalized configuration coordinate vector for the system, then the potential energy is given by

$$V = V(\boldsymbol{x}) \tag{3.2}$$

The kinetic energy can be written in terms of the state vector derivative $\dot{\boldsymbol{x}}$ or in terms of a quasivelocity vector $\boldsymbol{y}$ defined as

$$\boldsymbol{y} = [R(\boldsymbol{x})]\dot{\boldsymbol{x}} \tag{3.3}$$

where the matrix $[R(\boldsymbol{x})]$ linearly relates $\dot{\boldsymbol{x}}$ to $\boldsymbol{y}$. A field where quasivelocities are often preferred over configuration coordinate derivatives is rigid body attitude dynamics. For example, it is much simpler to write the system kinetic energy in terms of the body angular velocity $\boldsymbol{\omega}$ than in terms of the Euler attitude angle derivatives $\dot{\boldsymbol{\theta}}$. Let $[\bar{M}(\boldsymbol{x}, t)]$ be the mass matrix for a system described with $\boldsymbol{y}$, then the total kinetic energy for the system is given by

$$T = T_2 + T_1 + T_0 = \frac{1}{2}\boldsymbol{y}^T[\bar{M}(\boldsymbol{x}, t)]\boldsymbol{y} + \bar{\boldsymbol{G}}^T(\boldsymbol{x}, t)\boldsymbol{y} + T_0(\boldsymbol{x}, t) \tag{3.4}$$

where the $T_1 = \bar{\boldsymbol{G}}^T\boldsymbol{y}$ and $T_0$ terms only appear in unnatural systems. However, to find the traditional version of Lagrange's equations of motion, the kinetic energy needs to be written in terms of generalized coordinate derivative $\dot{\boldsymbol{x}}$, not in terms of

quasivelocities $\boldsymbol{y}$. Using Eq. (3.3), the kinetic energy is thus rewritten in terms of $\dot{\boldsymbol{x}}$ as

$$T_2 = \frac{1}{2}\dot{\boldsymbol{x}}^T[R(\boldsymbol{x})]^T[\bar{M}(\boldsymbol{x},t)][R(\boldsymbol{x})]\dot{\boldsymbol{x}} = \frac{1}{2}\dot{\boldsymbol{x}}^T[M(\boldsymbol{x},t)]\dot{\boldsymbol{x}} \tag{3.5}$$

$$T_1 = \bar{\boldsymbol{G}}^T(\boldsymbol{x},t)[R(\boldsymbol{x})]\dot{\boldsymbol{x}} = \boldsymbol{G}^T(\boldsymbol{x},t)\dot{\boldsymbol{x}} \tag{3.6}$$

where $[M(\boldsymbol{x},t)] = [R(\boldsymbol{x})]^T[\bar{M}(\boldsymbol{x},t)][R(\boldsymbol{x})]$ is the system mass matrix for the state vector $(\boldsymbol{x},\dot{\boldsymbol{x}})$ and $\boldsymbol{G}(\boldsymbol{x},t) = [R(\boldsymbol{x})]^T\bar{\boldsymbol{G}}(\boldsymbol{x},t)$. For mechanical systems $[M(\boldsymbol{x},t)]$ will always be symmetric positive definite. Let $\boldsymbol{Q}$ be a non-conservative force and let $-[A]^T\boldsymbol{\lambda}$ be the constraint force, then the Lagrange equations of motion are defined as

$$\frac{d}{dt}\left(\frac{\partial\mathcal{L}}{\partial\dot{\boldsymbol{x}}}\right) - \frac{\partial\mathcal{L}}{\partial\boldsymbol{x}} = \boldsymbol{Q} - [A]^T\boldsymbol{\lambda} \tag{3.7}$$

with the Pfaffian non-holonomic constraint system having the structure[46]

$$[A(\boldsymbol{x})]\dot{\boldsymbol{x}} + \boldsymbol{b}(t) = 0 \tag{3.8}$$

If $m$ Pfaffian non-holonomic constraints are present and the state vector $\boldsymbol{x}$ is of dimension $n$, then $[A]$ is a $m$x$n$ matrix. The needed partial derivatives of the system Lagrangian $\mathcal{L}$ are

$$\frac{\partial\mathcal{L}}{\partial\dot{\boldsymbol{x}}} = [M(\boldsymbol{x},t)]\dot{\boldsymbol{x}} + \boldsymbol{G}(\boldsymbol{x},t) \tag{3.9}$$

and

$$\frac{\partial\mathcal{L}}{\partial\boldsymbol{x}} = \frac{1}{2}\dot{\boldsymbol{x}}^T\frac{\partial[M(\boldsymbol{x},t)]}{\partial\boldsymbol{x}}\dot{\boldsymbol{x}} + \frac{\partial\boldsymbol{G}^T(\boldsymbol{x},t)}{\partial\boldsymbol{x}}\dot{\boldsymbol{x}} + \frac{\partial T_0(\boldsymbol{x},t)}{\partial\boldsymbol{x}} - \frac{\partial V}{\partial\boldsymbol{x}} \tag{3.10}$$

where the term $\dot{\boldsymbol{x}}^T \frac{\partial[M(\boldsymbol{x},t)]}{\partial \boldsymbol{x}} \dot{\boldsymbol{x}}$ is a column vector. The resulting standard Lagrange equations of motion are

$$[M(\boldsymbol{x},t)]\ddot{\boldsymbol{x}} + \left( [\dot{M}] - \frac{1}{2}\dot{\boldsymbol{x}}^T \frac{\partial[M(\boldsymbol{x},t)]}{\partial \boldsymbol{x}} - \frac{\partial G^T(\boldsymbol{x},t)}{\partial \boldsymbol{x}} \right) \dot{\boldsymbol{x}} + \dot{\boldsymbol{G}}(\boldsymbol{x},t) - \frac{\partial T_0(\boldsymbol{x},t)}{\partial \boldsymbol{x}} + \frac{\partial V}{\partial \boldsymbol{x}} = \boldsymbol{Q} - [A]^T \boldsymbol{\lambda} \quad (3.11)$$

or more compactly

$$[M(\boldsymbol{x},t)]\ddot{\boldsymbol{x}} + \Xi(\boldsymbol{x},\dot{\boldsymbol{x}},t) + \frac{\partial V}{\partial \boldsymbol{x}} = \boldsymbol{Q} - [A]^T \boldsymbol{\lambda} \quad (3.12)$$

The above equations of motion are a second order nonlinear differential equation, obviously generally not a simple task to solve. In particular, the time and state dependence of the mass matrix poses a potential difficulty. These standard equations of motion, when coupled to the constraint equations in Eq. (3.8), pose a significant challenge for high dimensioned systems. The necessity of solving systems of order $n+m$ to obtain $(\ddot{\boldsymbol{x}}, \boldsymbol{\lambda})$ for each $(\boldsymbol{x},\dot{\boldsymbol{x}},t)$ lies at the heart of the difficulty.

## 3.2 Eigenfactor Quasivelocity Equations of Motion

The following development is motived by studying rigid body dynamics wherein it is common practice to separate the momentum dynamics and kinematics. Euler's rotational equations of motion of a rigid body with inertia matrix $\Im$ are usually written in terms of the body angular velocity $\boldsymbol{\omega}$, not in terms of the time derivative of the attitude coordinate vector $\boldsymbol{\theta}$.

$$[I]\dot{\boldsymbol{\omega}} = -\boldsymbol{\omega} \times [I]\boldsymbol{\omega} + \boldsymbol{u} \quad (3.13a)$$

$$\dot{\boldsymbol{\theta}} = f(\boldsymbol{\theta})\boldsymbol{\omega} \quad (3.13b)$$

Eq. (3.13a) describes the system momentum time rate of change and Eq. (3.13b) describes the kinematic relationship between the body angular velocity $\boldsymbol{\omega}$ and the attitude coordinate derivative $\dot{\boldsymbol{\theta}}$. Using only $\boldsymbol{\theta}$ and its derivative instead of $\{\boldsymbol{\theta}, \boldsymbol{\omega}\}$ would yield a much more complex second order differential equation.

This separation of dynamics and kinematics in the equations of motion cannot be accomplished in more general dynamical systems. However, we show a way to accomplish an analogous structure in the more general system equations, at the expense of increasing the number of differential equations to be solved. This involves projecting the configuration coordinate derivative into a moving reference frame[11,44] by introducing a quasivelocity vector which diagonalizes the mass matrix. Since the mass matrix $[M]$ is always symmetric and positive definite, it can be spectrally decomposed using the orthogonal real eigenvector matrix $[E]$ and the diagonal positive real eigenvalue matrix $[D]$. Instead of using $[E]$ directly, using $[C] = [E]^T$ will simplify the following development. Let $\boldsymbol{c}_i$ be the $i$-th eigenvector of $[M(\boldsymbol{x})]$ at any instant, then $[C]$ is written as

$$[C] = [\boldsymbol{c}_1 \cdots \boldsymbol{c}_n]^T \tag{3.14}$$

The spectral decomposition of $[M]$ yields

$$[M] = [C]^T[D][C] \qquad [C][C]^T = I \qquad [D] = diag(\lambda_i) \tag{3.15}$$

Let the diagonal $[S]$ matrix be defined as the positive square root of the eigenvalue matrix $[D]$.

$$[S] = \sqrt{[D]} = diag\left(+\sqrt{\lambda_i}\right) \qquad [D] = [S]^T[S] \tag{3.16}$$

Substituting Eqs.(3.15) and (3.16) into Eq. (3.5) yields the following kinetic energy

expression.

$$T_2 = \frac{1}{2}\dot{\boldsymbol{x}}^T[C]^T[S]^T[S][C]\dot{\boldsymbol{x}} \tag{3.17}$$

The spectral decomposition of Eq. (3.15) is identical to the singular value decomposition of $[M]$ since $[M]$ is symmetric. If needed, the inverse of $[M]$ could be found robustly using the Moore-Penrose inverse. However, using developments below, we avoid $[M]^{-1}$ altogether by introducing the Eigenfactor Quasivelocity coordinate vector $\boldsymbol{\eta}$

$$\boldsymbol{\eta} = [S][C]\dot{\boldsymbol{x}} \qquad \boldsymbol{\eta} = \boldsymbol{\eta}(\lambda_i(\boldsymbol{x}),\boldsymbol{c}_i(\boldsymbol{x}),\dot{\boldsymbol{x}}) \tag{3.18}$$

Using this $\boldsymbol{\eta}$ we obtain a new simplified expression for the kinetic energy. The mass matrix associated with $\boldsymbol{\eta}$ is the identity matrix.

$$T^* = T_2^* + T_1^* + T_0^* = \frac{1}{2}\boldsymbol{\eta}^T\boldsymbol{\eta} + \boldsymbol{G}^T(\boldsymbol{x},t)[C]^T[S]^{-1}\boldsymbol{\eta} + T_0(\boldsymbol{x},t) \tag{3.19}$$

Note that $T_2^*$ depends explicitly only on $\boldsymbol{\eta}$. However, if we choose $(\boldsymbol{x},\dot{\boldsymbol{x}})$ as the independent set for taking partial derivatives, we must recall that $\boldsymbol{\eta}$ depends on $(\boldsymbol{x},\dot{\boldsymbol{x}})$. The $\boldsymbol{x}$ dependence is implicit in Eqs.(3.15), (3.16) and (3.18) because $[S(\boldsymbol{x})]$, $[C(\boldsymbol{x})]$ parameterize $[M(\boldsymbol{x})] = [C]^T[S]^T[S][C]$. Also note that $T^*$ is equal to $T$ (both represent the same physical kinetic energy quantity), they differ only in their algebraic formulations.

The new quasivelocity vector $\eta_i$ can also be expressed as

$$\eta_i = s_i\boldsymbol{c}_i^T\dot{\boldsymbol{x}} \tag{3.20}$$

Or in words, $\eta_i$ is the projection of the velocity vector $\dot{x}$ onto the $i$-th eigenvector $c_i$ and scaled by the $i$-th eigenvalue square root $s_i$. The new velocity coordinate not only contains information about the standard velocity coordinate, but it is also implicitly

linked to the system mass matrix itself. The inverse mapping of Eq. (3.18) describes the kinematic relationship between $\dot{\boldsymbol{x}}$ and $\boldsymbol{\eta}$ similarly to the relationship of $\dot{\boldsymbol{\theta}}$ and $\boldsymbol{\omega}$ in Eq. (3.13b). Since $C$ is orthogonal and the diagonal entries of $S$ are positive, the inverse mapping is trivial and singularity free:

$$\dot{\boldsymbol{x}} = [C]^T[S]^{-1}\boldsymbol{\eta} \tag{3.21}$$

The partial derivatives of the system Lagrangian $\mathcal{L}$ are now rewritten in terms of the new generalized velocity vector $\boldsymbol{\eta}$ using the chain rule as[44]

$$\frac{\partial \mathcal{L}}{\partial \dot{\boldsymbol{x}}} = \frac{\partial T^*}{\partial \dot{\boldsymbol{x}}} + \left(\frac{\partial \boldsymbol{\eta}}{\partial \dot{\boldsymbol{x}}}\right)^T \frac{\partial T^*}{\partial \boldsymbol{\eta}} = [C]^T[S]\frac{\partial T^*}{\partial \boldsymbol{\eta}} \tag{3.22}$$

and

$$\frac{\partial \mathcal{L}}{\partial \boldsymbol{x}} = \frac{\partial T^*}{\partial \boldsymbol{x}} + [J]^T\frac{\partial T^*}{\partial \boldsymbol{\eta}} - \frac{\partial V}{\partial \boldsymbol{x}} \tag{3.23}$$

where $[J]$ is the sensitivity matrix of $\boldsymbol{\eta}$ with respect to the state vector $\boldsymbol{x}$. This matrix is non-zero since the $[C]$ and $[S]$ both indirectly depend on $\boldsymbol{x}$.

$$[J] \equiv \frac{\partial \boldsymbol{\eta}}{\partial \boldsymbol{x}} = \left[\frac{\partial \boldsymbol{\eta}}{\partial x_1}, \cdots, \frac{\partial \boldsymbol{\eta}}{\partial x_n}\right] \tag{3.24}$$

Using the chain rule $\partial\boldsymbol{\eta}/\partial x_k$ is expressed as

$$\frac{\partial \boldsymbol{\eta}}{\partial x_k} = \left(\frac{\partial [S]}{\partial x_k} + [S]\frac{\partial [C]}{\partial x_k}[C]^T\right)[S]^{-1}\boldsymbol{\eta} \tag{3.25}$$

However, finding $\partial[S]/\partial x_k$ and $\partial[C]/\partial x_k$ is difficult to do without resolving the eigenvector, eigenvalue problem. One method to find these partial derivatives is to use the same square root algorithm used in this paper to find $[\dot{S}]$ and $[\dot{C}]$. This method is covered in a technical report.[43] However, this method only allowed the partial eigenfactor derivatives to be evaluated at the discrete integration time steps, not in between them. Because of this, methods such as the Runge-Kutta methods which

require intermediate steps could not be used to forward integrate the equations of motions. Thus Ref. 43 uses a predictor-corrector type integration method instead.

To avoid solving for the computationally expensive $\partial[S]/\partial x_k$ and $\partial[C]/\partial x_k$ terms, $\partial\mathcal{L}/\partial\boldsymbol{x}$ can be solved using $T(\boldsymbol{x},\dot{\boldsymbol{x}})$ instead of $T^*(\boldsymbol{x},\boldsymbol{\eta})$ as was done in Eq. (3.10). The $\dot{\boldsymbol{x}}$ velocities in Eq. (3.10) could be replaced by the new velocity vector $\boldsymbol{\eta}$ through Eq. (3.21), but it is computationally more efficient to keep the $\dot{\boldsymbol{x}}$ terms.

The partial derivative of $T^*$ with respect to $\boldsymbol{\eta}$ is

$$\frac{\partial T^*}{\partial \boldsymbol{\eta}} = \boldsymbol{\eta} + [S]^{-1}[C]\boldsymbol{G}(\boldsymbol{x},t) \tag{3.26}$$

Using Eqs.(3.10), (3.22) and (3.26), the Lagrange equations of motion in Eq. (3.7) become

$$\frac{d}{dt}\left([C]^T[S]\boldsymbol{\eta}+\boldsymbol{G}\right) - \frac{1}{2}\dot{\boldsymbol{x}}^T\frac{\partial[M]}{\partial\boldsymbol{x}}\dot{\boldsymbol{x}} - \frac{\partial\boldsymbol{G}^T}{\partial\boldsymbol{x}}\dot{\boldsymbol{x}} - \frac{\partial T_0}{\partial\boldsymbol{x}} + \frac{\partial V}{\partial\boldsymbol{x}} = \boldsymbol{Q} - [A]^T\boldsymbol{\lambda} \tag{3.27}$$

After carrying out the time derivative and using the orthogonality of the $[C]$ matrix, the following first order differential equation is obtained.[42]

$$\dot{\boldsymbol{\eta}} + [S]^{-1}\left([C][\dot{C}]^T[S] + [\dot{S}]\right)\boldsymbol{\eta} - [S]^{-1}[C]\left(\frac{1}{2}\dot{\boldsymbol{x}}^T\frac{\partial[M]}{\partial\boldsymbol{x}}\dot{\boldsymbol{x}} - \frac{\partial\boldsymbol{G}^T}{\partial\boldsymbol{x}}\dot{\boldsymbol{x}}\right) = [S]^{-1}[C]\boldsymbol{F} - [B]^T\boldsymbol{\lambda} \tag{3.28}$$

where

$$[B] = [A][C]^T[S]^{-1} \tag{3.29}$$

and

$$\boldsymbol{F} = \boldsymbol{Q} - \frac{\partial V}{\partial\boldsymbol{x}} - \dot{\boldsymbol{G}} + \frac{\partial T_0}{\partial x} \tag{3.30}$$

The two first order Eqs (3.21) and (3.28) replace the classical second order equa-

tions of motion in Eq. (3.12). Eq. (3.28) is an interesting special case of quasivelocity Lagrangian mechanics[44,47] for our choice of quasivelocity vector $\boldsymbol{\eta}$. This diagonalized equation of motion is very similar to the one introduced in Ref. 11, except that our new velocity vector $\boldsymbol{\eta}$ is not equal to their $\boldsymbol{v}$ since our parameterization of the mass matrix is different. Note that Eq. (3.28) requires no matrix inverse to be taken thanks to the orthogonality of the [C] matrix. Inverting the [S] matrix is trivial since it is a positive diagonal matrix. At this stage the complex problem of finding the instantaneous matrix inverse has been traded for another kinematics-like problem of solving the associated eigenfactor differential equations.

### 3.3 Mass Matrix Eigenfactor Derivatives

To solve the above quasivelocity Lagrange equations of motion, auxiliary differential equations are required to yield the eigenfactor derivatives with respect to time. A square root algorithm developed by Oshman and Bar-Itzhack to solve the matrix Riccati differential equation[48] was enhanced and extended in Ref. 41 to robustly handle the mass matrix eigenfactor derivatives. The method calculates the instantaneous $[C]$ and $[S]$ matrices and can also handle the very rare case of either repeated eigenvalues with distinct derivatives or with repeated derivatives. Since $[C]$ is an orthogonal matrix it satisfies a differential equation of the form[5,22,27,41]

$$[\dot{C}] = -[\Omega][C] \tag{3.31}$$

where $[\Omega]$ is a skew-symmetric matrix. Analogous to the attitude dynamics problem where the $[\Omega]$ matrix represents body angular velocities, for the eigenvector dynamics each $\Omega_{ij}$ term represents a generalized eigenvector axis angular velocity. All eigenfactor derivatives of $[M]$ are expressed by a projection onto $[C]$ in terms of $\mu_{ij}$ as[28,41,48,49]

$$\mu_{ij} = \boldsymbol{c}_j^T[\dot{M}(\boldsymbol{x},t)]\boldsymbol{c}_i \tag{3.32}$$

The method in Ref. 41 defines the $[\Omega]$ matrix elements as[28,48]

$$\Omega_{ij} = \begin{cases} \mu_{ij} / \left(s_j^2 - s_i^2\right) & \text{for } |s_j^2 - s_i^2| \geq \epsilon \\ \Omega_{ij}(t_0) \ + \dot{\Omega}_{ij}(t_0)(t_1 - t_0) & \text{for } |s_j^2 - s_i^2| < \epsilon \end{cases} \tag{3.33}$$

where $\epsilon$ is the smallest allowable numerical difference in eigenvalues before numerical problems occur in calculating $\Omega_{ij}$. When $\lambda_i$ differs from $\lambda_j$ by less than $\epsilon$, then the unknown $\Omega_{ij}$ term at $t_1$ is linearly interpolated from known terms at $t_0$. This approximation is shown to have minimal impact on the numerical accuracy of the solution. To enhance long term stability of the eigenfactor integration and handle the theoretical cases of discontinuous eigenvectors, Ref. 41 performs a Jacobi sweep[41,50,51] whenever the $\Omega_{ij}$ term is being approximated. Discontinuous eigenvectors of a continuous and differentiable symmetric positive definite matrix $[M(\boldsymbol{x}(t))]$ are mathematically only possible for the rare case where both the corresponding eigenvalues and their derivatives are repeated.[41]

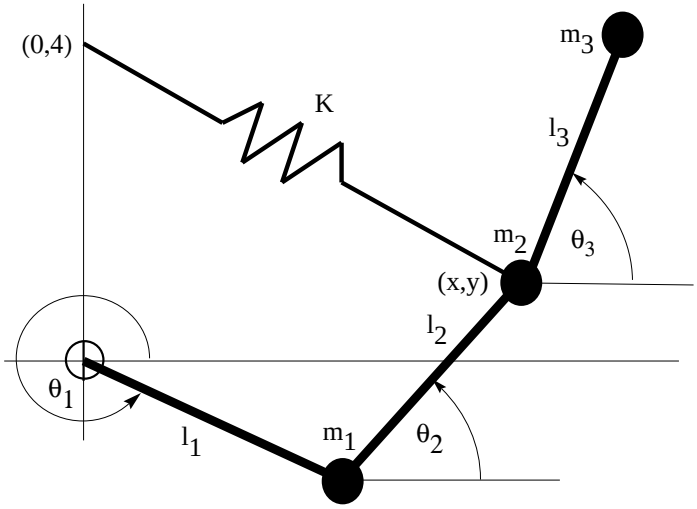


**Fig. 3.1:** Three-Link Manipulator System

To illustrate typical eigenvalue and $\Omega_{ij}$ behavior for a real mechanical system, the simple three-link dynamical system shown in Figure 3.1 is studied. All masses

and rods are set to unit weight and length and the system is initially at rest. The spring constant $K$ is 0.2. The initial orientation angles are $\theta_1 = -90°$, $\theta_2 = -30°$ and $\theta_3 = 0°$. The forward integration is performed with a variable step size third/fourth order Runge-Kutta method. The resulting eigenvalue time evolution for up to 20 seconds is shown in Figure 3.2(i). The eigenvalues $\lambda_2$ and $\lambda_3$ become very close at certain times, yet are never exactly equal. It appears like they repel from each other in the last moment and change directions. This phenomena of "eigenvalue near-misses" is discussed by V. I. Arnold in Appendix 10 of Ref. 52. We note that this is but one "eigenvalue encounter" pathology, for more general problems, the eigenvalues can indeed cross. For the single parameter system mass matrix $M(t)$ it is very unusual to encounter repeated eigenvalues; but it is not impossible. A two-link manipulator can be configured such that the eigenvalues do periodically become equal. If the manipulator chain is allowed to "fork", then it is also possible for eigenvalues to become equal. However, in all physical systems studied so far no system was found that exhibited crossing eigenvalues $\lambda_i$ and $\lambda_j$ *and* had non-zero corresponding $\Omega_{ij}$ terms. If the eigenvalues actually crossed, then their relative eigenaxis angular velocity was always found to be zero. While this pattern has been consistently observed, no claims are made that this will occur for *all* physical systems.

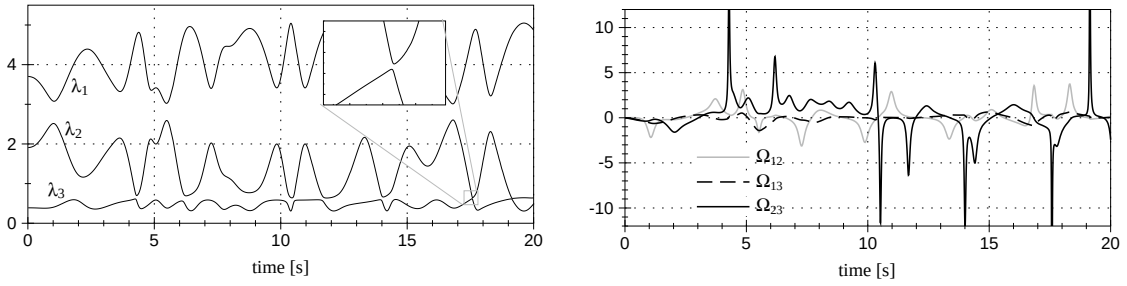


(i) Eigenvalues of System Mass Matrix (ii) Eigenvector Axis Ang. Vel. $\Omega_{ij}$

**Fig. 3.2:** Three-Link Manipulator Simulation

To track the rapid eigenvalue changes near $\lambda_2 \approx \lambda_3$, a variable step size integration method is essential. Every time these two eigenvalues become very close something interesting happens to corresponding eigenvectors. Away from a near eigenvalue encounter the eigenvectors oscillate normally as is seen in their angular velocity measures $\Omega_{ij}$ in Figure 3.2(ii). However, every close approach of $\lambda_2$ and $\lambda_3$ causes the corresponding eigenvector axes to "switch places." This switching is seen as a clear spike in the $\Omega_{23}$ time history in Figure 3.2(ii).

The time derivative of the eigenvalues $\lambda_i$ are defined in terms of $[\mu]$ matrix entries as[28, 41, 48, 49]

$$\dot{\lambda}_i = \mu_{ii} \tag{3.34}$$

However, the time derivative of the eigenvalues is not used directly in the EQV formulation, but the derivative of the eigenvalue square root. Let $s_i$ be the $i$-th entry of the $[S]$ matrix. Using the chain rule, the derivative of $s_i$ is

$$\dot{s}_i = \frac{1}{2s_i}\dot{\lambda}_i \tag{3.35}$$

This is written in a more compact form using the diagonal matrix $[\Gamma] = diag(\mu_{ii})$ as[48]

$$[\dot{S}] = \frac{1}{2}[\Gamma][S]^{-1} \tag{3.36}$$

Substituting Eq. (3.31) into Eq. (3.28), the quasivelocity Lagrange equations of motion are now reduced to

$$\dot{\boldsymbol{\eta}} + [S]^{-1}\left([\Omega][S] + [\dot{S}]\right)\boldsymbol{\eta} - [S]^{-1}[C]\left(\frac{1}{2}\dot{\boldsymbol{x}}^T\frac{\partial[M]}{\partial \boldsymbol{x}}\dot{\boldsymbol{x}} - \frac{\partial \boldsymbol{G}^T}{\partial \boldsymbol{x}}\dot{\boldsymbol{x}}\right) = [S]^{-1}C\boldsymbol{F} - [B]^T\boldsymbol{\lambda} \tag{3.37}$$

At first glance, Eq. (3.37) may seem more complicated than than the original equa-

tions of motion. Keep in mind, however, that $[S]$ and $[\Gamma]$ are diagonal matrices which greatly reduces the computational burden. The most costly terms to compute when evaluating the eigenfactor derivatives are the $\mu_{ij}$ terms in Eq. (3.32). Finding the instantaneous eigenfactors would be a very attractive task for massively parallel computer system since the $\mu_{ij}$ calculation is trivially parallelizable.

### 3.4 Pfaffian Non-Holonomic Constraints

If the dynamical system is unconstrained, then the Pfaffian constraint matrix $[B]$ is zero and Eq. (3.37) is fully defined. However, if the dynamics are constrained through the Pfaffian constraint of Eq. (3.8), then Eq. (3.37) will need to be solved simultaneously with the constraint equation. Using Eq. (3.21) we rewrite the Pfaffian constraint in terms of the new velocity vector $\boldsymbol{\eta}$.

$$[A][C]^T[S]^{-1}\boldsymbol{\eta} + \boldsymbol{b} = 0 \tag{3.38}$$

which can be simplified using Eq. (3.29) to

$$[B]\boldsymbol{\eta} + \boldsymbol{b} = 0 \tag{3.39}$$

The dynamical constraint equation is obtained by taking the first time derivative of Eq. (3.39).

$$[B]\dot{\boldsymbol{\eta}} + [\dot{B}]\boldsymbol{\eta} + \dot{\boldsymbol{b}} = 0 \tag{3.40}$$

Using Eqs. (3.36), (3.31) and (3.29) $[\dot{B}]$ can be expressed as

$$[\dot{B}] = \left([\dot{A}][C]^T + [A][\dot{C}]^T - [B][\dot{S}]\right)[S]^{-1} \tag{3.41}$$

To determine the vector $(\dot{\boldsymbol{\eta}}, \boldsymbol{\lambda})$ Eq. (3.37) will need to be solved simultaneously with Eq. (3.40). This leads to the differential-algebraic equations (DAE)

$$\begin{bmatrix} I & [B]^T \\ [B] & 0 \end{bmatrix} \begin{pmatrix} \dot{\boldsymbol{\eta}} \\ \boldsymbol{\lambda} \end{pmatrix} = \begin{pmatrix} \boldsymbol{a}_1 \\ \boldsymbol{a}_2 \end{pmatrix} \tag{3.42}$$

where the vectors $\boldsymbol{a}_1$ and $\boldsymbol{a}_2$ are given as

$$\boldsymbol{a}_1 = -[S]^{-1}\left([\Omega][S] + [\dot{S}]\right)\boldsymbol{\eta} + [S]^{-1}[C]\left(\frac{1}{2}\dot{\boldsymbol{x}}^T\frac{\partial[M]}{\partial \boldsymbol{x}}\dot{\boldsymbol{x}} - \frac{\partial \boldsymbol{G}^T}{\partial \boldsymbol{x}}\dot{\boldsymbol{x}} + \boldsymbol{F}\right) \tag{3.43a}$$

$$\boldsymbol{a}_2 = -[\dot{B}]\boldsymbol{\eta} - \dot{\boldsymbol{b}} \tag{3.43b}$$

Since $[B]$ is a $m$x$n$ matrix, $[M_2]$ is a symmetric $(n+m)$x$(n+m)$ matrix. A partitioned matrix inversion formula[28] is used to find the inverse of $[M_2]$. Because of the use of the quasivelocity vector $\boldsymbol{\eta}$, the upper left partition of $[M_2]$ is a $n$x$n$ identity matrix which simplifies the partitioned inverse immensely. For this case the $m$x$m$ Schur complement matrix $[\Delta]$ reduces to[28]

$$[\Delta] = [B][B]^T \tag{3.44}$$

making the partitioned inverse of $[M_2]$

$$[M_2]^{-1} = \begin{bmatrix} I - [B]^T[\Delta]^{-1}[B] & [B]^T[\Delta]^{-1} \\ [\Delta]^{-1}[B] & -[\Delta]^{-1} \end{bmatrix} \tag{3.45}$$

Using $[M_2]^{-1}$ in Eq. (3.45) the constrained differential equation of motion for $\boldsymbol{\eta}$ is

$$\dot{\boldsymbol{\eta}} = (I - [B]^T[\Delta]^{-1}[B])\boldsymbol{a}_1 + [B]^T[\Delta]^{-1}\boldsymbol{a}_2 \tag{3.46}$$

The Lagrange constraint vector $\boldsymbol{\lambda}$ is

$$\boldsymbol{\lambda} = [\Delta]^{-1}[B]\boldsymbol{a}_1 - [\Delta]^{-1}\boldsymbol{a}_2 \tag{3.47}$$

Note that if no constraints are imposed on the dynamical system, then Eq. (3.46) collapses back to Eq. (3.37). If the number of system constraints $m$ is small, then the $m$x$m$ matrix $[\Delta]^{-1}$ could be inverted for each time step. However, as $m$ grows larger taking a numerical inverse quickly grows in computational complexity.

Since $[\Delta]$, for linearly independent constraints, is a positive definite symmetric matrix by Eq. (3.44), it can be decomposed using the eigenfactor parameterization analogous to the mass matrix parameterization. Let $[C_\Delta]$ be the transpose of the eigenvector matrix of $[\Delta]$, and let $[S_\Delta]$ be a diagonal matrix whose entries are the positive roots of $[\Delta]$ eigenvalues. Then through a spectral decomposition $[\Delta]$ can be written as

$$[\Delta] = [C_\Delta]^T [S_\Delta]^T [S_\Delta][C_\Delta] \tag{3.48}$$

Since $[C_\Delta]$ is an orthogonal matrix and the diagonal entries of $[S_\Delta]$ are all positive, the inverse of $[\Delta]$ is

$$[\Delta]^{-1} = [C_\Delta]^T [S_\Delta]^{-2} [C_\Delta] \tag{3.49}$$

This direct inverse formulation reduces Eq. (3.46) to the following matrix inverse free formulation.

$$\dot{\boldsymbol{\eta}} = (I - [B]^T [C_\Delta]^T [S_\Delta]^{-2} [C_\Delta][B])\boldsymbol{a}_1 + [B]^T [C_\Delta]^T [S_\Delta]^{-2} [C_\Delta]\boldsymbol{a}_2 \tag{3.50}$$

Keep in mind that $[S_\Delta]$ is a diagonal matrix with positive entries. Therefore finding its inverse involves only scalar inversions.

To update the $[C_\Delta]$ and $[S_\Delta]$ matrices without resolving the eigenvalue, eigenvector problem, their time derivatives are found using the square root eigenfactor algorithm[41] analogously to finding the time derivatives of $[C]$ and $[S]$ of the mass

matrix $[M]$. Let $\boldsymbol{c}_{\Delta_i}$ be the $i$-th eigenvector of $[C_\Delta]$, then $\beta_{ij}$ is defined as

$$\beta_{ij} = \boldsymbol{c}_{\Delta_j}[\dot{\Delta}]\boldsymbol{c}_{\Delta_i}^T \tag{3.51}$$

where the time derivative of $[\Delta]$ is

$$[\dot{\Delta}] = [\dot{B}][B]^T + [B][\dot{B}]^T \tag{3.52}$$

and $[\dot{B}]$ was defined in Eq. (3.41). The diagonal matrix $[\Gamma_\Delta]$ and the skew-symmetric matrix $[\Omega_\Delta]$ are then defined as

$$[\Gamma_\Delta] = diag(\beta_{ii}) \tag{3.53}$$

$$[\Omega_{\Delta_{ij}}] = \begin{cases} \frac{\beta_{ij}}{s^2_{\Delta_j} - s^2_{\Delta_i}} & \text{for } |s^2_{\Delta_j} - s^2_{\Delta_i}| \geq \epsilon \\ \Omega_{\Delta_{ij}}(t_0) \ + \dot{\Omega}_{\Delta_{ij}}(t_0)(t_1 - t_0) & \text{for } |s^2_{\Delta_j} - s^2_{\Delta_i}| < \epsilon \end{cases} \tag{3.54}$$

The time derivatives of $[C_\Delta]$ and $[S_\Delta]$ are written as[48]

$$[\dot{S}_\Delta] = \frac{1}{2}[\Gamma_\Delta][S_\Delta]^{-1} \tag{3.55}$$

$$[\dot{C}_\Delta] = -[\Omega_\Delta][C_\Delta] \tag{3.56}$$

### 3.5 Numerical Simulations

Two numerical studies simulating distinct dynamical systems are presented in this section. This first study shows a case where it is beneficial to use the EQV and illustrates that dynamical systems do exists that have crossing eigenvalues. The second study deals with a more complicated constrained multi-link system which illustrates the typical EQV property of dealing with "near-eigenvalue misses."

### *3.5.1 Unconstrained Two-Link Simulation*

The first dynamical system studied is a two-link manipulator system whose shoulder is inertially fixed, but free to rotate. This system is identical to the one illustrated in Figure 3.1 without the third link. Each link is of length $l_i$ with all it's mass $m_i$ located at the tip. The configuration angles $\theta_i$ are measured from the local horizon. The manipulator hand is attached to an inertial point at coordinates (0,4) through a spring with stiffness $K$. Let $\boldsymbol{\theta} = (\theta_1, \theta_2)^T$ be the state configuration vector. The system potential energy is the total spring energy given as

$$V(\boldsymbol{\theta}) = \frac{1}{2}K\left((4-y)^2 + x^2\right) \tag{3.57}$$

The system kinetic energy is given as

$$T(\boldsymbol{\theta}, \dot{\boldsymbol{\theta}}) = \frac{1}{2}m_1 l_1^2 \dot{\theta}_1^2 + \frac{1}{2}m_2\left(l_1^2\dot{\theta}_1^2 + 2l_1 l_2 \cos(\theta_1 - \theta_2)\dot{\theta}_1\dot{\theta}_2 + l_2^2\dot{\theta}_2^2\right) \tag{3.58}$$

From the kinetic energy $T$ the system mass matrix $[M]$ can be extracted.

$$[M(\boldsymbol{\theta})] = \begin{bmatrix} (m_1+m_2)l_1^2 & m_2 l_1 l_2 \cos(\theta_1 - \theta_2) \\ m_2 l_1 l_2 \cos(\theta_1 - \theta_2) & m_2 l_2^2 \end{bmatrix} \tag{3.59}$$

The eigenfactor square root algorithm requires an algebraic expression for $[\dot{M}]$ and $\partial[M]/\partial\theta_k$. They are found directly from the system mass matrix $[M]$ in Eq. (3.59).

$$[\dot{M}(\boldsymbol{\theta}, \dot{\boldsymbol{\theta}})] = \begin{bmatrix} 0 & m_2 l_1 l_2 \sin(\theta_1 - \theta_2)(\dot{\theta}_2 - \dot{\theta}_1) \\ m_2 l_1 l_2 \sin(\theta_1 - \theta_2)(\dot{\theta}_2 - \dot{\theta}_1) & 0 \end{bmatrix} \tag{3.60}$$

$$\frac{\partial[M(\boldsymbol{\theta})]}{\partial\theta_1} = \begin{bmatrix} 0 & -m_2 l_1 l_2 \sin(\theta_1 - \theta_2) \\ -m_2 l_1 l_2 \sin(\theta_1 - \theta_2) & 0 \end{bmatrix} \tag{3.61}$$

$$\frac{\partial[M(\boldsymbol{\theta})]}{\partial\theta_2} = \begin{bmatrix} 0 & m_2 l_1 l_2 \sin(\theta_1 - \theta_2) \\ m_2 l_1 l_2 \sin(\theta_1 - \theta_2) & 0 \end{bmatrix} \tag{3.62}$$

**Table 3.1:** Parameters of Unconstraint Two-Link Simulation

| Parameter | Value | Units |
|---|---|---|
| $l_1$ | 0.5 | m |
| $l_2$ | $1/\sqrt{2}$ | m |
| $m_1$ | 1.0 | kg |
| $m_2$ | 1.0 | kg |
| $K$ | 1.0 | kg/sec$^2$ |
| $\boldsymbol{\theta}(t_0)$ | [0.0 60.0] | deg |
| $\dot{\boldsymbol{\theta}}(t_0)$ | [0.0 0.0] | deg/sec |

The simulation parameters are provided in Table 3.1. The link lengths and masses were chosen such that the mass matrix eigenvalues are time varying and could become equal. The geometric condition for $\lambda_1 = \lambda_2$ is that $|\theta_2 - \theta_1| = 90$ degrees. However, as mentioned earlier, the eigenvector axis angular velocity $\Omega_{12}$ is always zero for this system. This pattern was observed with every mechanical system studied. Whenever two eigenvalues $\lambda_i$ and $\lambda_j$ do potentially cross, then the corresponding $\Omega_{ij}$ is always zero. Therefore this example cannot be used to study the effect of near-equal eigenvalues since the critical $\Omega_{12}$ calculation is trivial. However, this example will provide some good insight into what potential benefits there are in using EQV $\boldsymbol{\eta}$ as the velocity measure instead of the standard $\dot{\boldsymbol{\theta}}$.

The initial motion of the two-link system defined in Table 3.1 is shown in Figure 3.3. A constant step size fourth order Runge-Kutta method was used to numerically integrate the system. The links ended up oscillating back and forth between the right and the left side. The initial conditions for this simulation were chosen such that the two links come close to being fully stretched as they pass the vertical axis. Since the spring is located on the vertical axis and is pulling the manipulator hand essentially upwards, the two-links systems end up "snapping" through this orientation and experience locally very high accelerations.

The configuration angles $\theta_i$ and angle accelerations $\ddot{\theta}_i$ are shown in Figures 3.4(i)

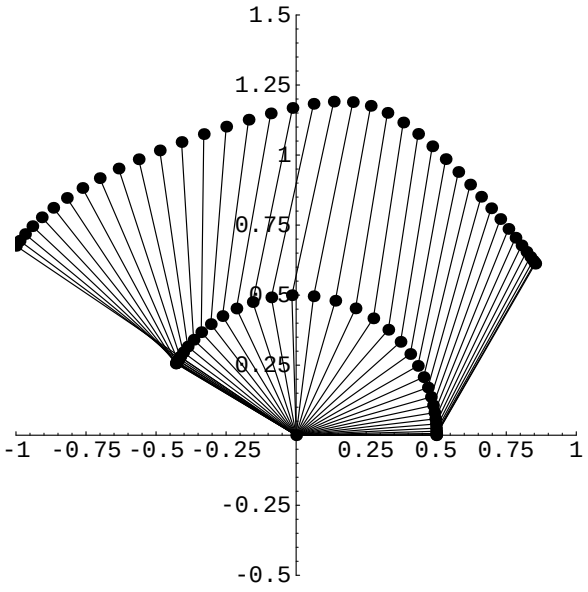


**Fig. 3.3:** Initial Motion of Two-Link System

and 3.4(ii) respectively with highlights where $\theta_1 \simeq \theta_2$. Combined both figures illustrate this "snap through" behavior very clearly. Whenever $\theta_1 \simeq \theta_2$, the angular accelerations $\ddot{\theta}_i$ change sharply. Therefore integrating the system with $(\boldsymbol{\theta}, \dot{\boldsymbol{\theta}})$ as the state vector would require drastically reducing the integration step size during these "snap-through's." However, using $(\boldsymbol{\theta}, \boldsymbol{\eta})$ as the state vector the angular accelerations look quite different. During these "snap-through's" the $\dot{\eta}_i$ coordinates don't change nearly as fast as the $\ddot{\theta}_i$ coordinates do. The explanation for this is given in Eq. (3.20). Since $\eta_i = s_i \boldsymbol{c}_i^T \dot{\boldsymbol{x}}$, the EQVs represent an angular momentum like quantity which does not change as sharply as the "pure" angular velocities $\ddot{\theta}_i$.

Since this two-link manipulator system is conservative the total energy $E$ is constant and can be used as a measure of integration accuracy. The total energy error $\delta E$ encountered during the integration is

$$\delta E(\boldsymbol{\theta}, \dot{\boldsymbol{\theta}}) = T(\boldsymbol{\theta}, \dot{\boldsymbol{\theta}}) + V(\boldsymbol{\theta}) - E(t_0) \tag{3.63}$$

The EQV formulation was compared to two other methods. Method 2 uses $\dot{\boldsymbol{\theta}}$ as its

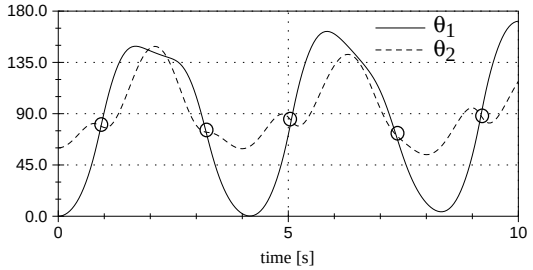


(i) Configuration Angles $\theta_i$

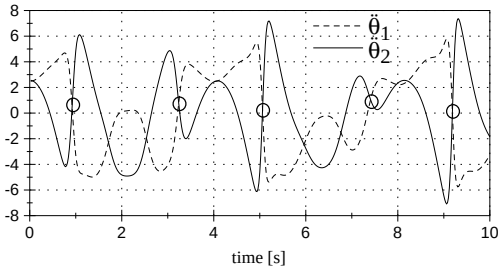


(ii) Configuration Angle Acceleration $\ddot{\theta}_i$

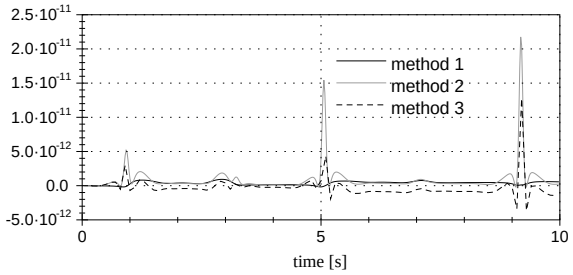


(iii) Total Energy Error $\delta E$

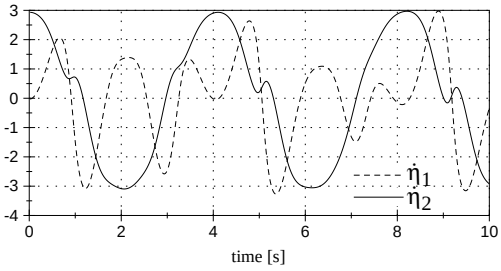


(iv) Quasivelocity Derivatives $\dot{\eta}_i$

**Fig. 3.4:** Unconstrained Two-Link Simulation Results

velocity coordinate vector but inverts the mass matrix using its spectral decomposition $[M]^{-1} = [C][S]^{-2}[C]^T$. Method 3 uses $\dot{\boldsymbol{\theta}}$ as the velocity coordinate vector and inverts the mass matrix by "brute force" using an LU decomposition. The numerical accuracy of each method is shown in Figure 3.4(iii). Since a constant step size integration was used, method 3 clearly performs very poorly during the snap-through's and starts to generate a non-zero offset in $\delta E$. Method 2 performs a little better than method 3 during the snap-through's and does not appear to generate any longterm energy errors. At least for this simulation method 1, which uses the EQV formulation, provided the best integration. The greatest numerical effort with the EQV formulation is calculating the $[\mu]$ matrix which is a $n^3$ operation. For a given integration step size even the "brute-force" method using the LU decomposition for inverting the

mass matrix only requires a $n^2$ type operator. More elegant methods such as the innovations factorization using in Ref. 11 are only $n$-th order operators. However, given the encouraging preliminary results in Figure 3.4 it was anticipated that the EQV would allow for a larger integration step size to offset the penalty of having a larger numerical effort per integration step. As will be discussed in the following numerical simulation, unfortunately this was not generally the case. For more complex system the required integration step size is roughly equal when using either the classical or the EQV formulation.

### *3.5.2 Constrained Multi-Link Simulation*

The second dynamical system is a semi-flexible multi-link system illustrated in Figure 3.5. The two-link subsystem is very similar to the previous dynamical system. The only difference is that the first link is now able to stretch without bending. The stretching is simulated by the spring $K_1$ and the amount stretched in indicated through the coordinate $\theta_3$. At the shoulder of the two-link system another link is added. A torsional spring $K_3$ connects these two link subsystems. Studying this system will provide some more insight into how typical mass matrix eigenfactors behave. Further, it illustrates how Eq. (3.46) is used to incorporate constraint into the EQV formulation.

The hand coordinate $y$ of the two-link subsystem in the vertical direction is given by

$$y = (l_1 + \theta_3)\sin\theta_1 + l_2 \sin\theta_2 \tag{3.64}$$

The system potential energy is the total spring energy given by

$$V(\boldsymbol{\theta}) = \frac{1}{2}K_1\theta_3^2 + \frac{1}{2}K_2\left(x^2 + (4-y)^2\right) + \frac{1}{2}K_3(\theta_4 - \theta_1 - \frac{\pi}{2})^2 \tag{3.65}$$

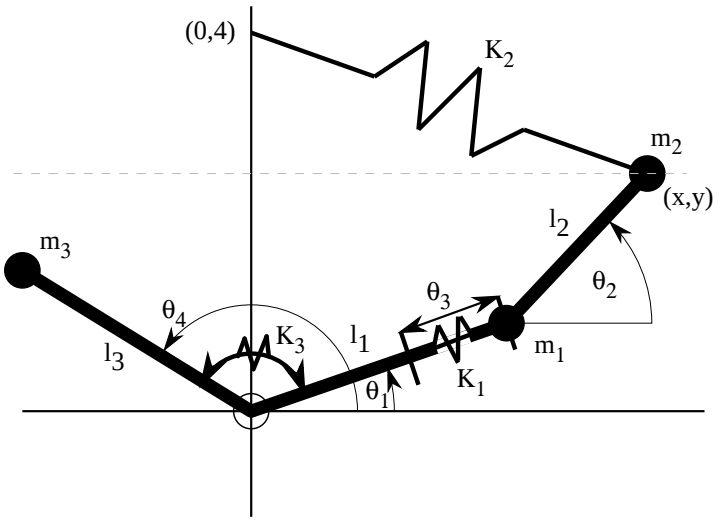


**Fig. 3.5:** Semi-Flexible Multi-Link System Layout

The system kinetic energy is given as

$$T = \frac{1}{2}m_1\left((l_1+\theta_3)^2\dot{\theta}_1^2+\dot{\theta}_3^2\right)+\frac{1}{2}m_3 l_3^2\dot{\theta}_4^2+\frac{1}{2}m_2\left((l_1+\theta_3)^2\dot{\theta}_1^2+l_2^2\dot{\theta}_2^2 \right.$$
$$\left.+\dot{\theta}_3^2+2(l_1+\theta_3)l_2\cos(\theta_1-\theta_2)\dot{\theta}_1\dot{\theta}_2+2l_2\sin(\theta_1-\theta_2)\dot{\theta}_2\dot{\theta}_3\right) \quad (3.66)$$

From the kinetic energy $T$ the system mass matrix can be extracted.

$$M(\boldsymbol{\theta}) = \begin{bmatrix} (m_1+m_2)L_1^2 & m_2L_1l_2\cos(\theta_{12}) & 0 & 0 \\ m_2L_1l_2\cos(\theta_{12}) & m_2l_2^2 & m_2l_2\sin(\theta_{12}) & 0 \\ 0 & m_2l_2\sin(\theta_{12}) & m_1+m_2 & 0 \\ 0 & 0 & 0 & m_3l_3^2 \end{bmatrix} \quad (3.67)$$

where the shorthand notations $\theta_{12} = \theta_1 - \theta_2$ and $L_1 = l_1 + \theta_3$ were used. The eigenfactor square root algorithm requires an algebraic expression for $\dot{M}$ and $\partial M/\partial\theta_k$. They are found directly by appropriate differentiations of the system mass matrix $M$ in Eq. (3.67).

This dynamical system will be constrained such that the hand of the two-link sub-

system can only move in the horizontal direction. This constraint therefore requires that $\dot{y} = 0$. Using Eq. (3.64) this can be expressed as $A(\boldsymbol{\theta})\dot{\boldsymbol{\theta}} = 0$ where

$$A(\boldsymbol{\theta}) = \begin{bmatrix} (l_1 + \theta_3)\cos\theta_1 & l_2\cos\theta_2 & \sin\theta_1 & 0 \end{bmatrix} \tag{3.68}$$

The simulation parameters are shown in Table 3.2. The torsional spring $K_3$ is assumed to be unstretched whenever $|\theta_4 - \theta_1| = 90$ degrees.

**Table 3.2:** Parameters of Constraint Multi-Link Simulation

| Parameter | Value | Units |
|---|---|---|
| $l_1$ | 0.5 | m |
| $l_2$ | $1/\sqrt{2}$ | m |
| $l_3$ | 1.5 | m |
| $m_1$ | 1.0 | kg |
| $m_2$ | 1.0 | kg |
| $m_3$ | 1.0 | kg |
| $K_1$ | 1.0 | kg/sec$^2$ |
| $K_2$ | 1.0 | kg/sec$^2$ |
| $K_3$ | 0.5 | kg-m$^2$/sec$^2$ |
| $[\theta_1(t_0), \theta_2(t_0), \theta_4(t_0)]$ | [30 60 135] | deg |
| $\theta_3(t_0)$ | 0.0 | m |
| $[\dot{\theta}_1(t_0), \dot{\theta}_2(t_0), \dot{\theta}_4(t_0)]$ | [0.0 0.0 0.0] | deg/sec |
| $\dot{\theta}_3(t_0)$ | 0.0 | m/sec |

The numerical integration was performed with a 3rd/4th order variable step-size Runge-Kutta method. The resulting initial motion is illustrated in Figure 3.6. As required by the system constraint, the hand of the two-link sub-system only moves in a horizontal manner. These motions were verified using the classical Lagrangian formulation along with the "brute force" integration method outlined with the previous simulation. Note that using Eq. (3.46) only requires solving an $n$-th order system instead of the standard $(n + m)$-th order system for dynamical systems with $m$ constraints present.

The matrix eigenvalues $\lambda_i$ are shown in Figure 3.7(i). The eigenvalue $\lambda_1$ remains

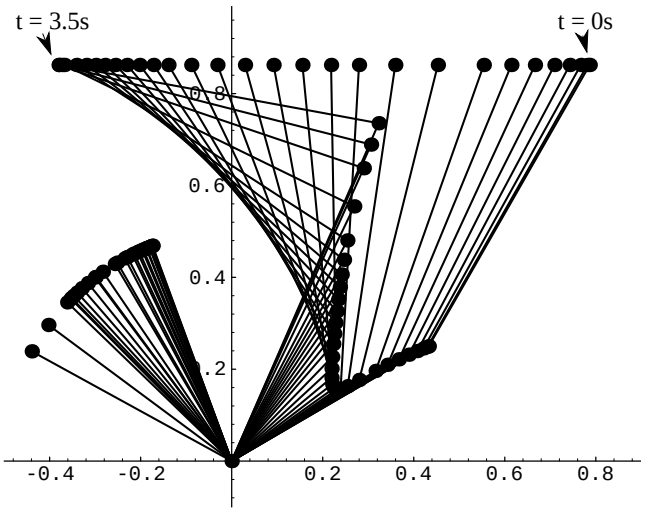


**Fig. 3.6:** Constrained Multi-Link Motion

constant for this system while the other vary with time. The corresponding eigenaxis angular velocities $\Omega_{ij}$ are shown in Figure 3.7(ii). For this dynamical system, the eigenaxis angular velocities $\Omega_{12}$, $\Omega_{13}$ and $\Omega_{14}$ are always zero. This is because the corresponding $\mu_{1i}$ terms are all zero. Therefore having $\lambda_2$ cross $\lambda_1$ does not pose any numerical difficulties when computing Eq. (3.33). The eigenvalue $\lambda_2$ is even able to remain very close to $\lambda_1$ for finite periods of time without causing numerical problems. Clearly this eigenvalue represents the separate link $l_3$ whose motion is only indirectly linked to the other links.

The remaining three eigenvalues $\lambda_2$, $\lambda_3$ and $\lambda_4$ represent the two-link subsystem. These eigenvalues will vary with time, but will never cross. Eigenvalues that corresponded to a single chain of links were never found to cross. For chains with more links than two, the only way found to make corresponding eigenvalues cross was to fork the chain as was done in this dynamical system. Figure 3.7(i) again shows the phenomenon of eigenvalue "near-misses" that were discussed Arnold in Ref. 52. At times two eigenvalue pairs appear to be crossing, but repel off eachother before doing

so. Figure 3.7(ii) shows that the corresponding $\Omega_{ij}$ always grows rather large when such an eigenvalue near-miss occurs. Even though the behavior of $\boldsymbol{\theta}$ and $\boldsymbol{\eta}$ might be perfectly smooth for these occurrences, the variable step size integrator is required to reduce the step size drastically here to accurately forward integrate the current eigenfactors.

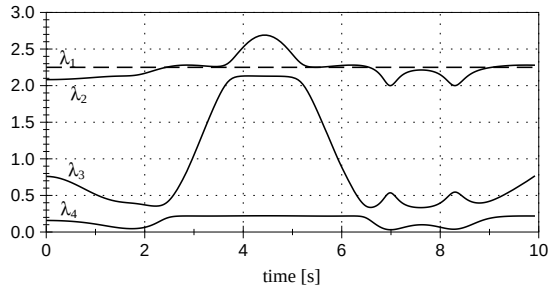


(i) Mass Matrix Eigenvalues $\lambda_i$

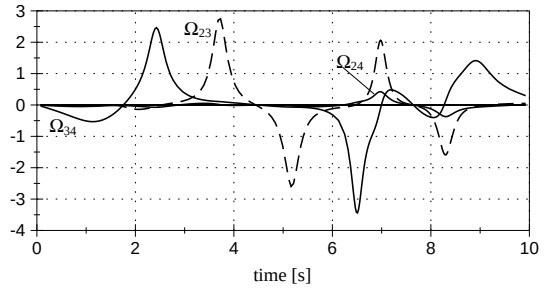


(ii) Eigenaxis Ang. Vel. $\Omega_{ij}$

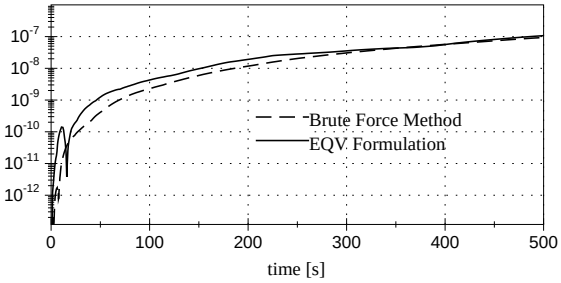


(iii) Constraint error $\Delta y$

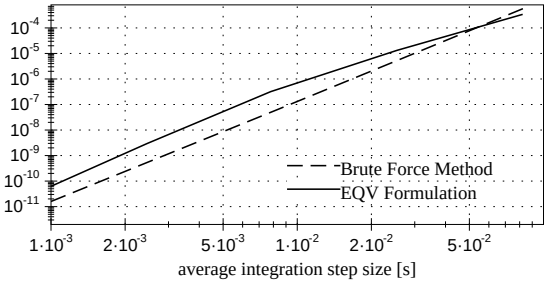


(iv) Integration Accuracy $|\Delta E|$

**Fig. 3.7:** Constrained Multi-Link Simulation Results

The previous unconstrained system encountered some snap-through's where it proved beneficial to use the EQV formulation. However, integrating the eigenfactors was also rather simple. For this more complex dynamical system the EQV formulation does appear to offer any computational benefits over the simple brute force method. In Figure 3.7(iii) the constraint error $\Delta y(t) = |y(t) - y(t_0)|$ obtained through the EQV formulation is compared to that of a numerical simulation using the brute

force method. Both methods use the same variable step size technique. However, due to the behavior of the eigenfactors, the step sizes taken by each methods are quite different. To provide a fair comparison each simulation was setup such that the average integration step size was about 0.0027 seconds for each method. As Figure 3.7(iii) shows, the constraint error violation was of roughly the same magnitude for either method. This was also confirmed testing other constrained dynamical systems.

Since the dynamical system is conservative, the total energy $E = T + V$ can again be used as a measure of the total integration accuracy. The integration error $|\Delta E|$ is defined to be

$$|\Delta E| = \int_0^{t_f} |E(t) - E(t_0)| dt \tag{3.69}$$

The brute force method and the EQV formulation integration errors for a 100 second simulation are compared in Figure 3.7(iv). Per average integration step the EQV method actually proved to be about one order of magnitude less accurate than the brute force method. Therefore, even after taking into account that the evaluation of the computationally most expensive term $\Omega_{ij}$ is trivially parallelizable, the remaining numerical effort involved in using the EQV formulation for running simulations still remains too high. While the EQV formulation is of interest by itself, since it provides some interesting insight into a complex dynamical system, it is not recommended that this formulation is used to run numerical simulations of complex systems. In the next section, we will establish that the important practical application for the EQV formulation lies elsewhere.

## 3.6 Eigenfactor Quasivelocity Feedback Law

This section will investigate the use of the EQVs as a velocity feedback measure rather than the standard $\dot{\boldsymbol{x}}$. This is analogous to feedback control laws in rigid body dynamics where $\boldsymbol{\omega}$ is fed back instead of $\dot{\theta}$. In particular, the effect of the nonlinear generalized coriolis term in the EQV formulation is studied. The resulting EQV feedback control law is shown to be asymptotically stabilizing and provide some elegant decoupling properties to complex dynamical motions.

### *3.6.1 Feedback Control Law*

An unconstrained version of the EQV formulation given in Eq. (3.28) can be compactly written as

$$\dot{\boldsymbol{\eta}} = -\boldsymbol{H}(\boldsymbol{x}, \boldsymbol{\eta}) + \boldsymbol{\epsilon} \tag{3.70}$$

The vector $\boldsymbol{H}$ is the nonlinear, generalized coriolis term

$$\boldsymbol{H}(\boldsymbol{x}, \boldsymbol{\eta}) = [S]^{-1}\left([\Omega][S] + [\dot{S}]\right)\boldsymbol{\eta} - [S]^{-1}[C]\left(\frac{1}{2}\dot{\boldsymbol{x}}^T[M_{\boldsymbol{x}}]\dot{\boldsymbol{x}}\right) \tag{3.71}$$

where $[M_{\boldsymbol{x}}] = \partial[M]/\partial\boldsymbol{x}$. The vector $\boldsymbol{\epsilon}$ is the generalized forcing term defined as

$$\boldsymbol{\epsilon} = [S]^{-1}[C](\boldsymbol{Q} - \frac{\partial V}{\partial \boldsymbol{x}}) \tag{3.72}$$

Because of the close relationship between this EQV formulation and the classical rigid body attitude dynamics formulation, the question naturally arises: Does the EQV vector have an important role in feedback laws, analogous to the $\boldsymbol{\omega}$ vector in attitude control? To gain some insight, first recall the Euler equation of motion of a rigid body given as

$$[I]\dot{\boldsymbol{\omega}} = -[\tilde{\omega}][I]\boldsymbol{\omega} + \boldsymbol{u} \tag{3.73}$$

where $[I]$ is again the inertia matrix, $\boldsymbol{u}$ is an external torque vector. The kinetic energy of a rotating rigid body is given as

$$T = \frac{1}{2}\boldsymbol{\omega}^T[I]\boldsymbol{\omega} \tag{3.74}$$

It is a known that the term $[\tilde{\omega}]I\boldsymbol{\omega}$ is a non-working term and that the kinetic energy rate can be written as the power equation[5,25]

$$\dot{T} = \boldsymbol{\omega}^T\boldsymbol{u} \tag{3.75}$$

Using the kinetic energy as a Lyapunov function, the simple feedback control law

$$\boldsymbol{u} = -[P^{\omega}]\boldsymbol{\omega} \tag{3.76}$$

is found where $[P^{\omega}]$ is a positive definite angular velocity feedback gain matrix. If $\boldsymbol{\omega}$ is the only state being controlled this controller is globally asymptotically stable.

Analogous statements can be made for the EQV formulation. Similar as in Ref. 11, the nonlinear coriolis term $\boldsymbol{H}(\boldsymbol{x},\boldsymbol{\eta})$ for the EQV formulation is also non-working. To show this *important* truth, let us study the term $\boldsymbol{\eta}^T\boldsymbol{H}$. Using Eq. (3.18) it can be written as

$$\boldsymbol{\eta}^T\boldsymbol{H} = \dot{\boldsymbol{x}}^T\dot{[C]}^T[S]^2[C]\dot{\boldsymbol{x}} + \dot{\boldsymbol{x}}^T[C]^T[\dot{S}][S][C]\dot{\boldsymbol{x}} - \frac{1}{2}\dot{\boldsymbol{x}}^T\left(\dot{\boldsymbol{x}}^T[M_{\boldsymbol{x}}]\dot{\boldsymbol{x}}\right) \tag{3.77}$$

which is the simplified to

$$\boldsymbol{\eta}^T\boldsymbol{H} = \dot{\boldsymbol{x}}^T\left([\dot{C}]^T[S]^2[C] + [C]^T[\dot{S}][S][C]\right)\dot{\boldsymbol{x}} - \frac{1}{2}\left[\sum_i^n \dot{\boldsymbol{x}}_i\left(\dot{\boldsymbol{x}}^T[M_{x_i}]\dot{\boldsymbol{x}}\right)\right] \tag{3.78}$$

Note the following identity.

$$\sum_i^n \dot{\boldsymbol{x}}_i\left(\dot{\boldsymbol{x}}^T[M_{x_i}]\dot{\boldsymbol{x}}\right) = \dot{\boldsymbol{x}}^T\dot{[M]}\dot{\boldsymbol{x}} \tag{3.79}$$

After adding and subtracting some terms $\boldsymbol{\eta}^T\boldsymbol{H}$ becomes

$$\boldsymbol{\eta}^T\boldsymbol{H} = \dot{\boldsymbol{x}}^T \Big( [\dot{C}]^T[S]^2[C] + [C]^T[S]^2[\dot{C}] + 2[C]^T[\dot{S}][S][C] - [C]^T[S]^2[\dot{C}] \\ -[C]^T[\dot{S}][S][C] \Big) \dot{\boldsymbol{x}} - \frac{1}{2}\dot{\boldsymbol{x}}^T[\dot{M}]\dot{\boldsymbol{x}} \quad (3.80)$$

From Eq. (3.15) it is clear that

$$[\dot{M}] = [\dot{C}]^T[S]^2[C] + [C]^T[S]^2[\dot{C}] + 2[C]^T[\dot{S}][S][C] \quad (3.81)$$

This identity is used to reduce $\boldsymbol{\eta}^T\boldsymbol{H}$ to

$$\boldsymbol{\eta}^T\boldsymbol{H} = \dot{\boldsymbol{x}}^T \left( [\dot{M}] - ([S][C])^T \frac{d}{dt}([S][C]) \right) \dot{\boldsymbol{x}} - \frac{1}{2}\dot{\boldsymbol{x}}^T[\dot{M}]\dot{\boldsymbol{x}} \quad (3.82)$$

which can be further manipulated to give the *very important* result:

$$\boldsymbol{\eta}^T\boldsymbol{H} = \dot{\boldsymbol{x}}^T \left( [\dot{M}] - \frac{1}{2}[\dot{M}] \right) \dot{\boldsymbol{x}} - \frac{1}{2}\dot{\boldsymbol{x}}^T[\dot{M}]\dot{\boldsymbol{x}} = 0 \quad (3.83)$$

Recall that the kinetic energy of a dynamical system expressed in the EQV formulation is $T = \frac{1}{2}\boldsymbol{\eta}^T\boldsymbol{\eta}$. Since the $\boldsymbol{H}(\boldsymbol{x}, \boldsymbol{\eta})$ term is nonworking, the kinetic energy rate can be expressed simply as

$$\dot{T} = \boldsymbol{\eta}^T\dot{\boldsymbol{\eta}} = \boldsymbol{\eta}^T(-\boldsymbol{H}(\boldsymbol{x}, \boldsymbol{\eta}) + \boldsymbol{\epsilon}) = \boldsymbol{\eta}^T\boldsymbol{\epsilon} \quad (3.84)$$

Using the kinetic energy as a Lyapunov function, the following feedback control law can be shown to be globally asymptotically stabilizing.

$$\boldsymbol{\epsilon} = -[P^\eta]\boldsymbol{\eta} \quad (3.85)$$

where $[P^\eta]$ is the positive definite velocity feedback gain matrix. Note that Eq. (3.85) provides a linear velocity feedback control law in the $\boldsymbol{\eta}$ formulation. This renders $\dot{T}$

in Eq. (3.84) into the negative definite expression

$$\dot{T} = -\boldsymbol{\eta}^T P^{\eta} \boldsymbol{\eta} \tag{3.86}$$

Therefore $\boldsymbol{\epsilon} = -P^{\eta}\boldsymbol{\eta}$ is a globally asymptotically stabilizing feedback control law for Eq. (3.70). Eq. (3.72) is used to rewrite this control law in terms of the generalized external force vector $\boldsymbol{Q}$.

$$\boldsymbol{Q} = V_x(\boldsymbol{x}) - [C]^T[S][P^{\eta}]\boldsymbol{\eta} \tag{3.87}$$

If the feedback gain $[P^{\eta}]$ is assumed to be a scalar, then the control laws simplifies to

$$\boldsymbol{Q} = V_x(\boldsymbol{x}) - P^{\eta}[M(\boldsymbol{x})]\dot{\boldsymbol{x}} \tag{3.88}$$

Note the physical significance of Eq. (3.88). Instead of just feeding back the $\dot{\boldsymbol{x}}$ vector, as would be done traditionally in velocity feedback (proportional damping), a momentum type quantity is fed back instead. Even though $[P^{\eta}]$ is a constant scalar in this expression, the $[M(\boldsymbol{x})]$ term acts as a state dependent feedback gain matrix. While the control law in Eq. (3.88) is fairly simple and straight forward to implement, the use of the more general control law in Eq. (3.87) requires the instantaneous eigenvectors and eigenvalues of the current system mass matrix $[M]$. One method to find these eigenfactors without resorting to resolving a complete eigenvector/eigenvalue problem is to use the elegant Jacobi method as outlined in Appendix A. Given a current eigenfactor estimate from the previous control update, by implementing one "Jacobi sweep" these estimates are replaced with the current values. Using the more general control law in Eq. (3.87) it would be possible to assign separate weights to each mode of the dynamical response and have them decay at different, well defined rates.

As a comparison, the traditional method of constructing output velocity feedback

laws would result in a control law of the type

$$\boldsymbol{Q} = V_x(x) - [P^{\dot{x}}]\dot{\boldsymbol{x}} \tag{3.89}$$

where $[P^{\dot{x}}]$ is the velocity feedback gain matrix. To study stability of the classical feedback law in Eq.(3.89), let us write the kinetic energy in the classical form and use it as a system Lyapunov function.

$$T = \frac{1}{2}\dot{\boldsymbol{x}}^T[M]\dot{\boldsymbol{x}} \tag{3.90}$$

The first time derivative of $T$ is

$$\dot{T} = \dot{\boldsymbol{x}}^T[M]\ddot{x} + \frac{1}{2}\dot{\boldsymbol{x}}^T[\dot{M}]\dot{\boldsymbol{x}} \tag{3.91}$$

Using Eq. (3.12) this is reduced to

$$\dot{T} = \dot{\boldsymbol{x}}^T\left(\boldsymbol{Q} - V_x - \frac{1}{2}[\dot{M}]\dot{\boldsymbol{x}} + \frac{1}{2}\dot{\boldsymbol{x}}^T[M_{\boldsymbol{x}}]\dot{\boldsymbol{x}}\right) \tag{3.92}$$

which is then expanded to

$$\dot{T} = \dot{\boldsymbol{x}}^T(\boldsymbol{Q} - V_x) - \frac{1}{2}\dot{\boldsymbol{x}}^T[\dot{M}]\dot{\boldsymbol{x}} + \frac{1}{2}\sum_i \dot{\boldsymbol{x}}_i(\dot{\boldsymbol{x}}^T[M_{x_i}]\dot{\boldsymbol{x}}) \tag{3.93}$$

Using the identity in Eq. (3.79) this is simplified to the usual work/energy power expression

$$\dot{T} = \dot{\boldsymbol{x}}^T(\boldsymbol{Q} - V_x) \tag{3.94}$$

The traditional velocity feedback control law in Eq. (3.89) then yields the following negative definite expression

$$\dot{T} = -\dot{\boldsymbol{x}}^T[P^{\dot{x}}]\dot{\boldsymbol{x}} \tag{3.95}$$

where $[P^{\dot{x}}]$ is a positive definite matrix. Therefore the classical velocity feedback

control law is also globally asymptotically stabilizing.

### *3.6.2 Exponential Convergence*

Both velocity feedback control laws in Eqs. (3.87) and (3.89) are shown to be globally asymptotically stabilizing. Now their convergence rates will be studied. First, assume that $P^\eta$ is a scalar quantity. Then the time derivative of $T$ can be written as

$$\dot{T} = -P^\eta \boldsymbol{\eta}^T \boldsymbol{\eta} \tag{3.96}$$

Using Eq. (3.19) this is rewritten as

$$\dot{T} = -2P^\eta T \tag{3.97}$$

This simple first order differential equation can be solved explicitly to yield

$$T(t) = e^{-2P^\eta t}\ T(0) \tag{3.98}$$

Therefore, for any choice of positive $P^\eta$, the total system kinetic energy will decay exponentially at a well defined rate.

To show exponential convergence for the case where $[P^\eta]$ is a fully populated positive definite matrix, we make use of the Rayleigh-Ritz inequality[53,54]

$$\lambda_{min}^{P^\eta} \boldsymbol{\eta}^T \boldsymbol{\eta} \leq \boldsymbol{\eta}^T [P^\eta] \boldsymbol{\eta} \leq \lambda_{max}^{P^\eta} \boldsymbol{\eta}^T \boldsymbol{\eta} \tag{3.99}$$

This inequality allows $\dot{T}$ to be upwardly bounded by

$$\dot{T} = -\boldsymbol{\eta}^T P^\eta \boldsymbol{\eta} \leq -\lambda_{min}^{P^\eta} \boldsymbol{\eta}^T \boldsymbol{\eta} \tag{3.100}$$

Using Eq. (3.19) again, the following inequality for $\dot{T}$ is obtained.

$$\dot{T} \leq -2\lambda_{min}^{P^\eta} T \tag{3.101}$$

Note that in this more general case the kinetic energy is upwardly bounded by a exponentially decaying curve at a rate of $-2\lambda_{min}^{P^\eta}$.

$$T(t) \leq T(0)e^{-2\lambda_{min}^{P^\eta}t} \tag{3.102}$$

Here the kinetic energy decay rate cannot be easily determined for the entire maneuver. However, as time $t$ grows sufficiently large it will approach the decay rate of the smallest eigenvalue $\lambda_{min}^{P^\eta}$.

Proving exponential stability for the feedback control law in Eq. (3.89) is more difficult. Let $\lambda_{min}^{P^{\dot{x}}}$ be the smallest eigenvalue of $[P^{\dot{x}}]$, then using Eq. (3.95) and (3.99) the following inequality must hold.

$$\dot{T} \leq -\lambda_{min}^{P^{\dot{x}}}\dot{\boldsymbol{x}}^T\dot{\boldsymbol{x}} \tag{3.103}$$

Let $\lambda_{max}^{M}$ be the largest eigenvalue of $M$. If

$$\lambda_{min}^{P^{\dot{x}}} \geq \lambda_{max}^{M} \tag{3.104}$$

is true, then the above inequality can be expanded to

$$\dot{T} \leq -\lambda_{min}^{P^{\dot{x}}}\dot{\boldsymbol{x}}^T\dot{\boldsymbol{x}} \leq -\lambda_{max}^{M}\dot{\boldsymbol{x}}^T\dot{\boldsymbol{x}} \leq -\dot{\boldsymbol{x}}^T M\dot{\boldsymbol{x}} \tag{3.105}$$

Using Eq. (3.90), the kinetic energy derivative will be upwards limited by

$$\dot{T} \leq -2T \tag{3.106}$$

Note that with this control law, exponential stability is only shown for a sufficiently large set of $[P^{\dot{x}}]$ eigenvalues. Also, the convergence rate cannot be determined easily from the above analysis. Numerical analysis shows that the condition in Eq. (3.104) is very conservative. It is observed that an exponential closed loop stability guarantee, for a general class of nonlinear systems, is a very significant result. The velocity

feedback control law in Eq. (3.89) is found to be exponentially stabilizing in the endgame even if the condition in Eq. (3.104) is violated. Therefore the EQV feedback control law in Eq. (3.87) or (3.88) provides a very simple and straight forward way of controlling the exponential convergence of the velocity state.

The concept of feeding back a generalized momentum quantity instead of a configuration velocity coordinate to achieve controlled exponential stability can easily be applied to the rigid body attitude control problem discussed earlier. Instead of using the traditional control torque $\boldsymbol{u}$ defined in Eq. (3.76), let the feedback gain $P^{\omega}$ be a scalar quantity and define the torque $\boldsymbol{u}$ instead as

$$\boldsymbol{u} = -P^{\omega}[I]\boldsymbol{\omega} \tag{3.107}$$

The kinetic energy derivative in Eq. (3.75) can now be written using Eq. (3.74) as

$$\dot{T} = -P^{\omega}\boldsymbol{\omega}^{T}[I]\boldsymbol{\omega} = -2P^{\omega}T \tag{3.108}$$

With this slight modification, a globally asymptotically stabilizing feedback control law is made exponentially stabilizing, providing a straight forward way to control the kinetic energy decay rate.

### *3.6.3 Numerical Results*

To compare the performance of the feedback control laws in Eqs. (3.87) and (3.89), they are applied to a three-link manipulator system and a tumbling rigid body. In each simulation the goal of the control law is to bring the system to rest by dissipating all initial kinetic energy. For all cases, we consider only damping (velocity) feedback. The position feedback term would be identical for both control laws and is therefore uninteresting for this analysis.

#### 3.6.3.1 Three-Link Manipulator System

The rigid three-link manipulator system is shown in Figure 3.8. Each link has some initial rotational velocity and the goal of this example is to bring all the links to rest at an arbitrary orientation. The numerical integration is performed with a fourth order Runge-Kutta method with an integration step size of 0.005 seconds and a simulation duration of 15 seconds.

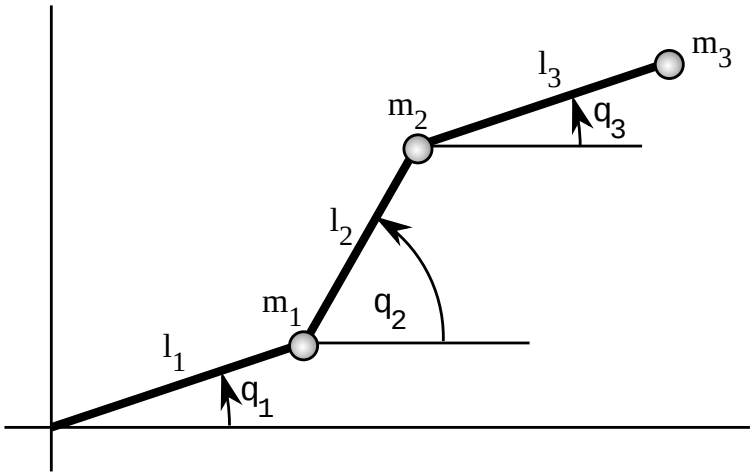


**Fig. 3.8:** Three-Link Manipulator System Layout

Choosing the inertial polar angles as generalized coordinates the state vector is $\boldsymbol{x} = (\theta_1, \theta_2, \theta_3)^T$, then the system mass matrix is

$$[M(\boldsymbol{x})] = \begin{bmatrix} (m_1+m_2+m_3)l_1^2 & (m_2+m_3)l_1 l_2 \cos\theta_{21} & m_3 l_1 l_3 \cos\theta_{31} \\ (m_2+m_3)l_1 l_2 \cos\theta_{21} & (m_2+m_3)l_2^2 & m_3 l_2 l_3 \cos\theta_{32} \\ m_3 l_1 l_3 \cos\theta_{31} & m_3 l_2 l_3 \cos\theta_{32} & m_3 l_3^2 \end{bmatrix} \tag{3.109}$$

where the shorthand notation $\theta_{ij} = \theta_i - \theta_j$ is used. The feedback gains are chosen to be scalars are held constant for each control law. To perform a reasonable comparison, the feedback gain magnitude for each control law is selected such that the maximum absolute control effort encountered is equal. The first simulation is performed with

very large initial link rotations as is shown in Table 3.3.

**Table 3.3:** Parameters of Large Initial Motion Study

| Parameter | Value | Units |
|---|---|---|
| $l_1$ | 1 | m |
| $l_2$ | 1 | m |
| $l_3$ | 1 | m |
| $m_1$ | 1.0 | kg |
| $m_2$ | 1.0 | kg |
| $m_3$ | 1.0 | kg |
| $P^{\eta}$ | 0.7 | kg-m$^2$/sec |
| $P^{\dot{x}}$ | 1.0 | kg-m$^2$/sec |
| $\boldsymbol{x}(t_0)$ | $[-90\ 30\ 0]$ | deg |
| $\dot{\boldsymbol{x}}(t_0)$ | $[93\ -110\ -73]$ | deg/sec |

The magnitude of the control vector $\boldsymbol{Q}$ is shown in Figure 3.9(i). With this tuning of the gains, both control laws encounter a maximum control effort of about 3.5 N-m. The $\boldsymbol{\eta}$ control law magnitude starts to be reduced linearly (on the base 10 logarithmic scale) after only about 1 second of maneuver time. A linear logarithmic decay rate indicates an exponentially decaying quantity. The $\dot{\boldsymbol{x}}$ control law does not start to decay linearly on this scale until after 6 seconds into the maneuver. After an initial hump, the control magnitude associated with $\dot{\boldsymbol{x}}$ control drops off quickly at first and then decays relatively slowly. The kinetic energy $T$ is decreased by about one order of magnitude every 5 seconds. The $\boldsymbol{\eta}$ control maintains a relatively large control effort for the initial portion of the maneuver where about 90% of the kinetic energy is being canceled. After this the $\boldsymbol{\eta}$ control effort drops off at a much faster than the $\dot{\boldsymbol{x}}$ control effort. The kinetic energy $T$ is decreased by one order of magnitude about every 1.5 seconds.

The only way for the $\dot{\boldsymbol{x}}$ control law to have a similar (three times as fast energy dissipation) performance as the $\boldsymbol{\eta}$ control law would be to make $P^{\dot{x}}$ time dependent, or introduce piecewise constant gain scheduling. The draw-back of feedback gain

scheduling is that it makes the overall control law much more complicated. The $\boldsymbol{\eta}$ control law effectively performs some feedback gain scheduling implicitly; as is seen in Eq. (3.88), the control law can be viewed as a variable-gain feedback on $\dot{\boldsymbol{x}}$.

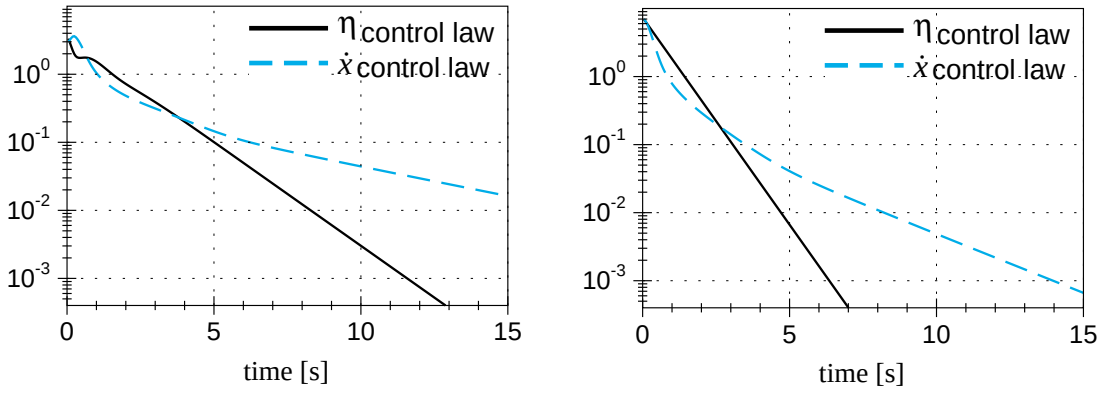


(i) Control Vector Magnitude $|\boldsymbol{Q}|$ (ii) Kinetic Energy $T$

**Fig. 3.9:** Large Initial Rotation Stabilization

The kinetic energy provides a scalar measure of the total system "error motion" and is plotted on a base 10 logarithmic scale in Figure 3.9(ii). As predicted, the $\boldsymbol{\eta}$ control law has an exponentially decaying kinetic energy since the corresponding curve in Figure 3.9(ii) is completely linear. The kinetic energy for the $\dot{\boldsymbol{x}}$ control law starts to decay linearly on the logarithmic scale after a few seconds, whereas the kinetic energy for the $\boldsymbol{\eta}$ control is linear from the outset. These example results demonstrate very clearly that for a given maximum control effort, the $\boldsymbol{\eta}$ control law outperforms the constant gain $\dot{\boldsymbol{x}}$ control law by having a much larger final decay rate. While these results are for a particular example, the exponential convergence proof of the previous section is general. Therefore this pattern is expected to be representative.

The second simulation is performed with only the third link having an initial rotational motion as evident in Table 3.4. If left uncontrolled, then the coupled system dynamics would distribute the kinetic energy of the third link into the other

**Table 3.4:** Parameters of Isolated Initial Motion Study

| Parameter | Value | Units |
|---|---|---|
| $l_1$ | 1 | m |
| $l_2$ | 1 | m |
| $l_3$ | 1 | m |
| $m_1$ | 1.0 | kg |
| $m_2$ | 1.0 | kg |
| $m_3$ | 1.0 | kg |
| $P^{\eta}$ | 0.72 | kg-m$^2$/sec |
| $P^{\dot{x}}$ | 1.0 | kg-m$^2$/sec |
| $\boldsymbol{x}(t_0)$ | [−90 30 0] | deg |
| $\dot{\boldsymbol{x}}(t_0)$ | [0.0 0.0 10] | deg/sec |

two links and very quickly all three links would be rotating. Furthermore, one can expect a general closed loop response to have significant energy in all links shortly after release. The closed loop time history of the $\dot{\boldsymbol{x}}$ vector components for both control laws (corresponding to proportional $\dot{\boldsymbol{x}}$ and $\boldsymbol{\eta}$ damping) are shown in Figure 3.10(i). With the $\dot{\boldsymbol{x}}$ feedback control law, coupling causes all three links to start to rotate and then the control law brings them all to rest together. The $\boldsymbol{\eta}$ feedback control law performs quite differently. The later keeps the motion of the first two links very close two zero while exponentially reducing the initial 10 degrees/second motion of the third link. This pleasant surprise is qualitatively a nonlinear analog of "independent modal space control" popular for linear structural dynamical systems.[28,55] In effect, this feedback control law is able to approximately decouple the rotation of each link and bring each *individually* to zero. Note that no explicit gain scheduling had to be performed with this control law to achieve this effect.

The magnitudes of the control efforts involved are shown in Figure 3.10(ii). Both feedback control laws have the same maximum control effort. As is shown in the previous simulation, again the $\boldsymbol{\eta}$ control effort remains larger than the $\dot{\boldsymbol{x}}$ control effort until about 90% of the kinetic energy is canceled. After this the $\boldsymbol{\eta}$ control effort

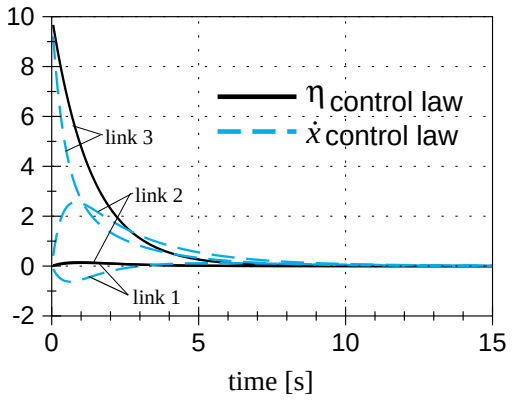


(i) $\dot{\boldsymbol{x}}$ Vector Components

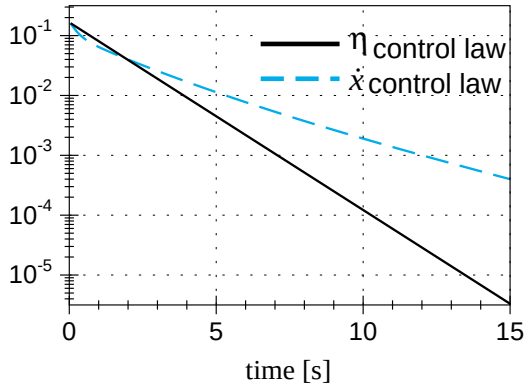


(ii) Control Vector Magnitude $|\boldsymbol{Q}|$

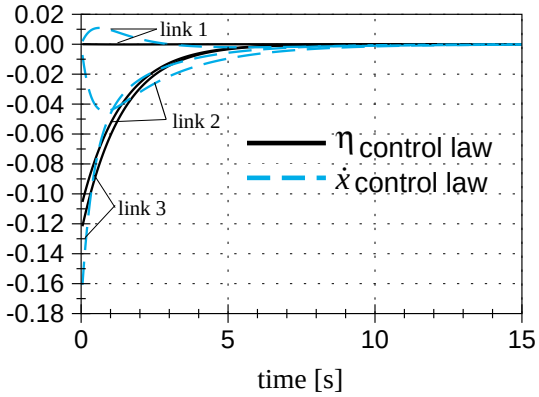


(iii) Control Vector $\boldsymbol{Q}$ Components

**Fig. 3.10:** Isolated Initial Rotation Stabilization

keeps on decreasing in an exponential manner while the $\dot{\boldsymbol{x}}$ control effort also decreases exponentially, but at a much slower rate.

The vector components of the control effort are shown in Figure 3.10(iii). As expected, all three control components are active for the $\dot{\boldsymbol{x}}$ feedback law. The $\boldsymbol{\eta}$ control however keeps the first control component near zero while only using the second and third control component. They decay at the same exponential rate and differ in magnitude such that the motion of the third link is stopped while not starting any motion in the second link.

#### 3.6.3.2 Tumbling Rigid Body

The second system studied is a tumbling rigid body. For this case, the body has a very large initial angular velocity and the feedback control law is designed to drive the kinetic energy to zero. The Euler equations of motion for a rigid body are given in Eq. (3.73). A fourth order Runge-Kutta integration method is used to perform the numerical simulation with an integration step size of 0.1 seconds. Total maneuver time is 15 seconds.

**Table 3.5:** Parameters of Rigid Body Stabilization Study

| Parameter | Value | Units |
|---|---|---|
| $[I]$ | $\begin{bmatrix} 10 & 5 & 3 \\ 5 & 7 & 4 \\ 3 & 4 & 5 \end{bmatrix}$ | kg-m$^2$ |
| $P^{\eta}$ | 0.33 | kg-m$^2$/sec |
| $P^{\dot{x}}$ | 2.0 | kg-m$^2$/sec |
| $\dot{\boldsymbol{\omega}}(t_0)$ | $[90 \quad -70 \quad 50]$ | deg/sec |

The two control laws given in Eqs. (3.76) and (3.107) are compared here. The simulation parameters used are given in Table 3.5. The angular velocity feedback is chosen to be a scalar in both cases. The classical feedback law is

$$\boldsymbol{u} = -P^{\dot{x}}\dot{\boldsymbol{x}} = -P_1\boldsymbol{\omega} \tag{3.110}$$

where the $\boldsymbol{\eta}$ feedback law reduces to

$$\boldsymbol{u} = -P^{\eta}[I]\boldsymbol{\omega} \tag{3.111}$$

which is simply momentum feedback in this case since $P^{\eta}$ is a scalar. In an effort to make a fair comparison of the control laws, the feedback gains are chosen such that the maximum encountered control effort for both control laws is the same, for the given initial conditions. The magnitudes of each control law are shown in Figure 3.11(i).

Both control laws have their gains tuned consistently so that they result in the same maximum control effort at the beginning of the simulation. As is observed in the three-link manipulator simulations, the $\boldsymbol{\eta}$ control law retains a larger control effort during the first segment of the maneuver and decays to a lower value than the $\dot{\boldsymbol{x}}$ control effort.

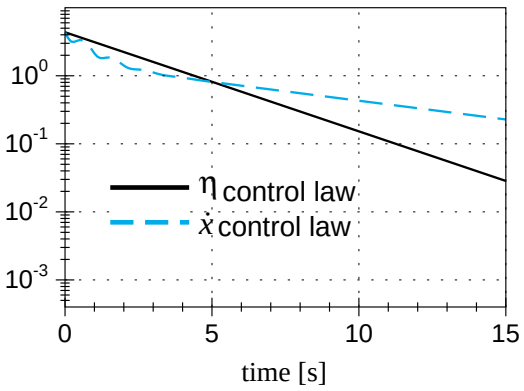


(i) Control Torque Magnitudes $|\boldsymbol{u}|$

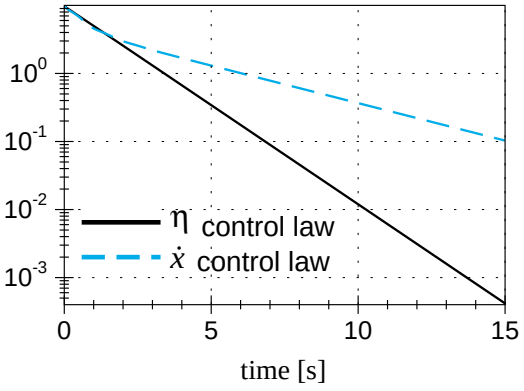


(ii) Kinetic Energy Decay

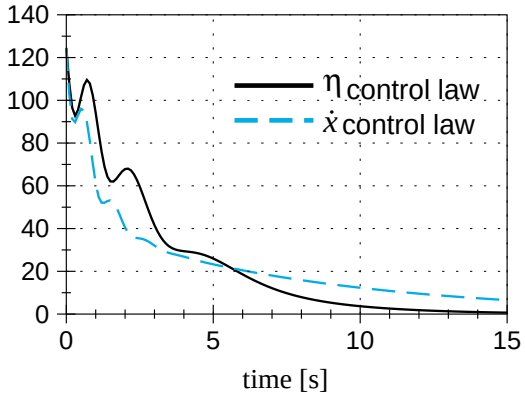


(iii) Body Ang. Vel. Magnitudes $|\boldsymbol{\omega}|$

**Fig. 3.11:** Rigid Body Stabilization

The system kinetic energy is plotted in Figure 3.11(ii). As anticipated, the $\boldsymbol{\eta}$ control law causes the system kinetic energy to decay exponentially at the prescribed rate. The $\dot{\boldsymbol{x}}$ control law appears to cause the kinetic energy to decay exponentially

only after about 2 seconds into the maneuver at a slower rate. At the maneuver end, the residual kinetic energy of the $\boldsymbol{\eta}$ control law simulations is over two orders of magnitude less then the $\dot{\boldsymbol{x}}$ control law simulation.

The corresponding body angular velocity vector magnitudes are plotted in Figure 3.11(iii). Note that even though the kinetic energy of the $\boldsymbol{\eta}$ control law simulation is typically equal or lower than the $\dot{\boldsymbol{x}}$ control law kinetic energy, the angular velocity magnitude of the $\boldsymbol{\eta}$ control law is only smaller than the $\dot{\boldsymbol{x}}$ angular velocity magnitude after about six seconds into the simulation.

One reason why the $\boldsymbol{\eta}$ control law performs so much better in these simulations than the $\dot{\boldsymbol{x}}$ control law is that the inertia matrix is fully populated. If we repeat these simulations with the inertia matrix $[I]$ near-diagonal, then there would be virtually no inertia matrix coupling to compensate for. In these cases the $\boldsymbol{\eta}$ and $\dot{\boldsymbol{x}}$ control laws perform almost identically.

# CHAPTER IV

## VARIABLE SPEED CONTROL MOMENT GYROSCOPES*

Instead of using thrusters to perform precise spacecraft attitude maneuvers, typically control moment gyros (CMGs) or reaction wheels (RWs) are used. These electric motor driver reaction devices have two main advantages over thrusters: (1) They can deliver smooth and easy to throttle torques guaranteed not to spill over into translational accelerations, and (2) Being driven by electricity, their lifetime on orbit is indefinitely long. A single-gimbal CMG contains a wheel spinning at a constant rate. To exert a torque onto the spacecraft, this wheel is gimbaled or rotated about a fixed axis.[16,18,57] The rotation axis and rotation angle are referred to as the gimbal axis and gimbal angle respectively. A separate feedback control loop is used to spin up the rotor to the required spin rate and maintain it. The primary advantage of a CMG device is that a small gimbal torque input is required to produce a relatively large effective torque output on the spacecraft. This makes CMGs very popular devices for reorienting large space structures such as the space station. The drawback of the single-gimbal CMGs is that their control laws can be fairly complex and that such CMG systems encounter certain singular gimbal angle configurations. At these singular configurations the CMG cluster is unable to produce the required torque exactly, or any torque at all if the required torque is orthogonal to the plane of allowable torques associated with the singular configuration. Several papers deal with this issue and present various approaches to solutions.[16,18,57,58] However, even with singularity robust steering laws or when various singularity avoidance strategies are applied, the actual torque produced by the CMG cluster is not equal to the

*Portions of this chapter were published in Reference 56. Authors retained the copyright.

required torque when maneuvering in the proximity of a singularity. The resulting motion may be stable, but the resulting attitude deviations can be highly undesirable in some applications where precise tracking is required.

Reaction wheels, on the other hand, have a wheel spinning about a body fixed axis whose spin speed is variable. Torques are produced on the spacecraft by accelerating or decelerating the reaction wheels.[5,25] RW systems don't have singular configurations and typically have simpler control laws than CMG clusters. Drawbacks to the reaction wheels include a relatively small effective torque being produced on the spacecraft and the possibility of reaction wheel saturation (exceeding maximum wheel speeds). To exert a given torque onto a spacecraft, reaction wheels typically require more energy than CMGs.

Variable Speed Control Moment Gyroscopes (VSCMGs) combine positive features of both the single-gimbal CMGs and the RWs. The spinning disk can be rotated or gimbaled about a single body fixed axis, while the disk spin rate is also free to be controlled.[19] This adds an extra degree of control to the classical single-gimbal CMG device. Note that adding this variable speed feature would not require the single-gimbal CMG to be completely reengineered. These devices already have a separate feedback loop that maintains a constant spin rate. However, it is anticipated that the torque motor controlling the RW spin rate would need to be stronger and, of course, the constant speed RW feedback law be abandoned in favor of a new control law. With this extra control flexibility, singular configurations (in the classical CMG sense) will not be present. Since CMGs are known to be more efficient energy wise than RWs, the VSCMG steering law should ideally act like the conventional CMG steering law away from a single-gimbal CMG singular configurations. As a single-gimbal CMG singularity is approached, the VSCMGs should begin to use the RW modes to avoid the excessive torques that would normally occur and ensure that the applied torque of

the VSCMG cluster is exactly equal to the required torque. This strategy will allow for precise steering without path deviations near the conventional CMG singularities because the actual commanded torque will be generated at all times. Both a gimbal velocity based and an gimbal acceleration based steering law are presented in this chapter. Lyapunov analysis is used to guarantee global asymptotic stability of the feedback control law.

As is shown by Vadali et. al in Ref.,[20] for a given spacecraft maneuver there are preferred sets of initial gimbal angles. Starting the reorientation with these preferred angles it is possible to not encounter any singularities during the maneuver and the corresponding trajectory deviations at all. To reconfigure the internal gimbals to the preferred set of angles, CMG *null motion* is typically used. Null motion arises due to redundancy. For example, a cluster of 4 CMGs has four gimbal angular rates (or accelerations) to generate the 3 torque components. Null motion refers to the special set of gimbal motions which yield a net effective torque of zero. To avoid applying any torque on the spacecraft, the internal CMG cluster momentum vector cannot change during this reconfiguration. This fact greatly limits the sets of angles between which the CMGs can be reconfigured. Using VSCMGs, however, more degrees of control are present to perform an infinite set of null motions. The VSCMG null motion equations of motion and their use to vary either the gimbal angles or the RW spin speed, or both together, is discussed below. Of particular interest will be the energy consumption required to augment the conventional CMG null motion with RW modes to perform more general reconfigurations.

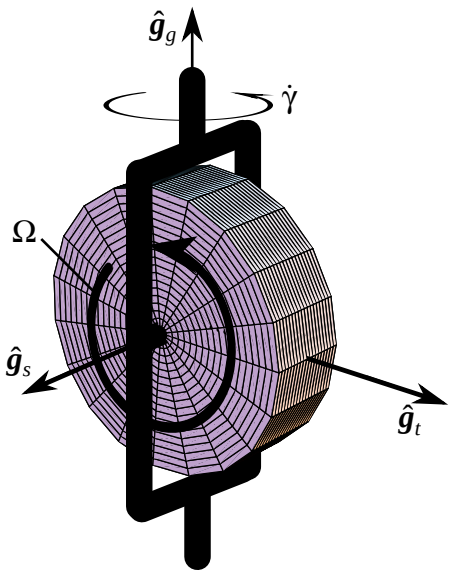


**Fig. 4.1:** Illustration of a Variable Speed Control Moment Gyroscope

## 4.1 Equations of Motion

### *4.1.1 Spacecraft with Single VSCMG*

To simplify the development and notation, the rotational equations of motion are first derived for the case where only one VSCMG is attached to a rigid spacecraft. Afterwards, the result is expanded to incorporate a system of $N$ VSCMGs. Let $\mathcal{G}$ denote the gimbal reference frame whose orientation is given by the triad of unit vectors $\{\hat{\boldsymbol{g}}_s, \hat{\boldsymbol{g}}_t, \hat{\boldsymbol{g}}_g\}$ as shown in Figure 4.1. The vector components of the unit vectors $\hat{\boldsymbol{g}}_i$ are assumed to be given in the spacecraft reference frame $\mathcal{B}$. Note that since the VSCMG gimbal axis $\hat{\boldsymbol{g}}_g$ is fixed relative to $\mathcal{B}$, only the orientation of the spin axis $\hat{\boldsymbol{g}}_s$ and the transverse axis $\hat{\boldsymbol{g}}_t$ will be time varying as seen from the $\mathcal{B}$ frame. Given an initial gimbal angle $\gamma_0$, the spin and transverse axis at a gimbal angle $\gamma(t)$ are given by

$$\hat{\boldsymbol{g}}_s(t) = \cos(\gamma(t) - \gamma_0)\,\hat{\boldsymbol{g}}_s(t_0) + \sin(\gamma(t) - \gamma_0)\,\hat{\boldsymbol{g}}_t(t_0) \tag{4.1}$$

$$\hat{\boldsymbol{g}}_t(t) = -\sin(\gamma(t) - \gamma_0)\,\hat{\boldsymbol{g}}_s(t_0) + \cos(\gamma(t) - \gamma_0)\,\hat{\boldsymbol{g}}_t(t_0) \tag{4.2}$$

The spin rate of the VSCMG about $\hat{\boldsymbol{g}}_s$ is denoted by $\Omega$. The angular velocity vector of the $\mathcal{G}$ frame relative to the $\mathcal{B}$ frame is

$$\boldsymbol{\omega}_{\mathcal{G}/\mathcal{B}} = \dot{\gamma}\hat{\boldsymbol{g}}_g \tag{4.3}$$

The angular velocity vector of the reaction wheel frame $\mathcal{W}$ relative to the gimbal frame $\mathcal{G}$ is

$$\boldsymbol{\omega}_{\mathcal{W}/\mathcal{G}} = \Omega\hat{\boldsymbol{g}}_s \tag{4.4}$$

To indicate in which reference frame vector or matrix components are taken, a superscript letter is added before the vector or matrix name. Since the $\mathcal{G}$ frame unit axes are aligned with the principal gimbal frame axes, the gimbal frame inertia matrix $[I_G]$ expressed in the $\mathcal{G}$ frame is the constant diagonal matrix.

$$[I_G] = {}^{\mathcal{G}}[I_G] = {}^{\mathcal{G}}\begin{bmatrix} I_{G_s} & 0 & 0 \\ 0 & I_{G_t} & 0 \\ 0 & 0 & I_{G_g} \end{bmatrix} \tag{4.5}$$

where $I_{G_s}$, $I_{G_t}$ and $I_{G_g}$ are the gimbal frame inertias about the corresponding spin, transverse and gimbal axes. The reaction wheel inertia about the same axes are denoted by $I_{W_s}$ and $I_{W_t}$.

$$[I_W] = {}^{\mathcal{W}}[I_W] = {}^{\mathcal{W}}\begin{bmatrix} I_{W_s} & 0 & 0 \\ 0 & I_{W_t} & 0 \\ 0 & 0 & I_{W_t} \end{bmatrix} \tag{4.6}$$

Note that since the disk is symmetric about the $\hat{\boldsymbol{g}}_s$ axis, it follows that ${}^{\mathcal{W}}[I_W] = {}^{\mathcal{G}}[I_W]$. In practice $I_{W_s}$ is typically much larger than any of the other gimbal frame or RW inertias. In this development the RW and gimbal frame inertias are not combined

initially into one overall VSCMG inertia matrix; rather, they are retained as separate entities until a later stage of the developments. This will allow for a precise accounting for the two sets of physical motor torques that drive the RWs and the CMGs.

The $\mathcal{G}$ frame orientation is related to the $\mathcal{B}$ frame orientation through the direction cosine matrix $[BG]$ which is expressed in terms of the gimbal frame unit direction vectors as

$$[BG] = [\hat{\boldsymbol{g}}_s \, \hat{\boldsymbol{g}}_t \, \hat{\boldsymbol{g}}_g] \tag{4.7}$$

In Eq. (4.7) the $\hat{\boldsymbol{g}}_i$ vector components are taken in the $\mathcal{B}$ frame. The rotation matrix $[BG]$ maps a vector with components taken in the $\mathcal{G}$ frame into a vector with components in the $\mathcal{B}$ frame. The constant diagonal inertia matrices ${}^{\mathcal{G}}[I_G]$ and ${}^{\mathcal{G}}[I_W]$ are expressed with components taken in the $\mathcal{B}$ frame as the following time varying matrices[59,60]

$${}^{\mathcal{B}}[I_G] = [BG]\,{}^{\mathcal{G}}[I_G]\,[BG]^T = I_{G_s}\hat{\boldsymbol{g}}_s\hat{\boldsymbol{g}}_s^T + I_{G_t}\hat{\boldsymbol{g}}_t\hat{\boldsymbol{g}}_t^T + I_{G_g}\hat{\boldsymbol{g}}_g\hat{\boldsymbol{g}}_g^T \tag{4.8}$$

$${}^{\mathcal{B}}[I_W] = [BG]\,{}^{\mathcal{G}}[I_W]\,[BG]^T = I_{W_s}\hat{\boldsymbol{g}}_s\hat{\boldsymbol{g}}_s^T + I_{W_t}\hat{\boldsymbol{g}}_t\hat{\boldsymbol{g}}_t^T + I_{W_t}\hat{\boldsymbol{g}}_g\hat{\boldsymbol{g}}_g^T \tag{4.9}$$

The total angular momentum of the spacecraft and the VSCMG about the spacecraft center of mass is given by

$$\boldsymbol{H} = \boldsymbol{H}_B + \boldsymbol{H}_G + \boldsymbol{H}_W \tag{4.10}$$

where $\boldsymbol{H}_B$ is the angular momentum of the spacecraft, $\boldsymbol{H}_G$ is the angular momentum of the gimbal frame and $\boldsymbol{H}_W$ is the angular momentum of the RW. Let $\mathcal{N}$ be an inertial reference frame and $\boldsymbol{\omega}_{\mathcal{B}/\mathcal{N}}$ be the relative angular velocity vector, then $\boldsymbol{H}_B$ is written as

$$\boldsymbol{H}_B = [I_s]\boldsymbol{\omega}_{\mathcal{B}/\mathcal{N}} \tag{4.11}$$

The matrix $[I_s]$ contains the spacecraft inertias and the VSCMG inertia components due to the fact that the VSCMG center of mass is not located at the spacecraft center of mass. While the matrix equation of Eq. (4.11) could be written in any reference frame, we choose the $\mathcal{B}$ frame because $[I_s] = {}^{\mathcal{B}}[I_s]$ is a constant matrix when expressed in the $\mathcal{B}$ frame. The gimbal frame angular momentum $\boldsymbol{H}_G$ is given by

$$\boldsymbol{H}_G = [I_G]\boldsymbol{\omega}_{\mathcal{G}/\mathcal{N}} \tag{4.12}$$

where $\boldsymbol{\omega}_{\mathcal{G}/\mathcal{N}} = \boldsymbol{\omega}_{\mathcal{G}/\mathcal{B}} + \boldsymbol{\omega}_{\mathcal{B}/\mathcal{N}}$. Using Eqs. (4.3), (4.5) and (4.8) this is rewritten as

$$\boldsymbol{H}_G = \left(I_{G_s}\hat{\boldsymbol{g}}_s\hat{\boldsymbol{g}}_s^T + I_{G_t}\hat{\boldsymbol{g}}_t\hat{\boldsymbol{g}}_t^T + I_{G_g}\hat{\boldsymbol{g}}_g\hat{\boldsymbol{g}}_g^T\right)\boldsymbol{\omega}_{\mathcal{B}/\mathcal{N}} + I_{G_g}\dot{\gamma}\hat{\boldsymbol{g}}_g \tag{4.13}$$

To simplify the following notation, let the variables $\omega_s$, $\omega_t$ and $\omega_g$ be the projection of $\boldsymbol{\omega}_{\mathcal{B}/\mathcal{N}}$ onto the $\mathcal{G}$ frame unit axes.

$$\omega_s = \hat{\boldsymbol{g}}_s^T\boldsymbol{\omega}_{\mathcal{B}/\mathcal{N}} \tag{4.14a}$$

$$\omega_t = \hat{\boldsymbol{g}}_t^T\boldsymbol{\omega}_{\mathcal{B}/\mathcal{N}} \tag{4.14b}$$

$$\omega_g = \hat{\boldsymbol{g}}_g^T\boldsymbol{\omega}_{\mathcal{B}/\mathcal{N}} \tag{4.14c}$$

The angular momentum $\boldsymbol{H}_G$ is then written as

$$\boldsymbol{H}_G = I_{G_s}\omega_s\hat{\boldsymbol{g}}_s + I_{G_t}\omega_t\hat{\boldsymbol{g}}_t + I_{G_g}\left(\omega_g + \dot{\gamma}\right)\hat{\boldsymbol{g}}_g \tag{4.15}$$

Upon substituting the $\mathcal{B}$ components of $\{\hat{\boldsymbol{g}}_s, \hat{\boldsymbol{g}}_t, \hat{\boldsymbol{g}}_g\}$, Eq. (4.15) provides $\boldsymbol{H}_G$ in the $\mathcal{B}$ frame, if desired. The RW angular momentum $\boldsymbol{H}_W$ is given by

$$\boldsymbol{H}_W = [I_W]\boldsymbol{\omega}_{\mathcal{W}/\mathcal{N}} \tag{4.16}$$

where $\boldsymbol{\omega}_{\mathcal{W}/\mathcal{N}} = \boldsymbol{\omega}_{\mathcal{W}/\mathcal{G}} + \boldsymbol{\omega}_{\mathcal{G}/\mathcal{B}} + \boldsymbol{\omega}_{\mathcal{B}/\mathcal{N}}$ and the components of all vectors are implicitly taken in the $\mathcal{B}$ frame in Eq. (4.16). Using analogous definitions as for $\boldsymbol{H}_G$, $\boldsymbol{H}_W$ is

rewritten as

$$\boldsymbol{H}_W = I_{W_s}\left(\omega_s + \Omega\right)\hat{\boldsymbol{g}}_s + I_{W_t}\omega_t\hat{\boldsymbol{g}}_t + I_{W_t}\left(\omega_g + \dot{\gamma}\right)\hat{\boldsymbol{g}}_g \tag{4.17}$$

To simplify the notation from here on, let us use the short hand notation $\boldsymbol{\omega} = \boldsymbol{\omega}_{\mathcal{B}/\mathcal{N}}$. In some developments it will be convenient to express $\boldsymbol{\omega}$ in the $\mathcal{G}$ frame as

$${}^{\mathcal{G}}\boldsymbol{\omega} = \omega_s\hat{\boldsymbol{g}}_s + \omega_t\hat{\boldsymbol{g}}_t + \omega_g\hat{\boldsymbol{g}}_g \tag{4.18}$$

To denote that a vector $\boldsymbol{x}$ is being differentiated relative to a reference frame $\mathcal{A}$, the following notation is used.

$$\frac{{}^{\mathcal{A}}d}{dt}\left(\boldsymbol{x}\right)$$

Indicating an inertial time derivatives of a vector $\boldsymbol{x}$ will be abbreviated as

$$\frac{{}^{\mathcal{N}}d}{dt}\left(\boldsymbol{x}\right) \equiv \dot{\boldsymbol{x}}$$

The equations of motion of a system of rigid bodies follow from Euler's equation[59,60]

$$\dot{\boldsymbol{H}} = \boldsymbol{L} \tag{4.19}$$

if all moments are taken about the configuration's center of mass. The vector $\boldsymbol{L}$ represents the sum of all the external torques experienced by the spacecraft.

To find the inertial derivatives of $\boldsymbol{H}_G$ and $\boldsymbol{H}_W$, the inertial derivatives of the vectors $\{\hat{\boldsymbol{g}}_s, \hat{\boldsymbol{g}}_t, \hat{\boldsymbol{g}}_g\}$ are required. Using the transport theorem we find[61]

$$\dot{\hat{\boldsymbol{g}}}_s = \frac{{}^{\mathcal{B}}d}{dt}\left(\hat{\boldsymbol{g}}_s\right) + \boldsymbol{\omega}\times\hat{\boldsymbol{g}}_s = \left(\dot{\gamma} + \omega_g\right)\hat{\boldsymbol{g}}_t - \omega_t\hat{\boldsymbol{g}}_g \tag{4.20a}$$

$$\dot{\hat{\boldsymbol{g}}}_t = \frac{{}^{\mathcal{B}}d}{dt}\left(\hat{\boldsymbol{g}}_t\right) + \boldsymbol{\omega}\times\hat{\boldsymbol{g}}_t = -\left(\dot{\gamma} + \omega_g\right)\hat{\boldsymbol{g}}_s + \omega_s\hat{\boldsymbol{g}}_g \tag{4.20b}$$

$$\dot{\hat{\boldsymbol{g}}}_g = \frac{{}^{\mathcal{B}}d}{dt}\left(\hat{\boldsymbol{g}}_g\right) + \boldsymbol{\omega}\times\hat{\boldsymbol{g}}_g = \omega_t\hat{\boldsymbol{g}}_s - \omega_s\hat{\boldsymbol{g}}_t \tag{4.20c}$$

since the $\mathcal{B}$ frame derivatives are simply

$$\frac{^{\mathcal{B}}d}{dt}\left(\hat{\boldsymbol{g}}_s\right) = \dot{\gamma}\hat{\boldsymbol{g}}_t \tag{4.21}$$

$$\frac{^{\mathcal{B}}d}{dt}\left(\hat{\boldsymbol{g}}_t\right) = -\dot{\gamma}\hat{\boldsymbol{g}}_s \tag{4.22}$$

$$\frac{^{\mathcal{B}}d}{dt}\left(\hat{\boldsymbol{g}}_g\right) = 0 \tag{4.23}$$

as can be verified through Eqs. (4.1) and (4.2). The inertial derivatives of the $\mathcal{G}$ frame body angular velocity components are

$$\dot{\omega}_s = \dot{\hat{\boldsymbol{g}}}_s^T\boldsymbol{\omega} + \hat{\boldsymbol{g}}_s^T\dot{\boldsymbol{\omega}} = \dot{\gamma}\omega_t + \hat{\boldsymbol{g}}_s^T\dot{\boldsymbol{\omega}} \tag{4.24a}$$

$$\dot{\omega}_t = \dot{\hat{\boldsymbol{g}}}_t^T\boldsymbol{\omega} + \hat{\boldsymbol{g}}_t^T\dot{\boldsymbol{\omega}} = -\dot{\gamma}\omega_s + \hat{\boldsymbol{g}}_t^T\dot{\boldsymbol{\omega}} \tag{4.24b}$$

$$\dot{\omega}_g = \dot{\hat{\boldsymbol{g}}}_g^T\boldsymbol{\omega} + \hat{\boldsymbol{g}}_g^T\dot{\boldsymbol{\omega}} = \hat{\boldsymbol{g}}_g^T\dot{\boldsymbol{\omega}} \tag{4.24c}$$

Using these definitions, the inertial derivative of $\boldsymbol{H}_W$ is expressed as

$$\begin{aligned}\dot{\boldsymbol{H}}_W = {} & \hat{\boldsymbol{g}}_s I_{W_s}\left(\dot{\Omega} + \hat{\boldsymbol{g}}_s^T\dot{\boldsymbol{\omega}} + \dot{\gamma}\omega_t\right) \\ & + \hat{\boldsymbol{g}}_t\left(I_{W_s}\dot{\gamma}\omega_s + I_{W_t}\hat{\boldsymbol{g}}_t^T\dot{\boldsymbol{\omega}} + \left(I_{W_s} - I_{W_t}\right)\omega_s\omega_g + I_{W_s}\Omega\left(\dot{\gamma} + \omega_g\right)\right) \\ & + \hat{\boldsymbol{g}}_g\left(I_{W_t}\hat{\boldsymbol{g}}_g^T\left(\dot{\boldsymbol{\omega}} + \ddot{\gamma}\right) + \left(I_{W_t} - I_{W_s}\right)\omega_s\omega_t + I_{W_s}\Omega\omega_t\right)\end{aligned} \tag{4.25}$$

Let $\boldsymbol{L}_W$ be the torque the gimbal frame exerts on the RW. Isolating the dynamics of the RW, Euler's equation states that $\dot{\boldsymbol{H}}_W = \boldsymbol{L}_W$. The torque components in the $\hat{\boldsymbol{g}}_t$ and $\hat{\boldsymbol{g}}_g$ direction are constraint reactions produced by the gimbal frame itself. However, the torque component $u_s$ about the $\hat{\boldsymbol{g}}_s$ axis is produced by the RW torque motor. Therefore, from Eq. (4.25) the spin control torque $u_s$ is given by

$$u_s = I_{W_s}\left(\dot{\Omega} + \hat{\boldsymbol{g}}_s^T\dot{\boldsymbol{\omega}} + \dot{\gamma}\omega_t\right) \tag{4.26}$$

After differentiating Eq. (4.15) and making use of the definitions in Eqs. (4.20)

and (4.24), $\dot{\boldsymbol{H}}_G$ is expressed as

$$\begin{aligned}\dot{\boldsymbol{H}}_G = & \hat{\boldsymbol{g}}_s \left( \left( I_{G_s} - I_{G_t} + I_{G_g} \right) \dot{\gamma} \omega_t + I_{G_s} \hat{\boldsymbol{g}}_s^T \dot{\boldsymbol{\omega}} + \left( I_{G_g} - I_{G_t} \right) \omega_t \omega_g \right) \\ & + \hat{\boldsymbol{g}}_t \left( \left( I_{G_s} - I_{G_t} - I_{G_g} \right) \dot{\gamma} \omega_s + I_{G_t} \hat{\boldsymbol{g}}_t^T \dot{\boldsymbol{\omega}} + \left( I_{G_s} - I_{G_t} \right) \omega_s \omega_g \right) \\ & + \hat{\boldsymbol{g}}_g \left( I_{G_g} \left( \hat{\boldsymbol{g}}_g^T \dot{\boldsymbol{\omega}} + \ddot{\gamma} \right) + \left( I_{G_t} - I_{G_s} \right) \omega_s \omega_t \right)\end{aligned} \tag{4.27}$$

From here on it is convenient to combine the inertia matrices of the RW and the gimbal frame into one VSCMG inertia matrix $[J]$ as

$$[J] = [I_G] + [I_W] = \begin{matrix} \\ \mathcal{G} \end{matrix} \begin{bmatrix} J_s & 0 & 0 \\ 0 & J_t & 0 \\ 0 & 0 & J_g \end{bmatrix} \tag{4.28}$$

Let $\boldsymbol{L}_G$ be the torque vector that the combined RW and CMG system exerts onto the spacecraft, then Euler's equation states that $\dot{\boldsymbol{H}}_G + \dot{\boldsymbol{H}}_W = \boldsymbol{L}_G$. The $\boldsymbol{L}_G$ torque component about the $\hat{\boldsymbol{g}}_g$ axis is produced by the gimbal torque motor. Adding Eqs. (4.25) and (4.27) and making use of the definition in Eq. (4.28), the gimbal torque $u_g$ is then expressed as

$$u_g = J_g \left( \hat{\boldsymbol{g}}_g^T \dot{\boldsymbol{\omega}} + \ddot{\gamma} \right) - \left( J_s - J_t \right) \omega_s \omega_t - I_{W_s} \Omega \omega_t \tag{4.29}$$

The inertial derivative of $\boldsymbol{H}_B$ is simply

$$\dot{\boldsymbol{H}}_B = [I_s] \dot{\boldsymbol{\omega}} + [\tilde{\boldsymbol{\omega}}][I_s] \boldsymbol{\omega} \tag{4.30}$$

To further simplify the equations of motions, the total spacecraft inertia matrix $[I]$ is defined as

$$[I] = [I_s] + [J] \tag{4.31}$$

Substituting Eqs. (4.25), (4.27) and (4.30) back into Eq. (4.19) and making use of the definition in Eq. (4.31), the equations of motion for a rigid spacecraft containing

one VSCMG are

$$\begin{aligned}[I]\dot{\boldsymbol{\omega}} = -[\tilde{\boldsymbol{\omega}}][I]\boldsymbol{\omega} &- \hat{\boldsymbol{g}}_s \left( J_s \dot{\gamma} \omega_t + I_{W_s} \dot{\Omega} - (J_t - J_g)\, \omega_t \dot{\gamma} \right) \\ &- \hat{\boldsymbol{g}}_t \left( (J_s \omega_s + I_{W_s} \Omega)\, \dot{\gamma} - (J_t + J_g)\, \omega_s \dot{\gamma} + I_{W_s} \Omega \omega_g \right) \\ &- \hat{\boldsymbol{g}}_g \left( J_g \ddot{\gamma} - I_{W_s} \Omega \omega_t \right) + \boldsymbol{L}\end{aligned} \tag{4.32}$$

where the identity

$$[\tilde{\boldsymbol{\omega}}][J]\boldsymbol{\omega} = (J_g - J_t)\, \omega_t \omega_g \hat{\boldsymbol{g}}_s + (J_s - J_g)\, \omega_s \omega_g \hat{\boldsymbol{g}}_t + (J_t - J_s)\, \omega_s \omega_s \hat{\boldsymbol{g}}_g \tag{4.33}$$

is used to combine terms into the $[\tilde{\boldsymbol{\omega}}][I]\boldsymbol{\omega}$ expression. From here on the common assumption will be made that $J_s \approx I_{W_s}$, i.e,. that the gimbal frame inertia $I_{G_s}$ about the spin axis is negligible as regards to it's contribution to spin momentum. The corresponding equations of motion are simplified to

$$\begin{aligned}[I]\dot{\boldsymbol{\omega}} = -[\tilde{\boldsymbol{\omega}}][I]\boldsymbol{\omega} &- \hat{\boldsymbol{g}}_s \left( J_s \left( \dot{\Omega} + \dot{\gamma} \omega_t \right) - (J_t - J_g)\, \omega_t \dot{\gamma} \right) \\ &- \hat{\boldsymbol{g}}_t \left( J_s\, (\omega_s + \Omega)\, \dot{\gamma} - (J_t + J_g)\, \omega_s \dot{\gamma} + J_s \Omega \omega_g \right) \\ &- \hat{\boldsymbol{g}}_g \left( J_g \ddot{\gamma} - J_s \Omega \omega_t \right) + \boldsymbol{L}\end{aligned} \tag{4.34}$$

An alternate path to derive these equations of motion is shown in Appendix B where Lagrangian methods are used.

### *4.1.2 Spacecraft with Multiple VSCMGs*

To obtain the equations of motion of a rigid spacecraft with several VSCMGs attached, the effects of each $\dot{\boldsymbol{H}}_G$ and $\dot{\boldsymbol{H}}_W$ are added up. To simplify notation, let us define the following useful matrices. The $3\text{x}N$ matrices $[G_s]$, $[G_t]$ and $[G_g]$ contain the spin, transverse and gimbal unit direction vectors of each VSCMG gimbal frame.

$$[G_s] = [\hat{\boldsymbol{g}}_{s_1} \cdots \hat{\boldsymbol{g}}_{s_N}] \tag{4.35a}$$

$$[G_t] = [\hat{\boldsymbol{g}}_{t_1} \cdots \hat{\boldsymbol{g}}_{t_N}] \tag{4.35b}$$

$$[G_g] = [\hat{\boldsymbol{g}}_{g_1} \cdots \hat{\boldsymbol{g}}_{g_N}] \tag{4.35c}$$

The total spacecraft inertia matrix is expressed as

$$[I] = [I_s] + \sum_{i=1}^{N} [J_i] = [I_s] + \sum_{i=1}^{N} \left[ J_{s_i} \hat{\boldsymbol{g}}_{s_i} \hat{\boldsymbol{g}}_{s_i}^T + J_{t_i} \hat{\boldsymbol{g}}_{t_i} \hat{\boldsymbol{g}}_{t_i}^T + J_{g_i} \hat{\boldsymbol{g}}_{g_i} \hat{\boldsymbol{g}}_{g_i}^T \right] \tag{4.36}$$

The effective torque quantities $\tau_{s_i}$, $\tau_{t_i}$ and $\tau_{g_i}$ are defined as

$$\boldsymbol{\tau}_s = \begin{bmatrix} J_{s_1} \left( \dot{\Omega}_1 + \dot{\gamma}_1 \omega_{t_1} \right) - \left( J_{t_1} - J_{g_1} \right) \omega_{t_1} \dot{\gamma}_1 \\ \vdots \\ J_{s_N} \left( \dot{\Omega}_N + \dot{\gamma}_N \omega_{t_N} \right) - \left( J_{t_N} - J_{g_N} \right) \omega_{t_N} \dot{\gamma}_N \end{bmatrix} \tag{4.37a}$$

$$\boldsymbol{\tau}_t = \begin{bmatrix} J_{s_1} \left( \Omega_1 + \omega_{s_1} \right) \dot{\gamma}_1 - \left( J_{t_1} + J_{g_1} \right) \omega_{s_1} \dot{\gamma}_1 + J_{s_1} \Omega_1 \omega_{g_1} \\ \vdots \\ J_{s_N} \left( \Omega_N + \omega_{s_N} \right) \dot{\gamma}_N - \left( J_{t_N} + J_{g_N} \right) \omega_{s_N} \dot{\gamma}_N + J_{s_N} \Omega_N \omega_{g_N} \end{bmatrix} \tag{4.37b}$$

$$\boldsymbol{\tau}_g = \begin{bmatrix} J_{g_1} \ddot{\gamma}_1 - J_{s_1} \Omega_1 \omega_{t_1} \\ \vdots \\ J_{g_N} \ddot{\gamma}_N - J_{s_N} \Omega_N \omega_{t_N} \end{bmatrix} \tag{4.37c}$$

The rotational equations of motion for a rigid body containing $N$ VSCMGs is then written compactly as[56]

$$[I]\dot{\boldsymbol{\omega}} = -[\tilde{\boldsymbol{\omega}}][I]\boldsymbol{\omega} - [G_s]\boldsymbol{\tau}_s - [G_t]\boldsymbol{\tau}_t - [G_g]\boldsymbol{\tau}_g + \boldsymbol{L} \tag{4.38}$$

The rotational kinetic energy $T$ of a rigid spacecraft with $N$ VSCMGs is given by

$$T = \frac{1}{2}\boldsymbol{\omega}^T [I_s]\boldsymbol{\omega} + \frac{1}{2} \sum_{i=1}^{N} \left[ J_{s_i} \left( \Omega_i + \omega_{s_i} \right)^2 + J_{t_i} \omega_{t_i}^2 + J_{g_i} \left( \omega_{g_i} + \dot{\gamma}_i \right)^2 \right] \tag{4.39}$$

The kinetic energy rate, also known as the work rate, is found after differentiating Eq. (4.39) and performing some lengthy algebra to be

$$\dot{T} = \sum_{i=1}^{N} \left( \dot{\gamma}_i u_{g_i} + \Omega_i u_{s_i} \right) + \boldsymbol{\omega}^T \boldsymbol{L} \tag{4.40}$$

This energy rate for this system of rigid bodies was apriori known from the Work-Energy-Rate principle[62] and is thus a validation of the presented equations of motion. Also, checking the kinetic energy time history is a convenient way to check the accuracy of the numerical simulations.

## 4.2 Feedback Control Law

### *4.2.1 Tracking a Reference Trajectory*

The following feedback law is derived using Lyapunov control theory. Given some initial angular velocity and attitude measure, the goal of the control law is to track some reference trajectory. The MRP attitude vector $\boldsymbol{\sigma}$ is measured relative to the reference frame $\mathcal{R}$ attitude. Let $\boldsymbol{\omega}_r$ be the reference frame body angular velocity, then the instantaneous angular velocity error vector $\delta\boldsymbol{\omega}$ is given by

$$\delta\boldsymbol{\omega} = \boldsymbol{\omega} - \boldsymbol{\omega}_r \tag{4.41}$$

The angular acceleration error vector is found by taking an inertial derivative of Eq. (4.41).

$$\delta\dot{\boldsymbol{\omega}} = \dot{\boldsymbol{\omega}} - \dot{\boldsymbol{\omega}}_r \tag{4.42}$$

where the vectors $\boldsymbol{\omega}_r$ and $\dot{\boldsymbol{\omega}}_r$ are assumed to be known. Note that the vector components of $\boldsymbol{\omega}_r$ and $\dot{\boldsymbol{\omega}}_r$ are typically given in the $\mathcal{R}$ frame. To actually compute Eqs. (4.41) and (4.42) the components of these vectors need to be projected into the body frame $\mathcal{B}$ through

$$^{\mathcal{B}}\boldsymbol{\omega}_r = [BR]^{\mathcal{R}}\boldsymbol{\omega}_r \tag{4.43}$$

$$^{\mathcal{B}}\dot{\boldsymbol{\omega}}_r = [BR]^{\mathcal{R}}\dot{\boldsymbol{\omega}}_r \tag{4.44}$$

In designing the control law it is assumed that estimates of $\boldsymbol{\omega}$, $\boldsymbol{\sigma}$, $\Omega_i$ and $\gamma_i$

are available. The following Lyapunov function $V$ is a positive definite, radially unbounded measure of the total system state error relative to the target state $\delta\boldsymbol{\omega} = \boldsymbol{\sigma} = 0$ where $K$ is a scalar attitude feedback gain.[25]

$$V(\delta\boldsymbol{\omega}, \boldsymbol{\sigma}) = \frac{1}{2}\delta\boldsymbol{\omega}^T[I]\delta\boldsymbol{\omega} + 2K\log\left(1 + \boldsymbol{\sigma}^T\boldsymbol{\sigma}\right) \tag{4.45}$$

The MRP attitude error measure containing the logarithm function is the same as was introduced in Chapter II. Note that all the body angular velocity vectors and inertia matrices have components taken in the $\mathcal{B}$ frame in Eq. (4.45). Using Eq. (2.66), the time derivative of the Lyapunov function $V$ is given by

$$\dot{V} = \delta\boldsymbol{\omega}^T\left([I]\delta\dot{\boldsymbol{\omega}} + \frac{1}{2}\frac{{}^{\mathcal{B}}d}{dt}[I]\delta\boldsymbol{\omega} + K\boldsymbol{\sigma}\right) \tag{4.46}$$

Since the Lyapunov function $V$ is a scalar quantity, taking its derivative involves simply the derivatives of the scalar components. Since the inertia matrix $[I]$ has components taken in the $\mathcal{B}$ frame, it's derivative here is taken as seen by the $\mathcal{B}$ frame only. The derivatives of the body angular velocity vectors are written in Eq. (4.46) as $\dot{\boldsymbol{\omega}}$ since differentiation of $\boldsymbol{\omega} = \boldsymbol{\omega}_{\mathcal{B}/\mathcal{N}}$ is $\mathcal{B}$ and $\mathcal{N}$ is identical due to the truth:

$$\dot{\boldsymbol{\omega}} = \frac{{}^{\mathcal{N}}d}{dt}\boldsymbol{\omega} = \frac{{}^{\mathcal{B}}d}{dt}\boldsymbol{\omega} + \boldsymbol{\omega}\times\boldsymbol{\omega} = \frac{{}^{\mathcal{B}}d}{dt}\boldsymbol{\omega} \tag{4.47}$$

Using the inertia matrix definition in Eq. (4.36) and the $\mathcal{B}$ frame derivatives in Eq. (4.21), the $\mathcal{B}$ frame derivative of $[I]$ is

$$\frac{{}^{\mathcal{B}}d}{dt}[I] = \sum_{i=1}^{N}\gamma_i\left(J_{s_i} - J_{t_i}\right)\left(\hat{\boldsymbol{g}}_{s_i}\hat{\boldsymbol{g}}_{t_i}^T + \hat{\boldsymbol{g}}_{t_i}^T\hat{\boldsymbol{g}}_{s_i}^T\right) \tag{4.48}$$

Lyapunov stability theory requires that $\dot{V}$ be negative semi-definite to guarantee stability. Let $[P]$ be a positive definite angular velocity feedback gain matrix, then $\dot{V}$

is set to

$$\dot{V} = -\delta\boldsymbol{\omega}^T[P]\delta\boldsymbol{\omega} \tag{4.49}$$

which, when combined with Eq. (4.46), leads to the stability constraint:

$$[I]\delta\dot{\boldsymbol{\omega}} = -K\boldsymbol{\sigma} - [P]\delta\boldsymbol{\omega} - \frac{1}{2}\frac{^{\mathcal{B}}d}{dt}[I]\delta\boldsymbol{\omega} \tag{4.50}$$

After substituting Eqs. (4.38) and (4.48) into Eq. (4.51), the following stability constraint is obtained.

$$\begin{aligned}\sum_{i=1}^{N} J_{s_i}\dot{\Omega}_i\hat{\boldsymbol{g}}_{s_i} + \sum_{i=1}^{N} J_{g_i}\ddot{\gamma}_i\hat{\boldsymbol{g}}_{g_i} + \sum_{i=1}^{N}\dot{\gamma}_i\Bigg(J_{s_i}\Omega_i\hat{\boldsymbol{g}}_{t_i} + \frac{1}{2}\left(J_{s_i}-J_{t_i}\right)\left(\omega_{t_i}\hat{\boldsymbol{g}}_{s_i}+\omega_{s_i}\hat{\boldsymbol{g}}_{t_i}\right)\\ + J_{g_i}\left(\omega_{t_i}\hat{\boldsymbol{g}}_{s_i}-\omega_{s_i}\hat{\boldsymbol{g}}_{t_i}\right) + \frac{1}{2}\left(J_{s_i}-J_{t_i}\right)\left(\hat{\boldsymbol{g}}_{s_i}\hat{\boldsymbol{g}}_{t_i}^T\boldsymbol{\omega}_r + \hat{\boldsymbol{g}}_{t_i}\hat{\boldsymbol{g}}_{s_i}^T\boldsymbol{\omega}_r\right)\Bigg)\\ = K\boldsymbol{\sigma} + [P]\delta\boldsymbol{\omega} + \boldsymbol{L} - [\tilde{\boldsymbol{\omega}}][I]\boldsymbol{\omega} - [I]\dot{\boldsymbol{\omega}}_r - \sum_{i=1}^{N} J_{s_i}\left(\Omega_i\omega_{g_i}\hat{\boldsymbol{g}}_{t_i} - \Omega_i\omega_{t_i}\hat{\boldsymbol{g}}_{g_i}\right)\end{aligned} \tag{4.51}$$

To express this condition in a more compact and useable form, let us define the following $3$x$N$ matrices, where all components are taken in $\mathcal{B}$:

$$[D_0] = [\cdots \hat{\boldsymbol{g}}_{s_i} J_{s_i} \cdots] \tag{4.52a}$$

$$[D_1] = [\cdots J_{s_i}\left(\left(\Omega_i + \frac{1}{2}\omega_{s_i}\right)\hat{\boldsymbol{g}}_{t_i} + \frac{1}{2}\omega_{t_i}\hat{\boldsymbol{g}}_{s_i}\right)\cdots] \tag{4.52b}$$

$$[D_2] = [\cdots \frac{1}{2}J_{t_i}\left(\omega_{t_i}\hat{\boldsymbol{g}}_{s_i} + \omega_{s_i}\hat{\boldsymbol{g}}_{t_i}\right)\cdots] \tag{4.52c}$$

$$[D_3] = [\cdots J_{g_i}\left(\omega_{t_i}\hat{\boldsymbol{g}}_{s_i} - \omega_{s_i}\hat{\boldsymbol{g}}_{t_i}\right)\cdots] \tag{4.52d}$$

$$[D_4] = [\cdots \frac{1}{2}\left(J_{s_i} - J_{t_i}\right)\left(\hat{\boldsymbol{g}}_{s_i}\hat{\boldsymbol{g}}_{t_i}^T\boldsymbol{\omega}_r + \hat{\boldsymbol{g}}_{t_i}\hat{\boldsymbol{g}}_{s_i}^T\boldsymbol{\omega}_r\right)\cdots] \tag{4.52e}$$

$$[B] = [\cdots \hat{\boldsymbol{g}}_{g_i} J_{g_i} \cdots] \tag{4.52f}$$

Let $\dot{\boldsymbol{\Omega}}$, $\ddot{\boldsymbol{\gamma}}$ and $\dot{\boldsymbol{\gamma}}$ be $N$x$1$ vectors whose $i$-th element contains the respective VSCMG angular velocity or acceleration or RW spin rate. The stability constraint in Eq. (4.51)

then is expressed as

$$[D_0]\dot{\boldsymbol{\Omega}} + [B]\ddot{\boldsymbol{\gamma}} + [D]\dot{\boldsymbol{\gamma}} = \boldsymbol{L}_r \tag{4.53}$$

where $[D] = ([D_1] - [D_2] + [D_3] + [D_4])$ and the required torque vector $\boldsymbol{L}_r$ is defined to be

$$\boldsymbol{L}_r = K\boldsymbol{\sigma} + [P]\delta\boldsymbol{\omega} + \boldsymbol{L} - [\tilde{\boldsymbol{\omega}}][I]\boldsymbol{\omega} - [I]\dot{\boldsymbol{\omega}}_r - \sum_{i=1}^{N} J_{s_i}\left(\Omega_i\omega_{g_i}\hat{\boldsymbol{g}}_{t_i} - \Omega_i\omega_{t_i}\hat{\boldsymbol{g}}_{g_i}\right) \tag{4.54}$$

Dropping the $[D_0]\dot{\boldsymbol{\Omega}}$ term, the standard single-gimbal CMG stability constraint is retrieved as it is developed in Ref. 16. Note that the formulation presented here does not require any matrix multiplications of sparse matrices and the effects of the individual VSCMG inertia terms are immediately evident. The condition in Eq. (4.53) only guarantees global stability in the sense of Lyapunov for the states $\delta\boldsymbol{\omega}$ and $\boldsymbol{\sigma}$, since $\dot{V}$ in Eq. (4.49) is only negative semi-definite, not negative definite. However, Eq. (4.49) does show that $\delta\boldsymbol{\omega} \to 0$ as time goes to infinity. To prove that the stability constraint in Eq. (4.53) guarantees asymptotic stability of all states including $\boldsymbol{\sigma}$, the higher time derivatives of $V$ must be investigated. A sufficient condition to guarantee asymptotic stability is that the first nonzero higher-order derivative of $V$, evaluated on the set of states such that $\dot{V}$ is zero, must be of odd order and be negative definite.[28,30,31] For this dynamical system $\dot{V}$ is zero when $\delta\boldsymbol{\omega}$ is zero. Differentiating Eq. (4.49) the second derivative of $V$ is

$$\frac{d^2}{d^2t}V = -2\delta\boldsymbol{\omega}^T[P]\delta\dot{\boldsymbol{\omega}} \tag{4.55}$$

which is zero on the set of states where $\delta\boldsymbol{\omega}$ is zero. Differentiating again the third derivative of $V$ is

$$\frac{d^3}{d^3t}V = -2\delta\dot{\boldsymbol{\omega}}^T[P]\delta\dot{\boldsymbol{\omega}} - 2\delta\boldsymbol{\omega}^T[P]\delta\ddot{\boldsymbol{\omega}} \tag{4.56}$$

Substituting Eq. (4.50) and setting $\delta\boldsymbol{\omega} = 0$, the third derivative of the Lyapunov function is expressed as

$$\frac{d^3}{d^3t}V = -K^2\boldsymbol{\sigma}^T\left([I]^{-1}\right)^T[P][I]^{-1}\boldsymbol{\sigma} \tag{4.57}$$

which is a negative definite quantity since both $[I]$ and $[P]$ are positive definite matrices. Therefore the stability constraint in Eq. (4.53) does guarantee global asymptotic stability.

### *4.2.2 Regulator Problem*

If the desired spacecraft trajectory is a stationary attitude, then the reference body angular velocity vector $\boldsymbol{\omega}_r$ is zero. For these rest-to-rest or motion-to-rest type maneuvers the feedback control law in Eq. (4.54) can be greatly simplified. Let the MRP attitude vector $\boldsymbol{\sigma}$ be measured relative to the desired final attitude. Since the final angular velocity is supposed to be zero, the Lyapunov function $V$ is defined as

$$V = \frac{1}{2}\boldsymbol{\omega}^T[I]\boldsymbol{\omega} + 2K\log\left(1 + \boldsymbol{\sigma}^T\boldsymbol{\sigma}\right) \tag{4.58}$$

where $K$ is a scalar attitude feedback gain. It's time derivative is given by

$$\dot{V} = \boldsymbol{\omega}^T\left([I]\dot{\boldsymbol{\omega}} + \frac{1}{2}\frac{\mathcal{B}d}{dt}[I]\boldsymbol{\omega} + K\boldsymbol{\sigma}\right) \tag{4.59}$$

After substituting Eqs. (4.38) and (4.48) into Eq. (4.59) and rearranging some terms, $\dot{V}$ is expressed as

$$\begin{aligned}\dot{V} = -\boldsymbol{\omega}^T\Bigg([\tilde{\boldsymbol{\omega}}][I]\boldsymbol{\omega} + \sum_{i=1}^{N} J_{s_i}\dot{\Omega}_i\hat{\boldsymbol{g}}_{s_i} + \sum_{i=1}^{N} J_{g_i}\ddot{\gamma}_i\hat{\boldsymbol{g}}_{g_i} + \sum_{i=1}^{N} J_{s_i}\dot{\gamma}_i\left(\Omega_i + \frac{1}{2}\left(\omega_{t_i}\hat{\boldsymbol{g}}_{s_i} + \omega_{s_i}\hat{\boldsymbol{g}}_{t_i}\right)\right) \\ - K\boldsymbol{\sigma} - \boldsymbol{L} + \sum_{i=1}^{N} J_{s_i}\Omega\left(\omega_{g_i}\hat{\boldsymbol{g}}_{t_i} - \omega_{t_i}\hat{\boldsymbol{g}}_{g_i}\right) - \sum_{i=1}^{N} J_{t_i}\dot{\gamma}_i\frac{1}{2}\left(\omega_{s_i}\hat{\boldsymbol{g}}_{t_i} + \omega_{t_i}\hat{\boldsymbol{g}}_{s_i}\right) \\ + \sum_{i=1}^{N} J_{g_i}\dot{\gamma}_i\left(\omega_{t_i}\hat{\boldsymbol{g}}_{g_i} - \omega_{g_i}\hat{\boldsymbol{g}}_{t_i}\right)\Bigg)\end{aligned} \tag{4.60}$$

For this regulator problem several terms in Eq. (4.60) can be shown to be nonworking and are neglected in the resulting feedback control law. Setting $\dot{V} = -\boldsymbol{\omega}^T[P]\boldsymbol{\omega}$ and performing further algebraic manipulations, the simplified stability constraint for the regulator problem is found to be

$$\sum_{i=1}^{N} J_{s_i}\dot{\Omega}_i\hat{\boldsymbol{g}}_{s_i} + \sum_{i=1}^{N} J_{g_i}\ddot{\gamma}_i\hat{\boldsymbol{g}}_{g_i} + \sum_{i=1}^{N} J_{s_i}\dot{\gamma}_i\left(\Omega_i + \omega_{s_i}\right)\hat{\boldsymbol{g}}_{t_i} - \sum_{i=1}^{N} J_{t_i}\omega_{s_i}\dot{\gamma}_i\hat{\boldsymbol{g}}_{t_i} = K\boldsymbol{\sigma} + [P]\boldsymbol{\omega} + L = \boldsymbol{L}_r \quad (4.61)$$

Note that $\boldsymbol{L}_r$ defined in Eq. (4.61) is a simplified version of the one defined in Eq. (4.54). Making use of the $3 \times N$ matrices

$$[D_0] = [\cdots \hat{\boldsymbol{g}}_{s_i} J_{s_i} \cdots] \quad (4.62a)$$

$$[D_1] = [\cdots \hat{\boldsymbol{g}}_{t_i} J_{s_i}\left(\Omega_i + \omega_{s_i}\right) \cdots] \quad (4.62b)$$

$$[D_2] = [\cdots \hat{\boldsymbol{g}}_{t_i} J_{t_i}\omega_{s_i} \cdots] \quad (4.62c)$$

$$[B] = [\cdots \hat{\boldsymbol{g}}_{g_i} J_{g_i} \cdots] \quad (4.62d)$$

the stability constraint is written in the following compact form[56]

$$[D_0]\dot{\boldsymbol{\Omega}} + [B]\ddot{\boldsymbol{\gamma}} + [D]\dot{\boldsymbol{\gamma}} = \boldsymbol{L}_r \quad (4.63)$$

where $[D] = ([D_1] - [D_2])$. Note that the matrices $[D_0]$ and $[B]$ are the same as with the general feedback law. The matrices $[D_1]$ and $[D_2]$ are simplified and have columns which solely depend on the $\hat{\boldsymbol{g}}_{t_i}$ directions. The matrices $[D_3]$ and $[D_4]$ do not appear at all in this control law. Since this regulator control law is a specialization of the more general trajectory tracking control law, it too is globally asymptotically stabilizing.

### *4.2.3 Velocity Based Steering Law*

Note that the stability constraints in Eqs. (4.53) and (4.63) do not contain the physical control torques $u_{s_i}$ and $u_{g_i}$ explicitly. Instead only gimbal rates and accelerations and RW accelerations appear. This will lead to a steering law that determines the required time history of $\boldsymbol{\gamma}$ and $\boldsymbol{\Omega}$ such that Eq. (4.53) is satisfied. The reason for this is two fold. First, currently available CMGs typically require the gimbal rate vector $\dot{\boldsymbol{\gamma}}$ as the input, not the actual physical torque vector $\boldsymbol{u}_g$. Secondly, writing Eqs. (4.53) and (4.63) in terms of the torque vectors $\boldsymbol{u}_s$ and $\boldsymbol{u}_g$ and then solving for these would lead to a control law that is equivalent to solving Eq. (4.53) directly for the gimbal acceleration vector $\ddot{\boldsymbol{\gamma}}$. As has been pointed out in Ref. 16, this has been found to give a very undesirable control law with excessive gimbal rates. A physical reason for this is that such control laws provide the required control torque mainly through the $[B]\ddot{\boldsymbol{\gamma}}$ term. In this setup the CMGs are essentially being used as RWs and the potential torque amplification effect in not being exploited. Because CMG gimbal inertias $J_g$ are typically very small compared to their spin inertia $J_s$, the corresponding $[B]$ will also be very small which leads to very large $\ddot{\boldsymbol{\gamma}}$ vectors.

To take advantage of the potential torque amplification effect, most of the required control torque vector $\boldsymbol{L}_r$ should be produced by the larger gyroscopic coupling $[D]\dot{\boldsymbol{\gamma}}$ term. This is why classical CMG steering laws control primarily the $\dot{\boldsymbol{\gamma}}$ vector and not $\ddot{\boldsymbol{\gamma}}$. For the VSCMGs it is desirable to have the required torque $\boldsymbol{L}_r$ be produced by a combination of the $\dot{\boldsymbol{\Omega}}$ and $\dot{\boldsymbol{\gamma}}$ terms in Eqs. (4.53) and (4.63). To simplify the further development, let us assume that the final angular velocity is zero and the stability constraint in Eq. (4.63) only is used. However, the results are equally valid for the trajectory tracking control law. Paralleling the development of the classical single-gimbal CMG velocity steering laws, the terms containing the transverse and

gimbal VSCMG inertias are ignored at this level. Eq. (4.63) then becomes

$$[D_0]\dot{\boldsymbol{\Omega}} + [D_1]\dot{\boldsymbol{\gamma}} = \boldsymbol{L}_r \tag{4.64}$$

Comparing the $[D_1]$ matrix to that of standard CMG steering laws it is evident that an extra $\hat{\boldsymbol{g}}_t J_s \omega_s$ term is present in the VSCMG formulation. This term is neglected in the standard CMG formulation since it can be assumed that $\omega_s$ will typically be much smaller than $\Omega$. However, since for a VSCMG the RW spin speed $\Omega$ is variable, this assumption can no longer be justified and this term is retained in this formulation.

For notational convenience, we introduce the *2N*x*1* state vector $\boldsymbol{\eta}$

$$\boldsymbol{\eta} = \begin{bmatrix} \boldsymbol{\Omega} \\ \boldsymbol{\gamma} \end{bmatrix} \tag{4.65}$$

and the *3*x*2N* matrix $[Q]$

$$[Q] = \begin{bmatrix} D_0 \vdots D_1 \end{bmatrix} \tag{4.66}$$

Eq. (4.64) can then be written compactly as

$$[Q]\dot{\boldsymbol{\eta}} = \boldsymbol{L}_r \tag{4.67}$$

Note that each column of the $[D_0]$ matrix is a scalar multiple of the $\hat{\boldsymbol{g}}_{s_i}$ vectors, while each column of $[D_1]$ is a scalar multiple of the $\hat{\boldsymbol{g}}_{t_i}$ vectors. In the classical 4 single-gimbal CMG cluster, singular gimbal configurations are encountered whenever the rank of $[D_1]$ is less than 3. This occurs whenever the $\hat{\boldsymbol{g}}_{t_i}$ no longer span the three-dimensional space but form a plane. Any required torque which does not lie perfectly in this plane then cannot be generated exactly by the CMG cluster and the spacecraft would deviate from the desired trajectory. If the required control torque is perpendicular to this plane then the CMG cluster produces no effective torque

on the spacecraft. This singular behavior is illustrated in Figure 4.2 with two CMGs gimbaling to produce a constant torque vector $\boldsymbol{L}_r$. Since each CMG produces a torque about it's transverse axis, the two wheels must be gimbaled symmetrically and at the same rate to produce the indicated required torque vector $\boldsymbol{L}_r$. As both transverse axes rotate toward perpendicular orientations relative to $\boldsymbol{L}_r$, the associated gimbal rates become exceedingly large to produce the required torque. This is referred to as operating in the neighborhood of a singular configuration. If both transverse axes are perpendicular to $\boldsymbol{L}_r$, then no torque is produced (referred to as gimbal lock).

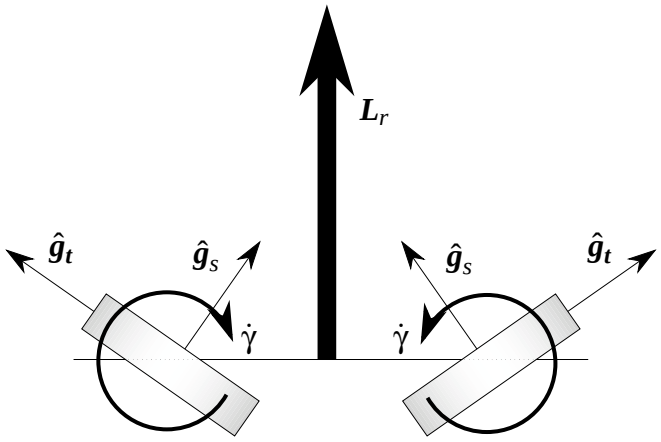


**Fig. 4.2:** Dual CMG System Encountering a Singularity

These singular configurations can never occur with a VSCMG since the rank of the $[Q]$ matrix will never be less than 3! Since the $\hat{\boldsymbol{g}}_{s_i}$ vectors are perpendicular to the $\hat{\boldsymbol{g}}_{t_i}$ vectors, even when all the transverse axes are coplanar, there will always be at least one spin axis that is not in this plane. Therefore the columns of $[Q]$ will *always* span the entire three-dimensional space as long as at least 2 or more VSCMGs are used with unique $\hat{\boldsymbol{g}}_{g_i}$ vectors. We mention, however, that while a singularity does not occur, this does not imply that other difficulties, such as wheel saturation, will not be encountered occasionally.

Since the $[Q]$ matrix will never be rank deficient, a minimum norm solution for

$\dot{\boldsymbol{\eta}}$ can be obtained using the standard Moore-Penrose inverse. However, since ideally the VSCMGs are to act like classical CMGs away from single-gimbal CMG singular configurations, a weighted pseudo inverse is recommended instead.[63] Let $[W]$ be a $2N$x$2N$ diagonal matrix

$$[W] = \begin{bmatrix} W_{s_1} & & & & & & 0 \\ & \ddots & & & & & \\ & & W_{s_N} & & & & \\ & & & W_{g_1} & & & \\ & & & & \ddots & & \\ 0 & & & & & & W_{g_N} \end{bmatrix} \tag{4.68}$$

where $W_{s_i}$ and $W_{g_i}$ are the weights associated with how nearly the VSCMGs are desired to locally perform like regular RWs or CMGs. Then the desired $\dot{\boldsymbol{\eta}}$ is[56]

$$\dot{\boldsymbol{\eta}} = \begin{bmatrix} \dot{\boldsymbol{\Omega}} \\ \dot{\boldsymbol{\gamma}} \end{bmatrix} = [W][Q]^T \left([Q][W][Q]^T\right)^{-1} \boldsymbol{L}_r \tag{4.69}$$

Note that there is no need here to introduce a modified pseudo-inverse as Nakamura and Hanafusa did in developing the singularity robustness steering law in Ref. 64. To achieve the desired VSCMG behavior, the weights are made dependent on the proximity to a single-gimbal CMG singularity. To measure this proximity the scalar factor $\delta$ is defined as

$$\delta = \det\left([D_1][D_1]^T\right) \tag{4.70}$$

Note that $[D_1]$ has units of angular momentum. With classical CMG configurations typically each CMG has the same spin axis angular momentum magnitude $h$, and this quantity can easily be factored out of $[D_1]$ to render $\delta$ non-dimensional. However, since VSCMGs will have time varying spin axis angular momentum magnitudes, one

would have to divide $[D_1]$ by a *nominal* spin axis angular momentum magnitude $\bar{h}$ to render $\delta$ non-dimensional.

$$\delta = \frac{1}{\bar{h}^2} \det\left([D_1][D_1]^T\right) \tag{4.71}$$

As the gimbals approach a singular CMG configuration this parameter $\delta$ will go to zero. The weights $W_{s_i}$ are then defined to be

$$W_{s_i} = W_{s_i}^0 e^{(-\mu\delta)} \tag{4.72}$$

where $W_{s_i}^0$ and $\mu$ are positive scalars to be chosen by the control designer. The gains $W_{g_i}$ are simply held constant. Away from CMG singularities this steering law will have very small weights on the RW mode and essentially perform like a classical single-gimbal CMG. As a singularity is approached, the steering law will start to use the RW mode to ensure that the gimbal rates do not become excessive and that the required control torque $\boldsymbol{L}_r$ is actually produced by the VSCMG cluster.

Two types of CMG singularities are commonly discussed. The simpler type of singularity is when the rank of the $[D_1]$ matrix drops below 3 which is indicated by $\delta$, defined in Eq. (4.70), approaching or becoming zero. The VSCMG velocity steering law in Eq. (4.69) handles temporary rank deficiencies very well. The required control torque is always produced correctly by making use of the addition control authority provided by the RW modes. Another type of singularity is when the required control torque is exactly perpendicular to the span of the transverse VSCMG axis (i.e. $\boldsymbol{L}_r$ is in the nullspace of $[D_1]$). Naturally, this is only possible whenever $\delta$ is zero. To measure how close the required torque $\boldsymbol{L}_r$ is to lying in the nullspace of $[D_1]$ the scalar orthogonality index $\mathcal{O}$ is used.[16]

$$\mathcal{O} = \frac{\boldsymbol{L}_r^T [D_1]^T [D_1] \boldsymbol{L}_r}{||\boldsymbol{L}_r||^2} \tag{4.73}$$

Similarly as with the non-dimensional singularity index $\delta$, the orthogonality index can be written in non-dimensional form as

$$\mathcal{O} = \frac{1}{\bar{h}^2} \frac{\boldsymbol{L}_r^T [D_1]^T [D_1] \boldsymbol{L}_r}{||\boldsymbol{L}_r||^2} \tag{4.74}$$

Whenever $\boldsymbol{L}_r$ becomes part of the nullspace of $[D_1]$, then $\mathcal{O}$ will tend towards zero. A classical single-gimbal CMG steering law demands a zero $\dot{\boldsymbol{\gamma}}$ vector with this type of singularity which "locks up" the gimbals produces no effective torque on the spacecraft. The VSCMG steering does not prevent the gimbals from being locked up in these singular orientations; however, the $\boldsymbol{L}_r$ vector is still being produced thanks to the RW mode of the VSCMGs. If a gimbal lock is actually achieved, then without any further changes, such as a change in the required $\boldsymbol{L}_r$, the VSCMG will simply continue the maneuvers acting like pure RWs. Running numerical simulations it was found that unless one starts the simulation in a pure gimbal lock situation, it was very unlikely for the VSCMG steering law to lock up the gimbals. Once a singularity is approached, the RWs are automatically spun up or down which also in return affects the gimbal orientation and lowers the likelihood of having the orthogonality index $\mathcal{O}$ go to zero. However, at present this VSCMG steering law makes no explicit effort to avoid these singular configurations during a maneuver. In essence, once the momentum symmetry (associated with CMG geometry and constant wheel speeds) is destroyed; by virtue of variable wheel speeds, the corresponding singular geometries are also eliminated.

### *4.2.4 Acceleration Based Steering Law*

The simplified formulation provided by the gimbal velocity based steering law in Eq. (4.69) is convenient to study and analyze the steering law. However, to provide a more realistic simulation, the transverse inertia need to be included also and $\ddot{\boldsymbol{\gamma}}$ needs

to be used as the actual control input. Having a gimbal angle acceleration expression will also allow for simulations that study the actual work done by the steering laws, and this is of obvious importance. If the transverse inertias are considered, then the stability constraint in Eq. (4.61) is given by

$$[D_0]\dot{\boldsymbol{\Omega}} + [B]\ddot{\boldsymbol{\gamma}} + [D]\dot{\boldsymbol{\gamma}} = \boldsymbol{L}_r \tag{4.75}$$

where $[D] = [D_1] + [D_2]$. The goal of the gimbal acceleration based steering law is to provide the same performance as the gimbal velocity based steering law. Let the vector $\dot{\boldsymbol{\eta}}_d$ be the desired $\dot{\boldsymbol{\Omega}}$ and $\dot{\boldsymbol{\gamma}}$ quantities provided by Eq. (4.69), the weighted minimum norm solution is

$$\dot{\boldsymbol{\eta}}_d = [W][Q]^T \left([Q][W][Q]^T\right)^{-1} \boldsymbol{L}_r \tag{4.76}$$

where the matrix $[Q]$ is now defined as

$$[Q] = \Big[D_0 \vdots D\Big] \tag{4.77}$$

The angular velocity steering law in Eq. (4.76) is adopted as a *target vector* of wheel speeds and gimbal rates, and now we introduce a Lyapunov tracking approach to command the corresponding accelerations. The vector $\dot{\boldsymbol{\eta}}$ contains the actual $\boldsymbol{\Omega}$ and $\dot{\boldsymbol{\gamma}}$ states. As is done with CMG steering laws in Ref. 16, a feedback law is designed around the desired $\dot{\boldsymbol{\eta}}_d$ such that the current $\boldsymbol{\eta}$ will approach $\dot{\boldsymbol{\eta}}_d$. To accomplish this let's define the positive definite Lyapunov function $V_{\dot{\gamma}}$ as

$$V_{\dot{\gamma}} = \frac{1}{2}\left(\dot{\boldsymbol{\eta}}_d - \dot{\boldsymbol{\eta}}\right)^T \left(\dot{\boldsymbol{\eta}}_d - \dot{\boldsymbol{\eta}}\right) \tag{4.78}$$

whose derivative is

$$\dot{V}_{\dot{\gamma}} = \left(\dot{\boldsymbol{\eta}}_d - \dot{\boldsymbol{\eta}}\right)^T \left(\ddot{\boldsymbol{\eta}}_d - \ddot{\boldsymbol{\eta}}\right) \tag{4.79}$$

To guarantee global asymptotic stability, $\dot{V}_{\dot{\gamma}}$ is set to

$$\dot{V}_{\dot{\gamma}} = -K_{\dot{\gamma}} \left(\dot{\boldsymbol{\eta}}_d - \dot{\boldsymbol{\eta}}\right)^T \left(\dot{\boldsymbol{\eta}}_d - \dot{\boldsymbol{\eta}}\right) \tag{4.80}$$

where $K_{\dot{\gamma}}$ is a positive scalar quantity. This leads to the following stability constraint, which is also an acceleration steering law that tracks $\dot{\boldsymbol{\eta}}_d$ in a stable manner.

$$\ddot{\boldsymbol{\eta}} = K_{\dot{\gamma}} \left(\dot{\boldsymbol{\eta}}_d - \dot{\boldsymbol{\eta}}\right) + \ddot{\boldsymbol{\eta}}_d \tag{4.81}$$

As is done in designing the single-gimbal CMG acceleration steering law in Ref. 16, the vector $\ddot{\boldsymbol{\eta}}_d$ is assumed to be small and is neglected relative to the much larger term of Eq. (4.81). Substituting Eq. (4.76) into (4.81) yields

$$\ddot{\boldsymbol{\eta}} = \begin{bmatrix} \ddot{\boldsymbol{\Omega}} \\ \ddot{\boldsymbol{\gamma}} \end{bmatrix} = K_{\dot{\gamma}} \left( [W][Q]^T \left([Q][W][Q]^T\right)^{-1} \boldsymbol{L}_r - \begin{bmatrix} \dot{\boldsymbol{\Omega}} \\ \dot{\boldsymbol{\gamma}} \end{bmatrix} \right) \tag{4.82}$$

The vector $\ddot{\boldsymbol{\gamma}}$ is the desired gimbal angle acceleration vector. The vector $\ddot{\boldsymbol{\Omega}}$, which represents the reaction wheel "jerk", is also assumed to be very small and is neglected. After some algebraic manipulations, the desired RW and CMG angular acceleration vectors are given through the steering law[56]

$$\begin{bmatrix} \dot{\boldsymbol{\Omega}} \\ \ddot{\boldsymbol{\gamma}} \end{bmatrix} = \begin{bmatrix} I & 0 \\ 0 & K_{\dot{\gamma}} I \end{bmatrix} \left( [W][Q]^T \left([Q][W][Q]^T\right)^{-1} \boldsymbol{L}_r - \begin{bmatrix} 0 \\ \dot{\boldsymbol{\gamma}} \end{bmatrix} \right) \tag{4.83}$$

Note that the RW angular acceleration vector $\dot{\boldsymbol{\Omega}}$ in Eq. (4.83) is the same as is commanded by the velocity based steering law in Eq. (4.69). Since generally the initial $\dot{\boldsymbol{\gamma}}$ vector will not be equal to the desired velocity vector at the beginning of a maneuver, the gimbal acceleration vector $\ddot{\boldsymbol{\gamma}}$ will drive the gimbal velocities to the desired values and then remain relatively small following the stable initial transient.

### *4.2.5 Reconfiguring VSCMG Cluster Using Null Motion*

To perform a given spacecraft maneuver, there are an infinity of possible CMG configurations that would produce the required torques. Depending on the torque direction and a given CMG momentum, some of these initial gimbal configurations will encounter CMG singularities during the resulting maneuver while others will not. Vadali et al. show in Ref. 20 a method to compute a preferred set of initial gimbal angles $\boldsymbol{\gamma}(t_0)$ with which the maneuver will not encounter any CMG singularities. To reorient the CMG cluster to these preferred gimbal angles, the null motion of $[D_1]\dot{\boldsymbol{\gamma}} = \boldsymbol{L}_r$ is used which does not apply any torque on the spacecraft. However, the set of gimbal angles between which one can reorient the classical CMGs is very limited since the internal CMG cluster momentum vector must remain constant. Also, the null motion involves the inverse of the $[D_1][D_1]^T$ matrix which has to be approximated with the singularity robustness inverse whenever the determinant goes to zero. This approximation results in a small torque being applied to the spacecraft itself.

Rearranging the VSCMGs however, there are now twice as many degrees of control available. A common four-CMG pyramid configuration would have eight degrees of control instead of four, and more importantly, instead of having a one dimensional nullspace, we have a five dimensional nullspace. In particular, the CMG angles can be rearranged in a more general manner by also varying the RW spin speed vector $\boldsymbol{\Omega}$. The null motion of Eq. (4.67) is given by

$$\dot{\boldsymbol{\eta}} = \Big[[I_{N\times N}] - [W][Q]^T \left([Q][W][Q]^T\right)^{-1} [Q]\Big]\, \boldsymbol{d} = [\tau]\boldsymbol{d} \tag{4.84}$$

Numerical studies have shown that the weight matrix $[W]$ can be held constant for the VSCMG null motion. If a reconfiguration can be done by the classical CMG null motion, then the resulting VSCMG is identical and the RW modes are not used. Note

that the symmetric matrix $[\tau]$ is a projection matrix and has the useful property that $[\tau]^2 = [\tau]$. Let the constant vector $\boldsymbol{\eta}_f$ be a preferred set of $\boldsymbol{\Omega}_f$ and $\boldsymbol{\gamma}_f$. The error vector $\boldsymbol{e}$ is defined as

$$\boldsymbol{e} = [A]\,(\boldsymbol{\eta}_f - \boldsymbol{\eta}) \tag{4.85}$$

where $[A]$ is the diagonal matrix

$$[A] = \begin{bmatrix} a_{RW}[I_{N\times N}] & [0_{N\times N}] \\ [0_{N\times N}] & a_{CMG}[I_{N\times N}] \end{bmatrix} \tag{4.86}$$

The parameters $a_{RW}$ and $a_{CMG}$ are either 1 or 0. If one is set to zero, this means that the resulting null motion will be performed with no preferred set of either $\boldsymbol{\Omega}_f$ or $\boldsymbol{\gamma}_f$. The derivative of $\boldsymbol{e}$ is

$$\dot{\boldsymbol{e}} = -[A]\dot{\boldsymbol{\eta}} \tag{4.87}$$

The total error between preferred and actual CMG angular speed states is given through the Lyapunov function

$$V_e(\boldsymbol{e}) = \frac{1}{2}\boldsymbol{e}^T\boldsymbol{e} \tag{4.88}$$

Using Eqs. (4.84) and (4.87), the derivative of the Lyapunov function is

$$\dot{V}_e = \boldsymbol{e}^T\dot{\boldsymbol{e}} = -\boldsymbol{e}^T[A][\tau]\boldsymbol{d} \tag{4.89}$$

After setting $\boldsymbol{d} = k_e\boldsymbol{e}$, where the scalar $k_e$ is a positive, and making use of the properties $[A]\boldsymbol{e} = \boldsymbol{e}$ and $[\tau]^2 = [\tau]$, $\dot{V}_e$ is rewritten as

$$\dot{V}_e = -k_e\boldsymbol{e}^T[\tau]^T[\tau]\boldsymbol{e} \leq 0 \tag{4.90}$$

which is negative semi-definite. Therefore the VSCMG null motion

$$\dot{\boldsymbol{\eta}} = k_e \left[ [I_{N\times N}] - [W][Q]^T \left( [Q][W][Q]^T \right)^{-1} [Q] \right] [A] \begin{pmatrix} \boldsymbol{\Omega}_f - \boldsymbol{\Omega} \\ \boldsymbol{\gamma}_f - \boldsymbol{\gamma} \end{pmatrix} \tag{4.91}$$

is a globally stable motion. Note however, that no guarantee as to asymptotic stability can be made. As was the case with the classical single-gimbal CMG null motion, it is still not possible to reorient between any two arbitrary sets of $\boldsymbol{\eta}$ vectors since the internal momentum vector must be conserved. If the momentum is not conserved, then some torque acts on the spacecraft.

## 4.3 Numerical Simulations

### *4.3.1 Feedback Control Laws*

Neglecting the VSCMG transverse and gimbal inertia effects not only simplifies the analysis and simulation, but only directly provides the correct control input $\dot{\boldsymbol{\gamma}}$ required by CMGs. However, including these small inertia terms and using the gimbal acceleration based steering law provides for a more accurate simulation. Also, the physical torques required by the RW and CMG torque motors can be obtained. The first simulation will use the gimbal velocity based steering law in Eq. (4.69) to study the desired performance. The second simulation will use the acceleration based steering law to verify that it does indeed track the velocity based steering law.

A rigid spacecraft with some initial body angular velocity $\boldsymbol{\omega}$ and non-zero attitude $\boldsymbol{\sigma}$ is to be brought to rest at a zero attitude vector. The $\boldsymbol{\sigma}$ vector is assumed to be measured from a desired attitude. Four equal VSCMGs are embedded in the spacecraft in a standard pyramid configuration as shown in Figure 4.3. All simulation parameters are shown in Table 4.1. The angular velocity feedback matrix $[P]$ is chosen to be of diagonal form with the entries shown in the table. The initial $\dot{\boldsymbol{\gamma}}$ value is only

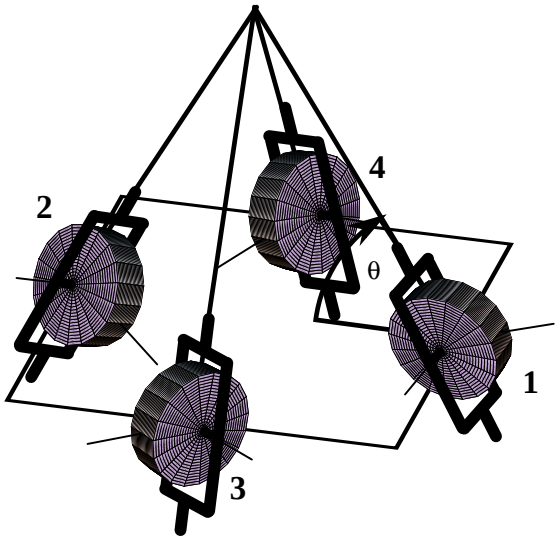


**Fig. 4.3:** Four VSCMGs in a Pyramid Configuration

used in the gimbal acceleration based steering law.

The VSCMG steering laws are compared to the single-gimbal CMG steering laws presented by Oh and Vadali in Ref. 16. Their steering law combines the Singularity Robustness Steering Law (SRSL) given by

$$\dot{\boldsymbol{\gamma}} = [D_1]^T \left( [D_1][D_1]^T + \alpha [I_{3x3}] \right)^{-1} \boldsymbol{L}_r \tag{4.92}$$

with a variable angular velocity feedback gain matrix $[P]$. The parameter $\alpha$ depends on the singularity index $\delta$ through

$$\alpha = \alpha_0 e^{-\delta} \tag{4.93}$$

The SRSL smoothly handles rank deficient $[D_1]$ matrices by having a slightly inaccurate matrix inverse. To escape situations where the orthogonality index $\mathcal{O}$ has gone to zero, the required torque is varied by changing the feedback gain matrix $[P]$ elements

**Table 4.1:** VSCMG Simulation Parameters

| Parameter | Value | Units |
|---|---|---|
| $I_{s_1}$ | 86.215 | kg-m$^2$ |
| $I_{s_2}$ | 85.070 | kg-m$^2$ |
| $I_{s_3}$ | 113.565 | kg-m$^2$ |
| $\boldsymbol{\sigma}(t_0)$ | [0.414 0.3 0.2] | |
| $\boldsymbol{\omega}(t_0)$ | [0.01 0.05 $-$ 0.01] | rad/sec |
| $N$ | 4 | |
| $\theta$ | 54.75 | degrees |
| $J_s$ | 0.13 | kg-m$^2$ |
| $J_t$ | 0.04 | kg-m$^2$ |
| $J_g$ | 0.03 | kg-m$^2$ |
| $\gamma_i(t_0)$ | [0 0 90 $-$ 90] | deg |
| $\dot{\gamma}_i(t_0)$ | [0 0 0 0] | rad |
| $\Omega(t_0)$ | 14.4 | rad/sec |
| $[P]$ | [13.13 13.04 15.08] | kg-m$^2$/sec |
| $K$ | 1.70 | kg-m$^2$/sec$^2$ |
| $K_{\dot{\gamma}}$ | 1.0 | sec$^{-1}$ |
| $W_{s_i}^0$ | 2.0 | |
| $W_{g_i}$ | 1.0 | |
| $\mu$ | $10^{-9}$ | |

through

$$[P] = \begin{bmatrix} P_1 & -\delta P & \delta P \\ \delta P & P_2 & -\delta P \\ -\delta P & \delta P & P_3 \end{bmatrix} \tag{4.94}$$

where the smoothly varying parameter $\delta P$ is related to the orthogonality factor through

$$\delta P = \begin{cases} \delta P_0 \frac{\mathcal{O}_0 - \mathcal{O}}{\mathcal{O}_0} & \text{for } \mathcal{O} < \mathcal{O}_0 \\ 0 & \text{for } \mathcal{O} \geq \mathcal{O}_0 \end{cases} \tag{4.95}$$

The parameter $\mathcal{O}_0$ was set to 0.01 and $\delta P_0$ is 0.1. The comparison of the steering laws is not done to establish that one control law is necessarily better than the other. They both have different purposes. The modified SRSL method is included because

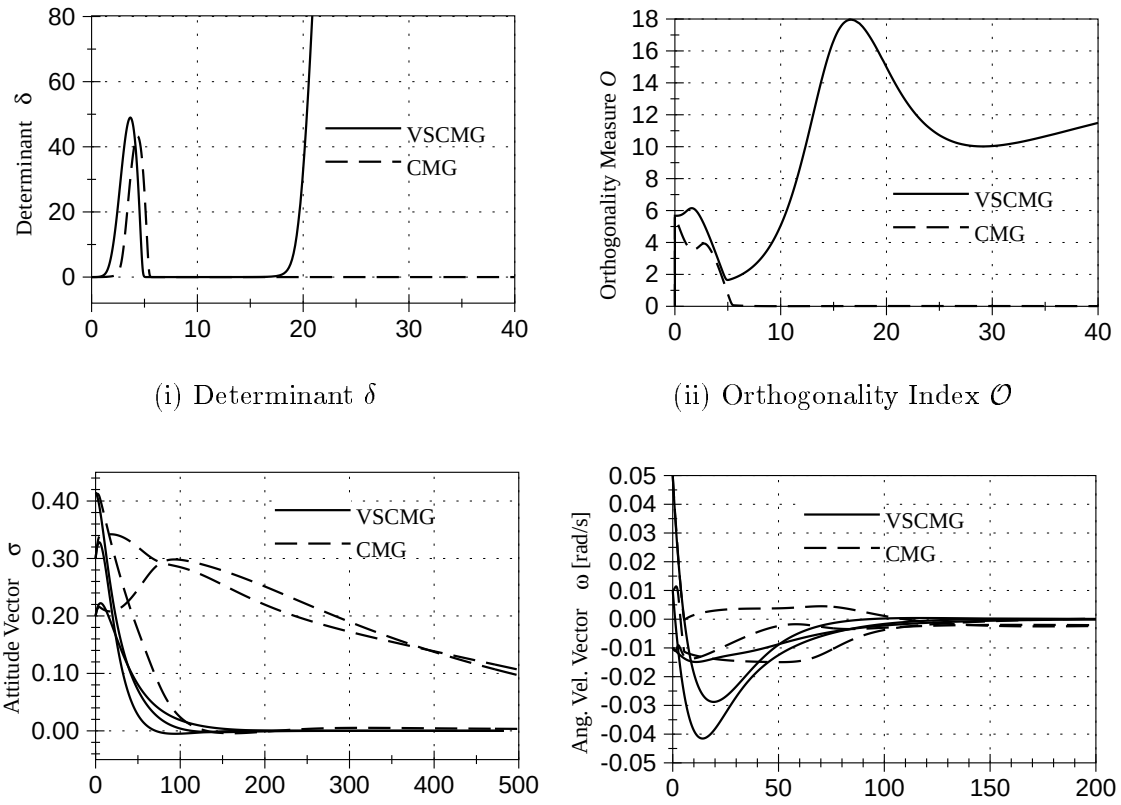


(i) Determinant $\delta$ (ii) Orthogonality Index $\mathcal{O}$

(iii) MRP Attitude Vector (iv) Body Ang. Vel. Vector

**Fig. 4.4:** Spacecraft Information of $\dot{\gamma}$ Based Steering Law

it illustrates the inherent problems of classical single-gimbal CMG steering laws and how they temporarily may not be able to provide the required torque. The VSCMG steering law is designed to *always* provide the required torque. However, as will be seen in the following simulations, this does come at a price of increased energy consumption, and in practice, the possibility of occasional wheel speed saturation.

This first simulation utilizes the VSCMG steering law in Eq. (4.69). As a comparison, the results of using the modified SRSL in Ref. 16 are included too and are indicated by the dashed lines in Fig. 4.4. Having the third and fourth VSCMG gimbal angles be initially +90 and -90 degrees each makes the dimensional determinant $\delta$ zero at the beginning of the simulation as is shown in Figure 4.4(i). The determinant

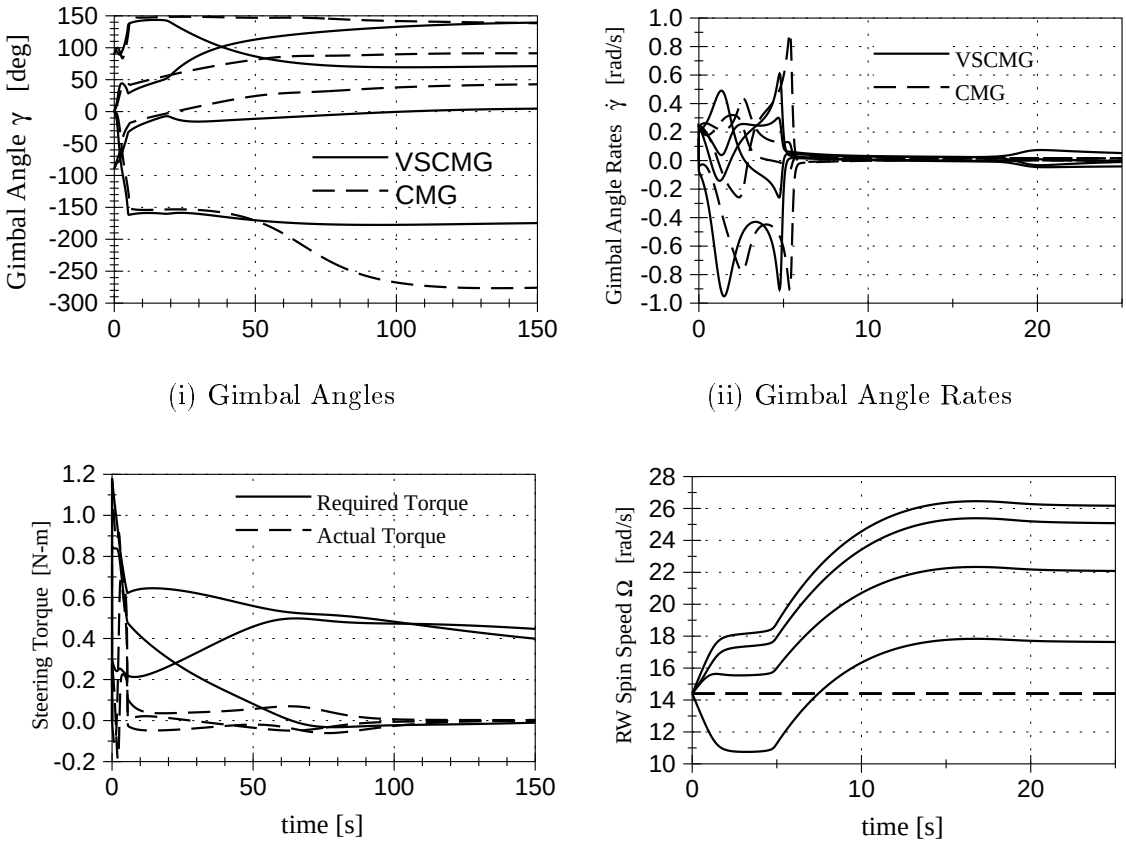


(i) Gimbal Angles

(ii) Gimbal Angle Rates

(iii) Required vs. Actual Torque

(iv) RW spin speed

**Fig. 4.5:** VSCMG Information of $\dot{\gamma}$ Based Steering Law

becomes nonzero for a few seconds and then goes back to zero for a while. About 18 seconds into the maneuver, the determinant becomes nonzero for the VSCMG steering law and then remains nonzero for the entire maneuver duration of 500 seconds. The standard CMG steering law has a similar behavior initially, but never becomes nonzero again after dipping back to zero at 5 seconds into the maneuver. The reason for this is seen by studying the dimensional orthogonality index $\mathcal{O}$ in Figure 4.4(ii). The index $\mathcal{O}$ is nonzero to begin with, allowing the CMG steering law to provide some torque onto the spacecraft. However, as the $\delta$ becomes zero again $\mathcal{O}$ also goes to zero for the CMG steering law, while the VSCMG steering law retains a nonzero

$\mathcal{O}$ throughout the maneuver. The modified feedback gain matrix $[P]$ does change $\boldsymbol{L}_r$ sufficiently that the spacecraft does approach the desired attitude as is shown in Figure 4.4(iii). However, this occurs very slowly. Here is a situation where the classical CMG steering law effectively remains trapped near a singular configuration which results in a very degraded performance. On the other hand, both the attitude and body angular velocity decay as described by the feedback law for the VSCMG as shown in Figures 4.4(iii) and 4.4(iv). If it were essential for the mission that the spacecraft actually follow the prescribed trajectory, the results of the classical CMG steering law clearly would be unsatisfactory, while the VSCMG steering law stays right on track.

Figures 4.5(i) and 4.5(ii) show the gimbal angles and gimbal angle rate time histories. For both the VSCMG and CMG steering law the gimbal rates are relatively large at the beginning of the maneuver where the CMGs remain close to a singular configuration. After about 6 seconds the CMG rates remain almost zero since the steering law is essentially "entrapped" in the singular configuration. Figure 4.5(iii) compares the required torque $\boldsymbol{L}_r$ to the actual torque $\boldsymbol{L}_a$ produced by the CMG steering law. The VSCMG actual torque is not shown in this figure since it always is equal to $\boldsymbol{L}_r$. While having the SRSL and the time varying $[P]$ matrix to help the standard CMG steering law and this spacecraft would eventually reach the desired target state, this Figure shows clearly that the actual torque produced at several time segments much less than the required torque. However, for the VSCMG steering law to keep the spacecraft on track comes at the expense of spinning the RW up or down on occasion. The RW spin speeds $\boldsymbol{\Omega}$ are shown in Figure 4.5(iv). The RW mode is employed twice when the determinant $\delta$ goes to zero. Once the CMGs are away for a singular configuration, the spin speeds remain essentially constant.

The second numerical simulation uses the gimbal acceleration-based steering law

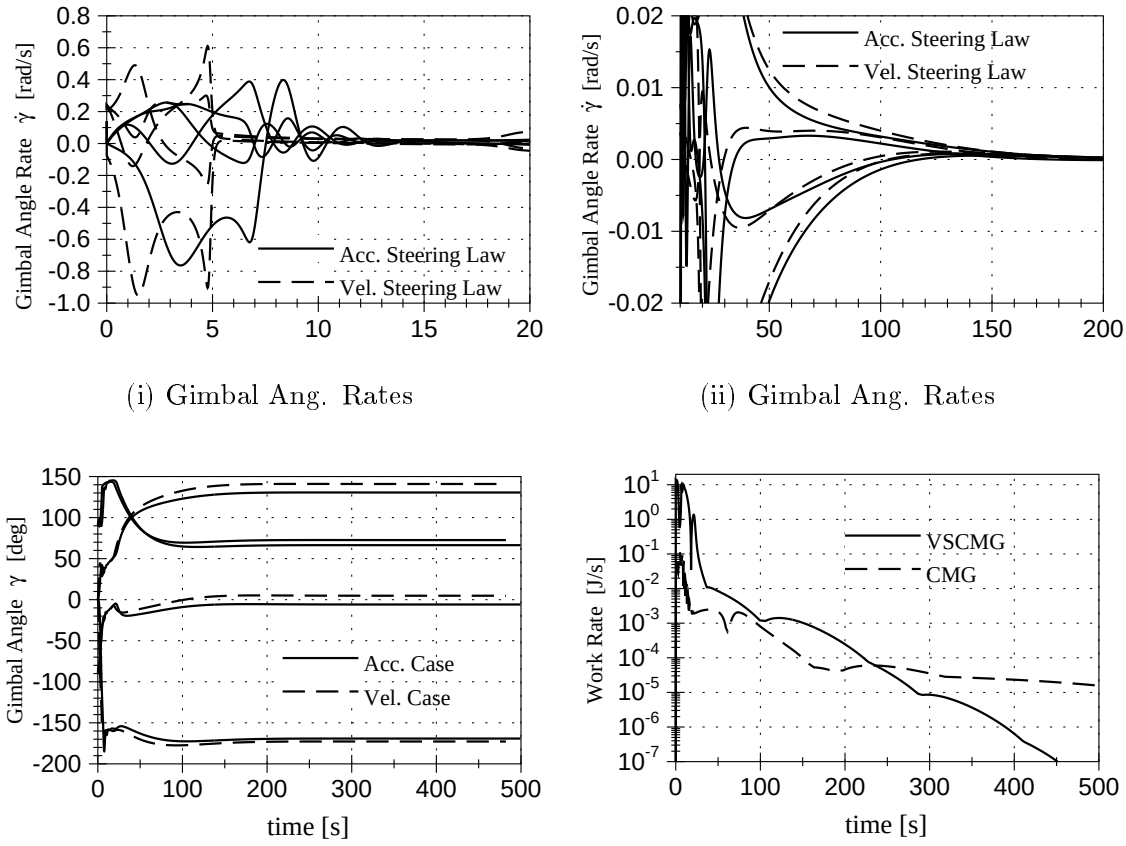


(i) Gimbal Ang. Rates (ii) Gimbal Ang. Rates

(iii) Gimbal Angles (iv) Work Rates

**Fig. 4.6:** Gimbal Acceleration Based Steering Law Simulation

in Eq. (4.83) and the results are shown in Figure 4.6. The gimbal acceleration were designed such that they would provide essentially the same performance as the velocity based steering law. Figures 4.6(i) and 4.6(ii) show the gimbal angle rates for both the gimbal acceleration and velocity based steering law. As expected, during the initial phase of the maneuver the two gimbal rates are quite different as seen in Figure 4.6(i). This is because the initial gimbal rates were set to zero and were not equal to the desired gimbal rates from Eq. (4.69). However, as Figure 4.6(ii) shows clearly, after about 10 to 20 seconds into the maneuver, the gimbal rate performance of the acceleration steering approaches that of the desired velocity based steering law.

The corresponding gimbal angles for both cases are shown in Figure 4.6(iii).

The natural drawback to using the RW modes of the VSCMG to maneuver through classical CMG singularities is evident when studying the work rate of the VSCMG steering law compared to the standard CMG steering law in Figure 4.6(iv). The work rate $\dot{W}$ for the VSCMGs is defined as

$$\dot{W} = \sum_{i=1}^{N} \left[ |\Omega_i u_{s_i}| + |\dot{\gamma}_i u_{g_i}| \right] \tag{4.96}$$

During the initial phase of the maneuver, where the determinant $\delta$ is very small, the energy consumption to drive the RW modes is relatively large compared to the CMG modes. Away from this singularity, the energy consumption is very comparable to that of the CMG steering law. The power required to generate RW torques is typically the limiting factor for the VSCMG devices to decide on how large a structure they could be used. However, for smaller spacecraft which may be able to afford occasional RW modes, or even for larger spacecraft with proper tuning of the control laws, the VSCMG steering law provides interesting possibilities. Other authors have looked into augmenting CMG cluster with thrusters to keep the spacecraft on track during near singular configurations. Using the RW modes has several benefits over using thrusters. They provide a much smoother response compared to using thrusters and will excite few flexible modes within the spacecraft. Also, RW don't require propellant to operate, but use electrical power which can be readily recharged from solar arrays.

### *4.3.2 VSCMG Null Motion Maneuvers*

To illustrate the interesting properties of the VSCMG null motion, various simulations were run. The scalar $k_e$ is set to 0.1 and the weights $W_{s_i}$ are held constant at 2 for all simulations unless noted otherwise. The feedback gains $[P]$ and $K$ are set to zero to turn off any station keeping control. In no simulation did the VSCMG null motion

cause an effective torque on the spacecraft.

The first simulation is equivalent to the one ran by Oh and Vadali in Ref. 20 to demonstrate their CMG null motion control law to reconfigure the gimbal angles. The initial and preferred gimbal angles are $(0, 0, 0, 0)$ degrees and $(45, 45, -45, -45)$ degrees respectively. Note that the internal CMG cluster momentum vector is zero for both configurations and the CMG null motion is able to perform this reconfiguration. The results of both the CMG and the VSCMG null motion are shown in Figure 4.7.

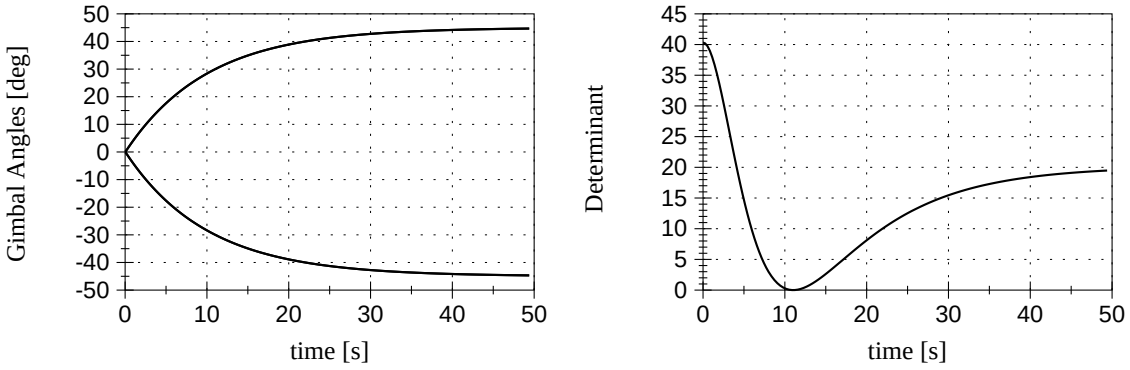


(i) Gimbal Angles $\boldsymbol{\gamma}$ (ii) Determinant $\delta$

**Fig. 4.7:** VSCMG Null Motion Simulation No. 1

Even though the weights $W_{s_i}$ on the RW mode were non-zero, the two maneuvers are identical. The gimbal angles are reoriented to the desired angles as shown in Figure 4.7(i). The minimum norm inverse automatically uses the CMGs exclusively here since they would require the least control effort. As shown in Figure 4.7(ii),even though the determinant does go through zero about 11 seconds into the maneuver, calculating the inverse of $[Q][W][Q]^T$ never poses any numerical problems since this matrix is always full rank for the VSCMGs. Therefore the VSCMG null motion falls back to the CMG null motion if possible.

The second simulation is identical to the first, except that the initial gimbal

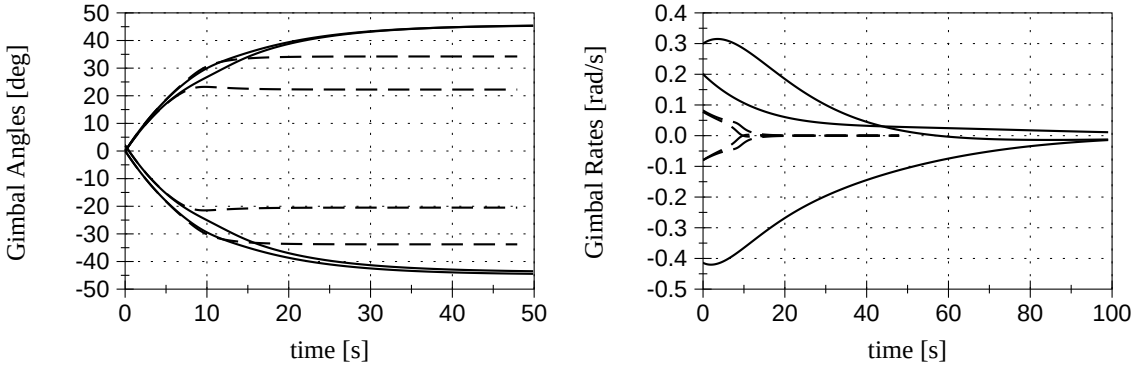


(i) Gimbal Angles $\boldsymbol{\gamma}$ (ii) Gimbal Ang. Rates $\dot{\boldsymbol{\gamma}}$

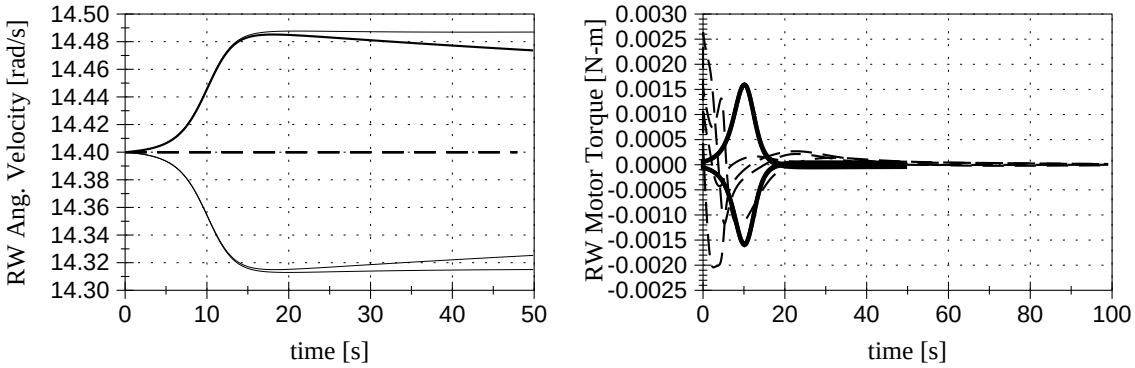


(iii) RW Spin Speeds $\boldsymbol{\Omega}$ (iv) RW Motor Torques $\boldsymbol{u}_s$

**Fig. 4.8:** VSCMG Null Motion Simulation No. 2

angles now are $(0, 0, 0, 2)$ degrees respectively. The classical CMG null motion will not be able to reconfigure the gimbals as desired without applying a torque to the spacecraft. The reason for this is that the initial CMG cluster momentum vector is non-zero, while the preferred gimbal angles would have a zero momentum vector. The results shown in Figure 4.8 were obtained with $a_{RW} = 0$ and $a_{CMG} = 1$. In other words, here it did not matter how the RW spin speeds changed, as long as the final gimbal angles approached the preferred sets. The CMG null motion results are shown as dashed lines while the VSCMG null motion is indicated with solid lines. Figure 4.8(i) clearly shows that while the VSCMG null motion is very close

to achieving the preferred gimbal angles after 50 seconds into the simulation, the CMG null motion stops short of the task. The required VSCMG gimbal rates remain relatively small. State of the art CMGs can produce gimbal rates of about 2 radians per second. The RW spin speeds are shown in Figure 4.8(iii). While the CMG null motion kept $\Omega_i$ constant, the VSCMG null motion adjusts them slightly to maintain a constant internal momentum vector. What is very interesting is that the change in $\Omega_i$ is very minimal. The corresponding RW motor torques are shown as a heavy black line in Figure 4.8(iv). Recall that conventional CMGs maintain a constant $\Omega_i$ during a spacecraft reorientation by having a separate RW feedback loop. To give a feel of the VSCMG null motion RW motor torques, the CMG reaction wheel feedback torque for a sample spacecraft maneuver are superimposed with dashed lines. The conclusion, for this case, is that the torques required to perform this VSCMG null motion is of the same order as what standard CMG are capable of producing already. Implementing VSCMG null motion often would not require a complete re-engineering of the gyro system, but simply a change in the feedback control law.

The same simulation was repeated with $a_{RW}$ set to 1 and $\mathbf{\Omega}_f = \mathbf{\Omega}(t_0)$. The RW spin speed are ideally to be kept constant during this maneuver. The results are shown in Figure 4.9. The CMG null motion solution is not shown here. Figure 4.9(i) shows that the gimbal angles are very close the to preferred gimbal angles after 50 seconds of maneuver time, but not quite as close as they came in the previous simulation. The RW spin speeds are shown in Figure 4.9(ii). The first 15 seconds look like the previous simulation. After this though the $\Omega_i$ are reduced and they approach their initial states. The corresponding RW motor torques are shown in Figure 4.9(iii) and are still of the same order of magnitude. This maneuver illustrates that sometimes it is possible to have both preferred gimbal angles and RW spin speeds. While the current $\gamma_i$ and $\Omega_i$ appear to be converging to the preferred values, it is impossible for them to

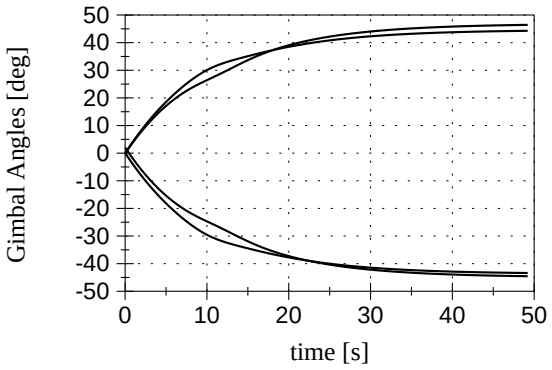


(i) Gimbal Angles $\boldsymbol{\gamma}$

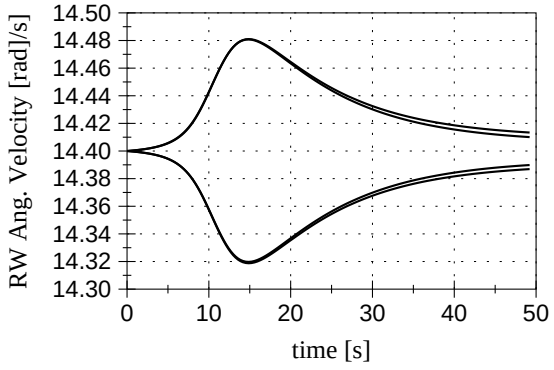


(ii) RW Spin Speeds $\boldsymbol{\Omega}$

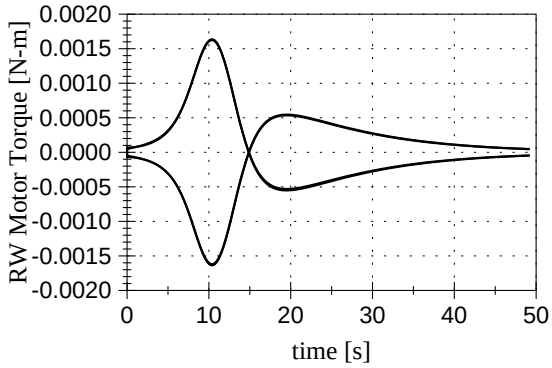


(iii) RW Motor Torques $\boldsymbol{u}_s$

**Fig. 4.9:** VSCMG Null Motion Simulation No. 3

actually reach. This is because if the preferred $\gamma_i$ and $\Omega_i$ are actually obtained, the VSCMG cluster would have a different momentum vector. While arbitrary sets of $\boldsymbol{\gamma}_f$ $and$ $\boldsymbol{\Omega}_f$ cannot be achieved, this example illustrates that in some cases it is possible to get close enough. If the final gimbal angles are not precisely at the preferred values, the resulting trajectory should still be singularity free; they gimbal sets might just come closer to singular configurations.

The initial gimbal angles in the previous two simulations were very close to the gimbal angles in the first simulation which the CMG null motion was able to reconfigure to the preferred angles. In the next simulation the initial gimbal angles

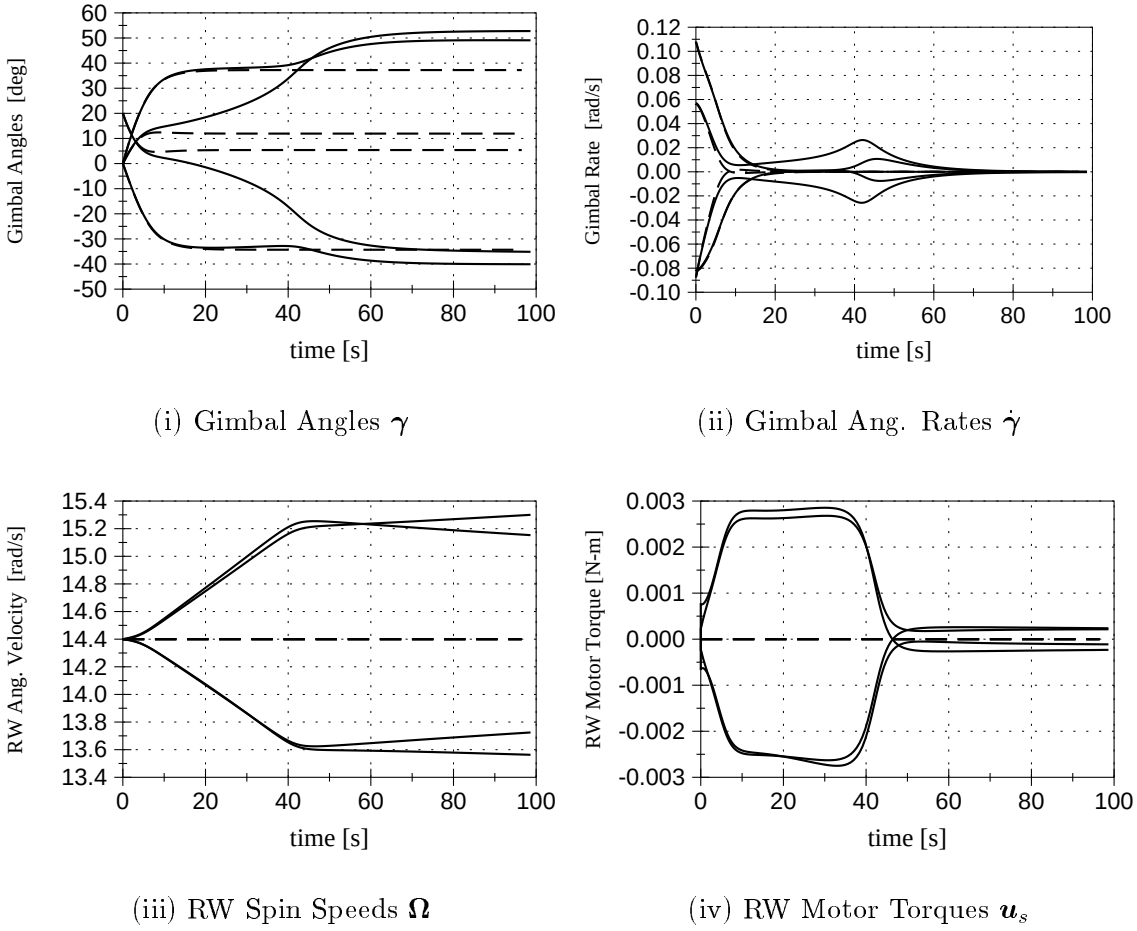


(i) Gimbal Angles $\boldsymbol{\gamma}$

(ii) Gimbal Ang. Rates $\dot{\boldsymbol{\gamma}}$

(iii) RW Spin Speeds $\boldsymbol{\Omega}$

(iv) RW Motor Torques $\boldsymbol{u}_s$

**Fig. 4.10:** VSCMG Null Motion Simulation No. 4

are set to be $(0, 0, 0, 20)$ degrees respectively. The first case was with $a_{RW}$ set to zero. Figure 4.10(i) shows that the CMG null motion does not to a good job reorienting the gimbal angles towards the preferred set. The VSCMG null motion once again is able to reconfigure the gimbals very close to the desired values while maintaining small gimbal velocities (shown in Figure 4.10(ii). The RW spin speeds, shown in Figure 4.10(iii), are increased more than was the case in the previous simulation, but all reaction wheels have a sufficient wheel speed to make them effective CMG devices. The required RW motor torques, shown in Figure 4.10(iv), still remain within the same level of what the standard CMG feedback control is able to achieve.

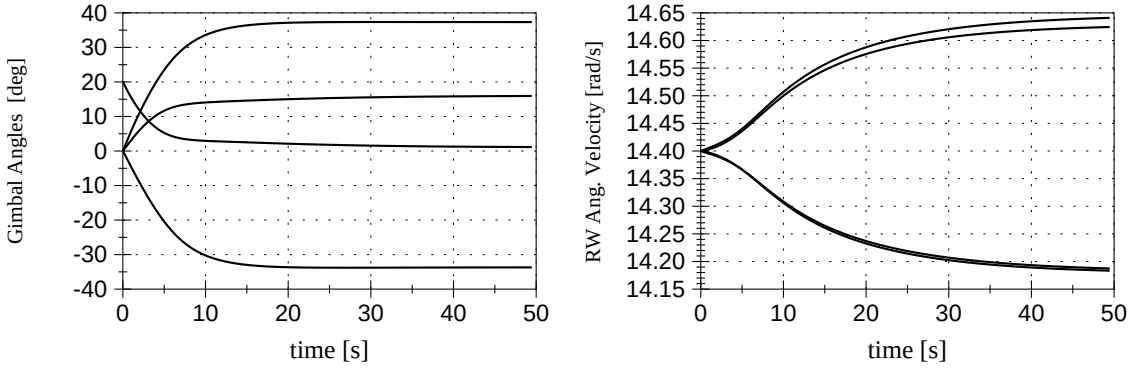


(i) Gimbal Angles $\boldsymbol{\gamma}$ (ii) RW Spin Speeds $\boldsymbol{\Omega}$

**Fig. 4.11:** VSCMG Null Motion Simulation No. 5

The second case was run with $a_{RW} = 1$ and $\boldsymbol{\Omega}_f = \boldsymbol{\Omega}(t_0)$. Only the VSCMG null motion results are shown in Figure 4.11. Since actually achieving the preferred $\boldsymbol{\gamma}_f$ and $\boldsymbol{\Omega}_f$ would drastically change the internal momentum vector, these two desired sets are mutually contradictory. Figure 4.11(i) shows that the gimbal angles quickly become stationary far away from their preferred values. The $\Omega_i$, shown in Figure 4.11(ii), varies a little, but remains close to the preferred set. Forcing the $\Omega_i$ to remain close to the preferred set essentially keeps the VSCMG from performing their task.

The last simulation, shown in Figure 4.12, illustrates the use of the VSCMG null motion to change the RW spin speed while leaving the gimbal angles free. After having performed a maneuver with the VSCMG feedback control law, it is possible that the RWs may have been spun up or down too much. Using the VSCMG null motion it is possible to redistribute the VSCMG cluster momentum vector among its RW and CMG modes. To illustrate the feasibility of such maneuvers, the following drastic task is performed. The preferred RW spin speeds are set to be the negative of their initial values, i.e. all the momentum of the RWs is to be reversed. Clearly, not a maneuver for the faint hearted! The parameter $a_{CMG}$ is set to zero here. The

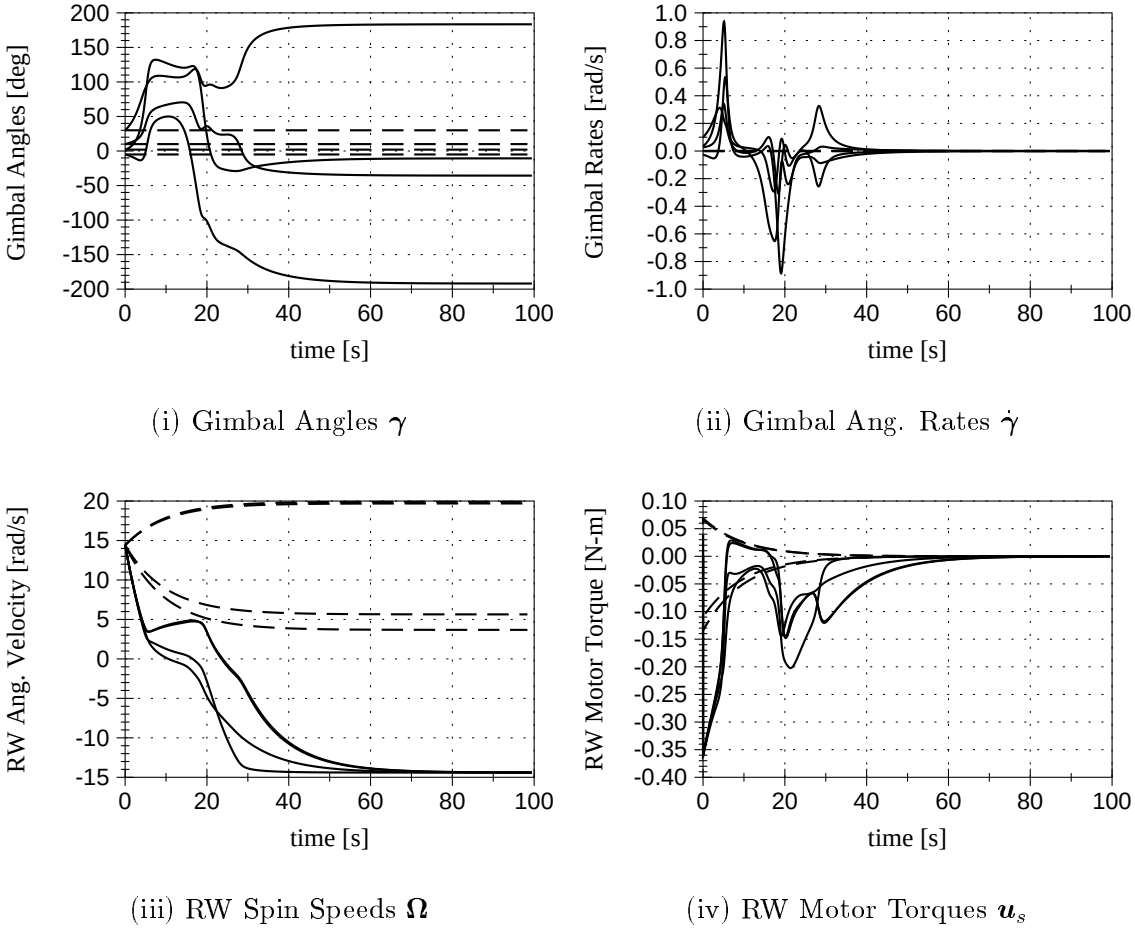


(i) Gimbal Angles $\boldsymbol{\gamma}$

(ii) Gimbal Ang. Rates $\dot{\boldsymbol{\gamma}}$

(iii) RW Spin Speeds $\boldsymbol{\Omega}$

(iv) RW Motor Torques $\boldsymbol{u}_s$

**Fig. 4.12:** VSCMG Null Motion Simulation No. 6

results of trying to use pure RW null motion to perform this difficult task are shown as dashed lines in Figure 4.12, while the VSCMG null motion results are indicated through solid lines. As expected, the pure RW null motion is not able to perform the required task and keep the gimbal angles constant at the same time. However, the VSCMG null motion is able to achieve the objective as seen in Figure 4.12(iii). After about 60 seconds into the maneuver all RW momentums has been reversed. To keep the internal momentum vector constant, the gimbal angles naturally have to be varied as shown in Figure 4.12(i). It is interesting to note that two gimbal angles remain relatively close to zero and two hover around the $\pm 180$ degree orientation.

The required $\dot{\gamma}_i$ are shown in Figure 4.12(ii). Even for this extreme maneuver they remain within the feasible range. If these gimbal rates were to grow too large, then the VSCMG null motion maneuver could be slowed down by reducing the $k_e$ constant. The RW motor torques are shown in Figure 4.12(iv). These torques are of the level of what regular RW are capable of doing. To perform drastic RW spin speed changes clearly stronger torque motors are required than what is available with regular CMGs. However, the more typical moderate $\Omega_i$ changes can be performed with the available CMG RW feedback torque motor.

# CHAPTER V

## SUMMARY AND CONCLUSION

Three sets of new results were developed in this dissertation. The first set is very fundamental, dealing with the motion of a single rigid body. The second set of results address the controlled motion of a class of multi-body systems. The final set of results apply to spacecraft having variable speed control moment gyroscopes. For the dynamics and control of a rigid body, a novel family of attitude parameters (the stereographic parameters) is presented, including their general transformations to and from the Euler parameters. The SPs are not unique, but have a corresponding shadow or image set which can typically be used to avoid singularities. The exception to this are the classical Rodrigues parameters, a particular set of symmetric SPs, for which the original and shadow set are identical. The modified Rodrigues parameters are the most promising set of SPs and are studied in more detail. Unsaturated and saturated MRP feedback control laws are presented that work well for arbitrarily large attitude errors. Further, since the closed loop equations are nearly linear, the linearized feedback gain design provides an accurate performance prediction even when the spacecraft is performing very large rotations. To allow the MRPs along with their shadow sets to be used as globally non-singular attitude parameters in optimal control problems, the MRP costate switching condition is presented. Whenever the MRP vector is switched to the alternate set, the corresponding attitude costate vector is analogously mapped onto an alternate set. Using MRPs in optimal control problems allows solutions to have general rotations without resorting to the use of the redundant set of Euler parameters.

For a class of nonlinear multi-body dynamical systems, the Lagrange equations of motion in terms of the eigenfactor quasivelocities was presented. Their form provides

a natural "splitting" of dynamics and kinematics similar to what is commonly done in rigid body dynamics. While this formulation does have numerical advantages for particular systems, generally it was found that the computational cost of calculating the eigenfactor derivatives was too high. However, the EQV do appear to make good velocity feedback coordinates. EQV feedback control laws are presented for which the exponential energy decay rate can easily be controlled. For systems containing chains of rigid links such as found in robotic arms, the use of the EQV feedback control law resulted in the motion of each link being controlled in a "decoupled manner".

In the last chapter, the equations of motion of a rigid body containing several variable speed control moment gyroscopes is developed. While classical single-gimbal CMGs contain singular orientations, the VSCMG use their reaction wheel mode to drive through these orientations. This allows for a prescribed trajectory to be accurately followed. However, the RWs typically are far less efficient energy wise than the CMGs. To actually drive the VSCMGs through a CMG singularity might require a relatively large RW control input. The RW feedback control motor found on single-gimbal CMGs would have to be enlarged to accommodate such maneuvers. To avoid CMG singularities altogether, it is possible to reorient the gimbal angles initially such that the resulting maneuver is singularity free. A VSCMG null motion is discussed which allows for such reorientations to be performed in a more general manner than was previously possible with single-gimbal CMGs. The resulting RW motor torques required are typically small and feasible with the existing RW feedback motor found in existing CMGs. This VSCMG null motion can be used to generally redistribute the internal VSCMG cluster momentum vector. Therefore it is also possible to use this to change the RW wheel speeds if so desired.

# REFERENCES

[1] J. L. Junkins, "Adventures on the Interface of Dynamics and Control," *Journal of Guidance, Control and Dynamics*, Vol. 20, No. 6, Nov.–Dec. 1997, pp. 1058–1071.

[2] R. C. Nelson, *Flight Stability and Automatic Control.* New York: McGraw-Hill, Inc., 1989.

[3] P. Tsiotras and J. M. Longuski, "A New Parameterization of the Attititude Kinematics," *Journal of the Astronautical Sciences*, Vol. 43, No. 3, 1996, pp. 342–262.

[4] P. Tsiotras and J. M. Longuski, "Spin-Axis Stabilization of Symmetric Spacecraft with Two Control Torques," *Systems & Control Letters*, Vol. 23, 1994, pp. 395–402.

[5] J. L. Junkins and J. D. Turner, *Optimal Spacecraft Rotational Maneuvers.* Amsterdam, Netherlands: Elsevier Science Publishers, 1986.

[6] O. Rodriques, "Des Lois Geometriques qui Regissent Les Deplacements D'Un Systeme Solide Dans l'Espace, et de la Variation des Coordonnes Provenants de ces Deplacements Considers Independamment des Causes Qui Peuvent les Preduire," *LIOUV*, Vol. III, 1840, pp. 380–440.

[7] T. F. Wiener, *Theoretical Analysis of Gimballess Inertial Reference Equipment Using Delta-Modulated Instruments.* Ph.D. dissertation, Department of Aeronautics and Astronautics, Massachusetts Institute of Technology, March 1962.

[8] S. R. Marandi and V. J. Modi, "A Preferred Coordinate System and the Associated Orientation Representation in Attitude Dynamics," *Acta Astronautica*, Vol. 15, No. 11, 1987, pp. 833–843.

[9] P. Tsiotras, "Stabilization and Optimality Results for the Attitude Control Problem," *Journal of Guidance, Control and Dynamics*, Vol. 19, No. 4, 1996, pp. 772–779.

[10] P. Tsiotras, "A Passivity Approach to Attitude Stabilization Using Nonredundant Kinematic Parameterizations," *34th IEEE Conference on Decision and Control*, (Princeton University), March 20-22 1996, pp. 1238–1243.

[11] A. Jain and G. Rodriguez, "Diagonalized Lagrangian Robot Dynamics," *IEEE Trans. on Robotics and Automation*, Vol. 11, No. 4, Aug. 1995, pp. 571–584.

[12] R. L. Dailey, "Eigenvector Derivatives with Repeated Eigenvalues," *AIAA Journal*, Vol. 27, No. 4, April 1989, pp. 486–491.

[13] W. C. Mills-Curran, "Calculation of Eigenvector Derivatives for Structures with Repeated Eigenvalues," *AIAA Journal*, Vol. 26, No. 7, July 1988, pp. 867–871.

[14] D.-W. Zhang and F.-S. Wei, "Computation of Eigenvector Derivatives with Repeated Eigenvalues Using a Complete Modal Space," *AIAA Journal*, Vol. 33, No. 9, May 1995, pp. 1749–1753.

[15] Y.-Q. Zhang and W.-L. Wang, "Eigenvector Derivatives of Generalized Nondefective Eigenproblems with Repeated Eigenvalues," *Journal of Engineering for Gas Turbines and Power*, Vol. 117, Jan. 1995, pp. 207–212.

[16] H. S. Oh and S. R. Vadali, "Feedback Control and Steering Laws for Spacecraft Using Single Gimbal Control Moment Gyros," *Journal of the Astronautical*

*Sciences*, Vol. 39, No. 2, April–June 1991, pp. 183–203.

[17] S. R. Vadali, "On the Euler Parameter Constraint," *Journal of Astronautical Sciences*, Vol. 36. No 3, July–Sept. 1988, pp. 259–265.

[18] B. R. Hoelscher and S. R. Vadali, "Optimal Open-Loop and Feedback Control Using Single Gimbal Control Moment Gyroscopes," *Journal of the Astronautical Sciences*, Vol. 42, No. 2, April–June 1994, pp. 189–206.

[19] K. Ford and C. D. Hall, "Flexible Spacecraft Reorientations Using Gimbaled Momentum Wheels," *AAS/AIAA Astrodynamics Specialist Conference*, (Sun Valley, Idaho), August 1997. Paper No. 97-723.

[20] S. R. Vadali, H. S. Oh, and S. R. Walker, "Preferred Gimbal Angles for Single-Gimbal Control Moment Gyros," *Journal of Guidance, Control and Dynamics*, Vol. 13, No. 6, Nov.–Dec. 1990, pp. 1090–1095.

[21] H. Schaub and J. L. Junkins, "Stereographic Orientation Parameters for Attitude Dynamics: A Generalization of the Rodrigues Parameters," *Journal of the Astronautical Sciences*, Vol. 44, No. 1, Jan.–Mar. 1996, pp. 1–19.

[22] H. Schaub, P. Tsiotras, and J. L. Junkins, "Principal Rotation Representations of Proper NxN Orthogonal Matrices," *International Journal of Engineering Science*, Vol. 33, No. 15, 1995, pp. 2277–2295.

[23] H. Schaub, R. D. Robinett, and J. L. Junkins, "New Penalty Functions for Optimal Control Formulation for Spacecraft Attitude Control Problems," *Journal of Guidance, Control and Dynamics*, Vol. 20, No. 3, May–June 1997, pp. 428–434.

[24] P. Tsiotras, J. L. Junkins, and H. Schaub, "Higher Order Cayley Transforms with Applications to Attitude Representations," *Journal of Guidance, Control*

*and Dynamics*, Vol. 20, No. 3, May–June 1997, pp. 528–534.

[25] H. Schaub, R. D. Robinett, and J. L. Junkins, "Globally Stable Feedback Laws for Near-Minimum-Fuel and Near-Minimum-Time Pointing Maneuvers for a Landmark-Tracking Spacecraft," *Journal of the Astronautical Sciences*, Vol. 44, No. 4, Oct.–Dec. 1996, pp. 443–466.

[26] R. D. Robinett, G. G. Parker, H. Schaub, and J. L. Junkins, "Lyapunov Optimal Saturated Control for Nonlinear Systems," *35th Aerospace Sciences and Meeting*, (Reno, Nevada), Jan. 1997. paper No. 97-0112.

[27] M. D. Shuster, "A Survey of Attitude Representations," *Journal of the Astronautical Sciences*, Vol. 41, No. 4, 1993, pp. 439–517.

[28] J. L. Junkins and Y. Kim, *Introduction to Dynamics and Control of Flexible Structures*. Washington D.C.: AIAA Education Series, 1993.

[29] A. Cayley, "On the Motion of Rotation of a Solid Body," *Cambridge Mathematics Journal*, Vol. 3, 1843, pp. 224–232.

[30] R. Mukherjee and D. Chen, "Asymptotic Stability Theorem for Autonomous Systems," *Journal of Guidance, Control, and Dynamics*, Vol. 16, Sept.–Oct. 1993, pp. 961–963.

[31] R. Mukherjee and J. L. Junkins, "Invariant Set Analysis of the Hub-Appendage Problem," *Journal of Guidance, Control, and Dynamics*, Vol. 16, Nov.–Dec. 1993, pp. 1191–1193.

[32] R. A. Paielli and R. E. Bach, "Attitude Control with Realization of Linear Error Dynamics," *Journal of Guidance, Control and Dynamics*, Vol. 16, No. 1, Jan.–Feb. 1993, pp. 182–189.

[33] J. L. Junkins and H. Bang, "Lyapunov Optimal Control Law for Flexible Space Structure Maneuver and Vibration Control," *Journal of the Astronautical Sciences*, Vol. 41, No. 1, Jan.–Mar. 1993, pp. 91–118.

[34] Y. Kim, T. Suk, and J. L. Junkins, "Optimal Slewing and Vibration Control of Smart Structures," *Smart Structures, Nonlinear Dyanamics and Control*, Vol. II, Prentice Hall, to appear in 1998.

[35] B. Lee and W. J. Grantham, "Aeroassisted Orbital Maneuvering Using Lyapunov Optimal Feedback Control," *Journal of Guidance, Control and Dynamics*, Vol. 12, No. 2, 1989, pp. 237–242.

[36] D. E. Kirk, *Optimal Control Theory, An Introduction.* Networks Series, Englewood Cliffs, New Jersey: Prentice-Hall, Inc., 1970.

[37] D. G. Luenberger, *Optimization by Vector Space Methods.* New York, New York: John Wiley & Sons, Inc., 1969.

[38] A. E. Bryson and Y. Ho, *Applied Optimal Control.* Washington, D.C.: Hemisphere Publishing Corporation, 1975.

[39] G. Leitmann, *The Calculus of Variations and Optimal Control.* New York: Plenum Press, 1981.

[40] C. H. Denbow, "A Generalized Form of the Problem of Bolza," *In Contributions to the Calculus of Variations (1933–1937)*, University of Chicago Press, 1937.

[41] J. L. Junkins and H. Schaub, "Orthogonal Square Root Eigenfactor Parameterization of Mass Matrices," *Journal of Guidance, Control and Dynamics*, Vol. 20, No. 6, Nov.–Dec. 1997, pp. 1118–1124.

[42] J. L. Junkins and H. Schaub, "An Instantaneous Eigenstructure Quasi-Coordinate Formulation for Nonlinear Multibody Dynamics," *7th AAS/AIAA Space Flight Meeting*, (Huntsville, Alabama), Feb. 10–12 1997. paper No. AAS 97-119.

[43] J. L. Junkins and H. Schaub, "An Eigenfactor Square Root Algorithm Formulation for Nonlinear Dynamics," technical report, Aerospace Engineering Department, Texas A&M University, May 1996.

[44] M. H. Rheinfurth and H. B. Wilson, "Methods of Applied Dynamics," NASA Reference Publication 1262, NASA, Huntsville, Alabama, May 1991.

[45] E. Bayo and R. Ledesma, "Augmented Lagranian and Mass-Orthogonal Projection Methods for Constrained Multibody Dynamics," *Journal of Nonlinear Dynamics*, Vol. 9, Nos. 1–2, 1996, pp. 113–130.

[46] L. Meirovitch, *Methods of Analytical Dynamics*. New York: McGraw–Hill, 1970.

[47] J. G. Papastavridis, "On the Boltzmann-Hamel Equations of Motion: A Vectorial Treatment," *Journal of Applied Mechanics*, Vol. 61, June 1994, pp. 453–459.

[48] Y. Oshman and I. Y. Bar-Itzhack, "Eigenfactor Solution of the Matrix Riccati Equation — A Continuous Square Root Algorithm," *IEEE Trans. on Automatic Control*, Vol. AC-30, No. 10, Oct. 1985, pp. 971–978.

[49] Y. Kim, S. Lee, and J. L. Junkins, "Eigenvector Derivatives for Mechanical Second - Order Systems," *Journal of Guidance, Control and Dynamics*, Vol. 18, No. 4, July–Aug. 1995, pp. 899–906.

[50] C. G. J. Jacobi, "Über ein leichtes Verfahren die in der Theorie der Säculärstörungen vorkommenden Gleichungen numerisch aufzulösen," *Crelle's Journal*, Vol. 30, 1846, pp. 51–94.

[51] K. Bathe, *Finite Element Procedures in Engineering Analysis.* Englewood Cliffs, New Jersey: Prentice-Hall, Inc., 1982.

[52] V. I. Arnold, *Mathematical Methods of Classical Mechanics.* New York: Springer-Verlag, 2nd ed., 1989.

[53] J. E. Slotine and W. Li, *Applied Nonlinear Control.* Englewood Cliffs, New Jersey: Prentice-Hall, Inc., 1991.

[54] W. J. Rugh, *Linear System Theory.* Englewood Cliffs, New Jersey: Prentice-Hall, Inc., 1993.

[55] H. Oz and L. Meirovitch, "Optimal Modal-Space Control of Flexible Gyroscopic Systems," *Journal of Guidance and Control*, Vol. 3, No. 3, 1980, pp. 218–226.

[56] H. Schaub, S. R.Vadali, and J. L. Junkins, "Feedback Control Law for Variable Speed Control Moment Gyroscopes," *8th AAS/AIAA Space Flight Mechanics Meeting*, (Monterey, California), Feb. 9–11 1998. Paper No. AAS 98-140.

[57] S. Krishnan and S. R. Vadali, "An Inverse-Free Technique for Attitude Control of Spacecraft Using CMGs," *Acta Astronautica*, Vol. 39, No. 6, 1997, pp. 431–438.

[58] N. S. Bedrossian, *Steering Law Design for Redundant Single Gimbal Control Moment Gyro Systems.* M.S. Thesis, Mechanical Engineering, MIT, 1987.

[59] D. T. Greenwood, *Principles of Dynamics.* Englewood Cliffs, New Jersey: Prentice-Hall, Inc, 2nd ed., 1988.

[60] W. E. Wiesel, *Spaceflight Dynamics.* New York: McGraw-Hill, Inc., 1989.

[61] P. C. Hughes, *Spacecraft Attitude Dynamics.* New York: John Wiley & Sons, Inc., 1986.

[62] H. S. Oh, S. R. Vadali, and J. L. Junkins, "On the Use of the Work-Energy Rate Principle for Designing Feedback Control Laws," *AIAA Journal of Guidance, Control and Dynamics*, Vol. 15 No. 1, Jan–Feb 1992, pp. 272–277.

[63] J. L. Junkins, *An Introduction to Optimal Estimation of Dynamical Systems*. Alphen aan den Rijn, Netherlands: Sijthoff & Noordhoff International Publishers, 1978.

[64] Y. Nakamura and H. Hanafusa, "Inverse Kinematic Solutions with Singularity Robustness for Robot Manipulator Control," *Journal of Dynamic Systems, Measurement, and Control*, Vol. 108, 1986, pp. 164–171.

# APPENDIX A

## JACOBI METHOD OF GENERATING EIGENFACTORS

Jacobi presented a very elegant method in 1846 in Ref. 50 which diagonalizes a symmetric matrix $[M]$ and thus generates the corresponding eigenvalues and eigenvectors. This Jacobi method has been used for over a century because of its simplicity and stability. It finds the eigenvalues and eigenvectors of a symmetric matrix $[M]$ by pre- and postmultiplying it by successive orthogonal single-axis rotation matrices $[P_i]$ as is briefly outlined below.[51]

Let $[P_i]$ be the $i$-th rotation matrix and $[\Lambda_k]$ be the matrix obtained after pre- and postmultiplying $[M]$ by the first $k$ rotation matrices.

$$[P_k]^T \dots [P_1]^T [P_0]^T [M][P_0][P_1] \dots [P_k] = [\Lambda_k] \tag{A.1}$$

As $k \to \infty$ the matrix $[\Lambda_k]$ becomes diagonal with its entries being the eigenvalues of $[M]$. The eigenvector matrix $[C]$ as defined in Eq. (3.15) is approximated at the $k$-th step as

$$[C] = [P_k]^T \dots [P_1]^T [P_0]^T \tag{A.2}$$

The orthogonal single-axis rotation matrix $[P_{k+1}]$ is defined such that the $i,j$-th entry of $[\Lambda_k]$ is zeroed. The matrix $[P_{k+1}]$ is the identity matrix except for the $i$-th and $j$-th diagonal elements being $\cos\theta$. The only two non-zero off-diagonal elements are the $i,j$-th element being $-\sin\theta$ and the $j,i$-th element being $\sin\theta$. The rotation angle $\theta$ is defined as

$$\theta = \frac{1}{2} \arctan \frac{2\Lambda_{ij}^k}{\Lambda_{ii}^k - \Lambda_{jj}^k} \tag{A.3}$$

if the diagonal elements $\Lambda_{ii}$ and $\Lambda_{jj}$ are distinct or as

$$\theta = \frac{\pi}{4} \tag{A.4}$$

if the diagonal elements are equal. Once the off-diagonal elements are small in magnitude, the procedure is shown to have quadratic convergence.[51] Thus for near diagonal mass matrix, we expect very rapid convergence.

Let $[\hat{C}]$ be a close approximation of the actual eigenvector matrix $[C]$. During numerical simulations, the eigenvectors of the mass matrix at the previous time step would still be available. Since the time steps are typically small, the eigenvectors would not have changed much between integration steps. Let $[\hat{\Lambda}_0]$ be found through

$$[\hat{C}][M][\hat{C}]^T = [\hat{\Lambda}_0] \tag{A.5}$$

Since $[\hat{C}] \neq [C]$, the matrix $[\hat{\Lambda}_0]$ will have some small non-zero off diagonal terms. Instead of resolving a general eigenvalue, eigenvector problem for the current mass matrix, a Jacobi sweep could be performed. A Jacobi sweep sequentially sweeps through all the off-diagonal terms of $[\Lambda]$ and zeros them. Since $[\hat{C}]$ is already close to $[C]$ and the Jacobi method has quadratic convergence, one sweep is usually all it takes to obtain the current eigenvalues and eigenvectors within machine accuracy. To cancel the first off-diagonal element of $[\hat{\Lambda}_0]$, the rotation matrix $P_1$ is constructed and used to obtain $[\hat{\Lambda}_1]$.

$$[P_1]^T[\hat{\Lambda}_0][P_1] = [\hat{\Lambda}_1] \tag{A.6}$$

This process is then repeated to cancel the second off diagonal element of $[\Lambda_1]$ and so on. Assuming the matrix has $k$ significant off-diagonal elements, the current eigen-

vector matrix $[\hat{C}]$ is found through

$$[\hat{C}] = [P_k]^T \ldots [P_1]^T \hat{C} \tag{A.7}$$

The final $[\hat{\Lambda}_k]$ matrix contains the current eigenvalues on the diagonal. Note that each $[P_i][\hat{C}]$ update does not involve a full matrix multiplication. Actually only two eigenvectors are linearly combined (i.e. rotated) to form the new eigenvectors. Thus given an initial estimate of the eigenvectors, with one Jacobi sweep the actual eigenvectors and eigenvalues of the symmetric $[M]$ matrix are found.

# APPENDIX B

## DERIVING VSCMG EQUATIONS OF MOTION USING LAGRANGIAN METHOD

The equations of motion of a rigid spacecraft containing one VSCMG given in Eq. (4.32) was developed using classical Newtonian and Eulerian Methods. To verify this equations, the same equations of motion along with expressions for the RW and gimbal motor torques $u_s$ and $u_g$ are rederived in this appendix using a Lagrangian method. The kinetic energy of a rigid body with one VSCMG is given by

$$T = \frac{1}{2}\boldsymbol{\omega}^T[I_s]\boldsymbol{\omega} + \frac{1}{2}I_{W_s}\left(\hat{\boldsymbol{g}}_s^T\boldsymbol{\omega} + \Omega\right)^2 + \frac{1}{2}I_{G_s}\left(\hat{\boldsymbol{g}}_2^T\boldsymbol{\omega}\right)^2 + \frac{1}{2}J_t\left(\hat{\boldsymbol{g}}_t^T\boldsymbol{\omega}\right)^2 + \frac{1}{2}J_g\left(\hat{\boldsymbol{g}}_g^T\boldsymbol{\omega} + \dot{\gamma}\right)^2 \quad \text{(B.1)}$$

Since there is not potential energy in this dynamical system, the Lagrangian $\mathcal{L}$ is simply the kinetic energy.

$$\mathcal{L} = \mathcal{T} \quad \text{(B.2)}$$

Let $\boldsymbol{p}$ be a fictitious attitude vector such that $\dot{\boldsymbol{p}} = \boldsymbol{\omega}$ and let the angle $\kappa$ be the orientation angle of the RW about its spin axis such that $\dot{\kappa} = \Omega$. The system state vector $\boldsymbol{x}$ is then defined as

$$\boldsymbol{x} = \begin{pmatrix} \boldsymbol{p} \\ \gamma \\ \kappa \end{pmatrix} \quad \text{(B.3)}$$

The spacecraft equations of motion are found by evaluating the expression

$$\frac{{}^{\mathcal{N}}d}{dt}\left(\frac{\partial\mathcal{L}}{\partial\dot{\boldsymbol{p}}}\right) - \frac{\partial\mathcal{L}}{\partial\boldsymbol{p}} = \boldsymbol{L} \quad \text{(B.4)}$$

where $\boldsymbol{L}$ is the external torque vector. Since $\partial\mathcal{L}/\partial\boldsymbol{p} = 0$ only the first expression of Eq. (B.4) needs to be calculated. Noting that $\dot{\boldsymbol{p}} = \boldsymbol{\omega}$, the partial derivative of $\mathcal{L}$ with respect to $\boldsymbol{\omega}$ is

$$\frac{\partial\mathcal{L}}{\partial\boldsymbol{\omega}} = [I_s]\boldsymbol{\omega} + I_{W_s}\left(\hat{\boldsymbol{g}}_s^T + \Omega\right)\hat{\boldsymbol{g}}_s + I_{G_s}\left(\hat{\boldsymbol{g}}_s^T\boldsymbol{\omega}\right)\hat{\boldsymbol{g}}_s + J_t\left(\hat{\boldsymbol{g}}_t^T\boldsymbol{\omega}\right)\hat{\boldsymbol{g}}_t + J_g\left(\hat{\boldsymbol{g}}_g^T\boldsymbol{\omega} + \dot{\gamma}\right)\hat{\boldsymbol{g}}_g \quad \text{(B.5)}$$

The inertial derivative of Eq. (B.5) is

$$\begin{aligned}\frac{\mathcal{N}d}{dt}\left(\frac{\partial\mathcal{L}}{\partial\boldsymbol{\omega}}\right) = {} & [I_s]\dot{\boldsymbol{\omega}} + [\tilde{\boldsymbol{\omega}}][I_s]\boldsymbol{\omega} + I_{W_s}\left(\dot{\hat{\boldsymbol{g}}}_s^T\boldsymbol{\omega} + \hat{\boldsymbol{g}}_s^T\dot{\boldsymbol{\omega}} + \dot{\Omega}\right)\hat{\boldsymbol{g}}_s + I_{W_s}\left(\hat{\boldsymbol{g}}_s^T\boldsymbol{\omega} + \Omega\right)\dot{\hat{\boldsymbol{g}}}_s \\ & + I_{G_s}\left(\dot{\hat{\boldsymbol{g}}}_s^T + \hat{\boldsymbol{g}}_s^T\dot{\boldsymbol{\omega}}\right)\hat{\boldsymbol{g}}_s + I_{G_s}\left(\hat{\boldsymbol{g}}_s^T\boldsymbol{\omega}\right)\dot{\hat{\boldsymbol{g}}}_s + J_t\left(\dot{\hat{\boldsymbol{g}}}_t^T\boldsymbol{\omega} + \hat{\boldsymbol{g}}_t^T\dot{\boldsymbol{\omega}}\right)\hat{\boldsymbol{g}}_t + J_t\left(\hat{\boldsymbol{g}}_t^T\boldsymbol{\omega}\right)\dot{\hat{\boldsymbol{g}}}_t \\ & + J_g\left(\dot{\hat{\boldsymbol{g}}}_g^T\boldsymbol{\omega} + \hat{\boldsymbol{g}}_g^T\dot{\boldsymbol{\omega}} + \ddot{\gamma}\right)\hat{\boldsymbol{g}}_g + J_g\left(\hat{\boldsymbol{g}}_g^T\boldsymbol{\omega} + \dot{\gamma}\right)\dot{\hat{\boldsymbol{g}}}_g \quad \text{(B.6)}\end{aligned}$$

After substituting Eqs. (4.20) and (B.6) into Eq. (B.4) and performing some algebraic manipulations, the equations of motion of a rigid spacecraft with one VSCMG given in Eq. (4.32) are found.

$$\begin{aligned}[I]\dot{\boldsymbol{\omega}} = {} & -[\tilde{\boldsymbol{\omega}}][I]\boldsymbol{\omega} - \hat{\boldsymbol{g}}_s\left(J_s\dot{\gamma}\omega_t + I_{W_s}\dot{\Omega} - (J_t - J_g)\,\omega_t\dot{\gamma}\right) \\ & - \hat{\boldsymbol{g}}_t\left(\left(J_s\omega_s + I_{W_s}\Omega\right)\dot{\gamma} - (J_t + J_g)\,\omega_s\dot{\gamma} + I_{W_s}\Omega\omega_g\right) \\ & - \hat{\boldsymbol{g}}_g\left(J_g\ddot{\gamma} - I_{W_s}\Omega\omega_t\right) + \boldsymbol{L}\end{aligned} \quad \text{(B.7)}$$

To find the RW motor torque $u_s$, the following Lagrange equation of motion is solved.

$$\frac{\mathcal{N}d}{dt}\left(\frac{\partial\mathcal{L}}{\partial\dot{\kappa}}\right) - \frac{\partial\mathcal{L}}{\partial\boldsymbol{\kappa}} = u_s \quad \text{(B.8)}$$

where $\dot{\kappa} = \Omega$. Note that $\partial\mathcal{L}/\partial\kappa = 0$ for this system. The partial derivative of $\mathcal{L}$ with

respect to $\mathcal{L}$ is

$$\frac{\partial \mathcal{L}}{\partial \Omega} = I_{W_s}\left(\hat{\boldsymbol{g}}_s^T \boldsymbol{\omega} + \Omega\right) \tag{B.9}$$

whose time derivative is given by

$$\frac{d}{dt}\left(\frac{\partial \mathcal{L}}{\partial \Omega}\right) = I_{W_s}\left(\dot{\hat{\boldsymbol{g}}}_s^T \boldsymbol{\omega} + \hat{\boldsymbol{g}}_s^T \dot{\boldsymbol{\omega}} + \dot{\Omega}\right) \tag{B.10}$$

After substituting Eqs. (4.20) and (B.10) into Eq. (B.8), the RW motor torque given in Eq. (4.26) is found.

$$u_s = I_{W_s}\left(\dot{\Omega} + \hat{\boldsymbol{g}}_s^T \dot{\boldsymbol{\omega}} + \dot{\gamma}\omega_t\right) \tag{B.11}$$

The gimbal motor torque $u_g$ is found by solving the Lagrange equation of motion

$$\frac{{}^{\mathcal{N}}d}{dt}\left(\frac{\partial \mathcal{L}}{\partial \dot{\gamma}}\right) - \frac{\partial \mathcal{L}}{\partial \boldsymbol{\gamma}} = u_g \tag{B.12}$$

The partial derivative of $\mathcal{L}$ with respect to $\gamma$ is non-zero in this case and is given by

$$\frac{\partial \mathcal{L}}{\partial \gamma} = I_{W_s}\left(\hat{\boldsymbol{g}}_s^T \boldsymbol{\omega} + \Omega\right)\frac{\partial \hat{\boldsymbol{g}}_s}{\partial \gamma}^T \boldsymbol{\omega} + I_{G_s}\left(\hat{\boldsymbol{g}}_s^T \boldsymbol{\omega}\right)\frac{\partial \hat{\boldsymbol{g}}_s}{\partial \gamma}^T \boldsymbol{\omega} + J_t\left(\hat{\boldsymbol{g}}_t^T \boldsymbol{\omega}\right)\frac{\partial \hat{\boldsymbol{g}}_t}{\partial \gamma}^T + J_g\left(\hat{\boldsymbol{g}}_g^T \boldsymbol{\omega} + \dot{\gamma}\right)\frac{\partial \hat{\boldsymbol{g}}_g}{\partial \gamma}^T \tag{B.13}$$

After making use of

$$\frac{\partial \hat{\boldsymbol{g}}_s}{\partial \gamma} = \hat{\boldsymbol{g}}_t \tag{B.14a}$$

$$\frac{\partial \hat{\boldsymbol{g}}_t}{\partial \gamma} = -\hat{\boldsymbol{g}}_s \tag{B.14b}$$

$$\frac{\partial \hat{\boldsymbol{g}}_g}{\partial \gamma} = 0 \tag{B.14c}$$

and the inertia definition in Eq. (4.28), this is simplified to

$$\frac{\partial \mathcal{L}}{\partial \gamma} = \left(J_s - J_t\right)\omega_t\omega_s + I_{W_s}\Omega\omega_t \tag{B.15}$$

The partial derivative of $\mathcal{L}$ with respect to $\dot{\gamma}$ is

$$\frac{\partial \mathcal{L}}{\partial \dot{\gamma}} = J_g \left( \hat{\boldsymbol{g}}_g^T \boldsymbol{\omega} + \dot{\gamma} \right) \tag{B.16}$$

After making use of Eq. (4.20), the time derivative of Eq. (B.16) is found to be

$$\frac{d}{dt} \left( \frac{\partial \mathcal{L}}{\partial \dot{\gamma}} \right) = J_g \left( \hat{\boldsymbol{g}}_g^T \dot{\boldsymbol{\omega}} + \ddot{\gamma} \right) \tag{B.17}$$

Combining Eqs. (B.15) and (B.17) in Eq. (B.12) the gimbal motor torque in Eq. (4.29) is found.

$$u_g = J_g \left( \hat{\boldsymbol{g}}_g^T \dot{\boldsymbol{\omega}} + \ddot{\gamma} \right) - \left( J_s - J_t \right) \omega_s \omega_t - I_{W_s} \Omega \omega_t \tag{B.18}$$

# VITA

Hanspeter Schaub is the son of Hanspeter and Margarita Schaub of Füllinsdorf, Switzerland. Hanspeter received the Matura Typus-C from the Gymnasium Liestal in Switzerland in 1987. After fulfilling his military duties with the Swiss army he went to Texas A&M University in 1988. He earned a B.S. degree in aerospace engineering in May 1992, a M.S. degree in aerospace engineering in August 1994 and a Ph.D. in aerospace engineering in May 1998. All graduate level work was performed under the supervision of Dr. John L. Junkins. The master's studies focused on developing a prototype three-dimensional laser scanning system. The Ph.D. studies centered around several spacecraft controls related topics. A sample of published journal papers includes:

Schaub, H. and Junkins, J. L., "Stereographic Orientation Parameters for Attitude Dynamics: A Generalization of the Rodrigues Parameters," *Journal of the Astronautical Sciences*, Vol. 44, No. 1, Jan.–Mar. 1996, pp. 1–19.

Schaub, H., Robinett, R. D., and Junkins, J. L., "Globally Stable Feedback Laws for Near-Minimum-Fuel and Near-Minimum-Time Pointing Maneuvers for a Landmark-Tracking Spacecraft," *Journal of the Astronautical Sciences*, Vol. 44, No. 4, Oct.–Dec. 1996, pp. 443–466.

Schaub, H., Robinett, R. D., and Junkins, J. L., "Adaptive External Torque Estimation by Means of Tracking a Lyapunov Function," *Journal of the Astronautical Sciences*, Vol. 44, No. 3, July–Sept. 1996.

Schaub, H., Robinett, R. D., and Junkins, J. L., "New Penalty Functions For Optimal Control Formulation for Spacecraft Attitude Control Problems," *Journal of Guidance, Control and Dynamics*, Vol. 20, No. 3, May–June 1997, pp. 428–434.

His permanent mailing address is Giebenacherstr. 73, 4414 Füllinsdorf, Switzerland.